POLITECNICO
MILANO 1863

SCUOLA DI INGEGNERIA INDUSTRIALE
E DELL'INFORMAZIONE

Graphene oxide reduction and decoration with lead sulphide nanoparticles for gas sensing application

TESI DI LAUREA MAGISTRALE IN
MATERIALS ENGINEERING AND NANOTECHNOLOGY
INGEGNERIA DEI MATERIALI E DELLE NANOTECNOLOGIE

Author: Valentina Berlin

Student ID: 963952
Advisor: Andrea Li Bassi
Co-advisors: Benoit Hackens, Sophie Hermans, Fernando Massa Fernandes
Academic Year: 2021-2022

Abstract

The growing concern about the worsening of air quality in highly polluted environments has led to the development of new low-cost, high-performance devices, capable of detecting even small amount of the analyte in complex gas mixtures. Hybrid functional nanomaterials-based chemiresistive sensors have been proposed as suitable candidates for environmental monitoring, thanks to their high sensitivity, fast response, and energy efficiency. Among these, reduced graphene oxide (rGO) decorated with semiconductor nanoparticles has emerged as inexpensive alternative to the more common functionalised pristine graphene. In this thesis, different graphene oxide's reduction mechanisms have been investigated with the aim of improving their effectiveness, and rGO flakes decoration with lead sulphide nanoparticles has been explored for application in chemiresistive methane sensors.

The first part of the work has been dedicated to the morphological study of commercially available graphene oxide (GO) sources, in order to establish the exfoliation parameters to obtain homogeneous dispersions of small single flakes. Different reduction methods were then explored, namely thermal annealing assisted by ethanol or benzene healing, simple chemical reduction with ascorbic acid, and solvothermal annealing in NMP. The results of the analysis conducted on the reduced GO samples revealed that the combined action of the latter two processes is extremely effective in the removal of the oxygen functionalities from graphene oxide basal plane, allowing a decrease in resistance up to 10 orders of magnitude. The second part of the thesis is instead dedicated to the discussion of the outcomes of the analysis performed on lead sulphide nanoparticles (NPs), synthetized at room temperature in aqueous solution. Lastly, the results of the decoration of the rGO flakes with lead sulphide nanocrystals are presented, as well as the preliminary results about the gas sensing performance of the rGO-PbS NPs devices.

Key-words: graphene oxide (GO), reduced graphene oxide (rGO), thermal annealing, ascorbic acid, lead sulphide nanoparticles, chemiresistive methanol sensors.

Abstract in italiano

La crescente preoccupazione per il peggioramento della qualità dell'aria in ambienti altamente inquinati ha portato allo sviluppo di nuovi dispositivi a basso costo e alte prestazioni, in grado di rilevare anche basse concentrazioni di analita in miscele di gas. Sensori basati su nanomateriali funzionali ibridi sono considerati promettenti candidati per il monitoraggio ambientale, grazie alla loro elevata sensibilità, rapida risposta ed efficienza energetica. Tra questi, l'ossido di grafene ridotto (rGO) decorato con nanoparticelle di semiconduttori si distingue come alternativa economica al più comune grafene. In questo lavoro di tesi, sono stati studiati diversi meccanismi di riduzione dell'ossido di grafene con l'obiettivo di migliorarne l'efficacia, ed è stata valutata la possibilità di decorare scaglie di rGO con nanoparticelle di solfuro di piombo per l'applicazione in sensori di metano.

La prima parte del lavoro è stata dedicata all'analisi della morfologia di ossidi di grafene (GO) disponibili in commercio, al fine di stabilire i parametri di esfoliazione per ottenere una dispersione omogenea di singoli fogli di GO. Sono stati quindi esplorati diversi metodi di riduzione, ovvero riduzione per via termica assistita da etanolo o benzene, semplice riduzione chimica con acido ascorbico e riduzione solvotermica in 1-metil-2-pirrolidone. I risultati dell'analisi condotta sui campioni di GO ridotto hanno rivelato che la combinazione delle ultime due tecniche menzionate è estremamente efficace nella rimozione dei gruppi funzionali contenenti ossigeno, consentendo una diminuzione della resistenza fino a 10 ordini di grandezza. La seconda parte della tesi è invece dedicata alla discussione degli esiti delle indagini condotte su nanoparticelle di solfuro di piombo, sintetizzate a temperatura ambiente in soluzione acquosa. Infine, sono riportate le immagini dei fogli di rGO decorati con nanocristalli di solfuro di piombo, e i risultati preliminari dei test sulla rilevazione di gas metano da parte di tali dispositivi.

Parole chiave: ossido di grafene (GO), ossido di grafene ridotto (rGO), riduzione termica, acido ascorbico, nanoparticelle di solfuro di piombo, sensori chemoresistivi di metano.

Contents

1 Introduction

Globally, there is a long-standing demand for highly sensitive, inexpensive, and energy-efficient miniaturized gas sensors for the detection of harmful and environmentally polluting gases such as NO_2, NH_3, CO_2, CO and CH_4. To date, the solutions available on the market present limitation related to high capital costs, poor portability and high operating temperatures. In this context, the use in chemiresistive sensors of hybrid functional nanomaterials and especially graphene-based ones has attracted considerable attention.

As a sensing element, graphene shows a remarkable response to ultralow concentration of absorbed molecules because of the interaction of the analyte with the delocalized cloud of π-electrons. Moreover, graphene can also be employed in conjunction with other nanometric structures for the detection of those gases that are not strong charge donors or acceptor. Graphene-based hybrid gas sensors based on charge transfer effect belong to the latter category. Among these, reduced graphene oxide (rGO) planes decorated with semiconductor nanoparticles present outstanding performances in terms of responsivity and sensitivity due to the simultaneous effect of superb interaction of the nanocrystals (NCs) with the analyte and great charge transport in rGO.

The interest of the scientific community towards reduced graphene oxide is justified not only by its remarkable electronic characteristics that make it suitable for gas sensing application, but also because, differently from its pristine counterpart, it allows high-volume production at a relatively low-cost. Different reduction processes have been proposed to remove the oxygen functionalities that hinder the conduction of charge carriers along graphene oxide's basal plane; however, the fact that many of these techniques are not efficient in reducing highly oxygenated graphene oxide samples, opens the way for further research on this topic.

2 State of art

2.1. Graphene oxide

Since its discovery, graphene, a two-dimensional plane of sp^2 hybridized carbon atoms, has attracted a great deal of interest in the scientific community because of its remarkable properties that originate from the delocalization of the π band over the honeycomb structure. Graphene, indeed, shows high mechanical strength (1.24 TPa) [1] and thermal conductivity (4000 Wm^{-1} K^{-1}) [2], good optical transmittance (97.7%) [3], large specific surface area (2600 m^2 g^{-1}) and unusually high charge carrier mobility (105 cm^2 V^{-1} s^{-1}) [4]. Although these characteristics makes graphene a good candidate for applications in multiple fields [5], limitation related to the difficult scalability and high costs of its manufacturing processes still persists. Some examples of bottom-up synthesis methods comprehend chemical vapor deposition (CVD) on metal foils [6] and epitaxial growth on silicon carbide [7], while among top-down methods micromechanical cleavage [8] and exfoliation of graphite intercalated compounds (GICs) can be mentioned. In the last years, there has been a growing interest towards the employment of graphene oxide (GO) in top-down solution synthesis processes for the production of chemically derived graphene. More specifically, GO is obtained from graphite through chemical or electrochemical exfoliation, based on processes proposed by Brodie, Staudenmaier, Hofmann and Hummer [9, 10]. Currently, a modified form of the Hummer's method [11] is the most common route for oxidizing graphite, due to its high yield, low toxicity levels and low explosion risk.

Reduced graphene oxide, obtained from the chemical or thermal removal of the oxygen-containing functional groups present on the surface of its precursor, exhibits similar properties to those of graphene, but it allows for high-yield production and tunable electrical properties through control of the sp^2-to-sp^3 ratio [12]. A schematic representation of the steps required for the production of rGO is reported in Figure 2.1.

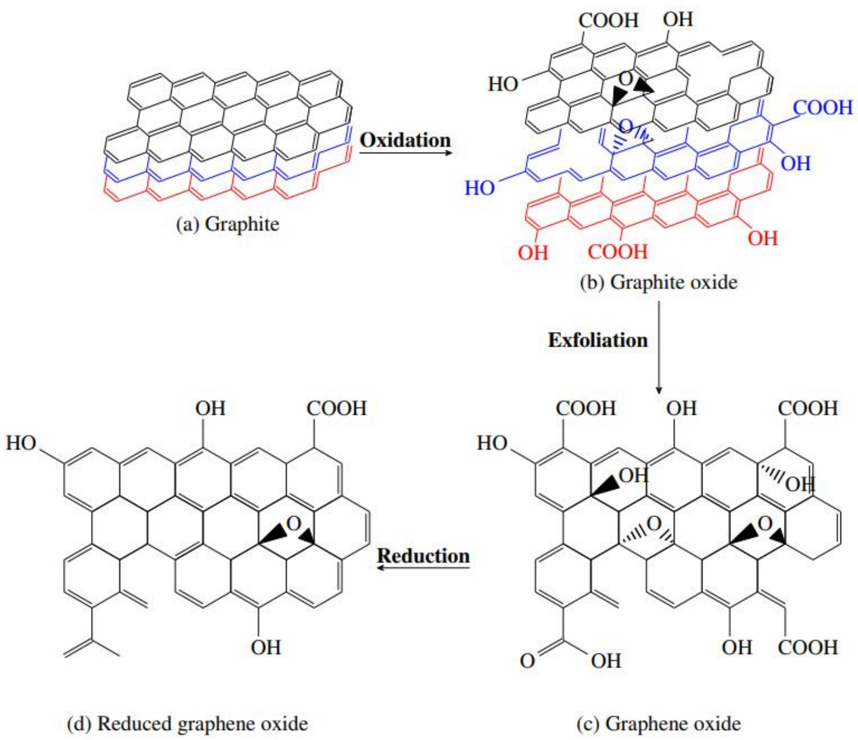

Figure 2.1: Schematic representation of the steps required for the production of rGO.

2.1.1. Graphene oxide and reduced graphene oxide's structure

In order to uncover all the possible applications of graphene oxide and its reduced form, it is important to first have an understanding about GO's structure. Contrarily from pristine graphene that contains only sp^2-hybridized carbon atoms organized in a honeycomb structure, it is known that graphene oxide includes oxygenated functional groups that disrupt the crystalline network of sp^2 carbon atoms. However, scientists have not yet reached an agreement about the exact structure of graphene oxide, mostly because of its amorphous character and the high structural variability between samples prepared with different protocols and conditions. Nevertheless, many authors proposed several models to describe the structure of graphene oxide.

Early research, such as the one conducted by Hofmann and Holst [13], proposed GO structural models with stoichiometric regular lattices. In particular, the two authors suggested a planar structure decorated with 1,2-epoxides, with a final molecular formula of C_2O (Figure 2.2, (a)). Hofmann and Holst's structure was later revised by Ruess [14], who, to account for the presence of hydrogen, proposed a model with hydroxyl groups linked to a sp^3-hybridized basal plane (Figure 2.2, (b)). Scholz and Boehm [15] presented a third model, characterized by the absence of epoxy and ether groups, substituted only by hydroxyl and ketone groups (Figure 2.2, (c)). The final stochiometric model was suggested by Nakajima and Matsuo, who assumed a structure similar to the one of poly(dicarbon monofluoride), $(C_2F)_n$ (Figure 2.2, (d)).

Thanks to the introduction of nuclear magnetic resonance (NMR) spectroscopy to the study of graphene oxide, it was finally possible to abandon the lattice-based structure in favor of a non-stoichiometric one. The firsts to do so were Lerf and Klinowski, whose model is viewed as one of the most credible [16]. They hypothesized the GO structure to be a planar sheet of aromatic regions surrounded by sp^3-hybridized carbon decorated with hydroxyl and epoxy (1,2-ether) functional groups. They also suggested that carboxyl and carbonyl groups are located only at the sheet edges (Figure 2.2, (e)).

Finally, Dékány and Szabò formulate a model that turn away from Lerf and Klinowski's planar structure, to embrace Ruess and Scholz–Boehm's ideas of a corrugated structure. Indeed, in light of the results obtained through several characterization techniques (nuclear magnetic resonance spectroscopy (NMR), transmission electron microscopy (TEM), elemental analysis (EM), Fourier transform infrared spectroscopy (FT-IR), X-Ray photoelectron spectroscopy (XPS) and X-Ray diffraction spectroscopy (XRD)), Dékány and Szabò theorized a structure with trans-linked cyclohexane chairs and linear hexagonal ribbons (Figure 2.2, (f)) [17, 18].

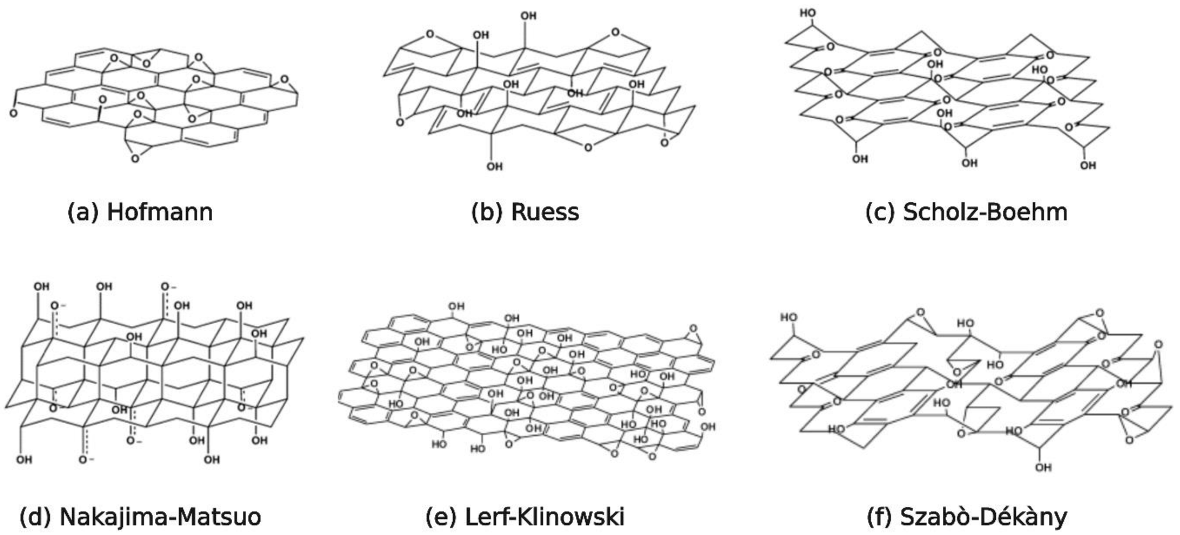

Figure 2.2: Schematic representation of graphene oxide's structure proposed by different authors. Adapted from [19].

The determination of chemical structure of reduced graphene oxide presents all the problems listed for its precursor, plus one more, related to the fact that different reduction technique allows to accomplish various reduction degrees, interpreted as the amount of residual oxygen functional groups on the surface of rGO sheets. Moreover, reduction conditions (temperature, type and concentration of reducing agent, …) can greatly influence the degree of graphitization of the final structure. A schematic representation of the possible structure of a graphene oxide sheet before and after reduction is reported in Figure 2.3.

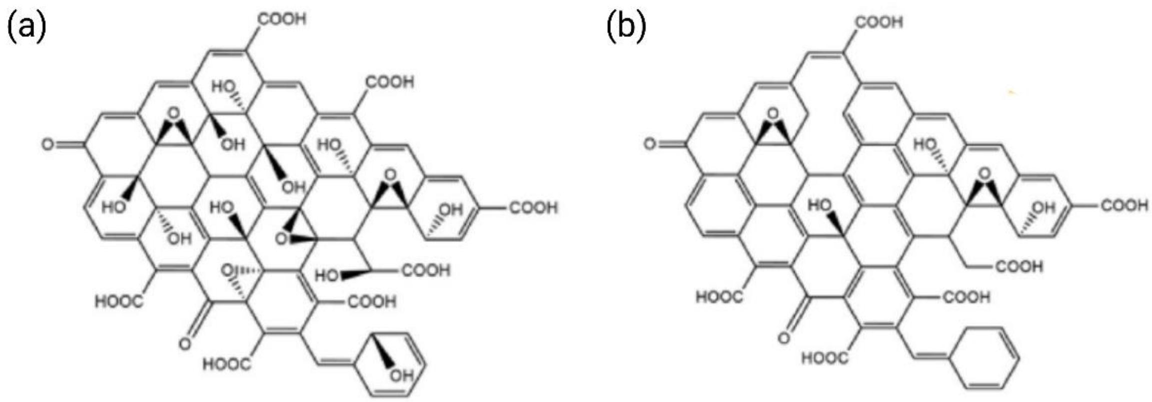

Figure 2.3: Schematic representation of the structure of (a) graphene oxide and (b) reduced graphene oxide. Adapted from [20].

2.1.2. Graphene oxide and reduced graphene oxide's properties

Graphene oxide and its reduced form present several exceptional properties, including controllable electronic conductivity and mechanical strength, broadband fluorescence and optical transparency, tunable thermal conductivity, and high chemical reactivity, which open the way for chemical modification of as-prepared GO. Based on these remarkable characteristics which depend on the degree of oxidation of the 2D structure, GO proved to be a good candidate for many applications in the field of sensors, energy storage and energy production, catalysis and flexible electronics [21].

In the development of gas sensing devices, a variation in the value of each of these properties when the molecules of interest are present can be exploited for the detection mechanism. In particular, it has been proven that, when used as a conductive path for charge carriers, rGO is able to provide an enhancement in the sensing ability of the gas-interacting elements (usually semiconductor nanoparticles) and an overall faster and more accurate response of the sensor to the detected entity, in the form of a resistance variation [22, 23, 24, 25]. For this reason, the understanding of the conduction mechanism in rGO flakes, briefly reviewed in this section, is of critical importance.

2.1.2.1. Electronic properties

It is well known that pristine graphene sheets show a semiconductive behavior with a zero-band gap and a nearly ballistic transport at room temperature [26]. However, when oxygen functional groups are introduced, the destruction of the delocalized π-band, caused by the bonding of oxygen moieties to the graphene plane, results in the opening of the band gap up to few eV. The degree of oxygenation and the type and distribution of oxygen-containing groups strongly influence the electronic band structure. In particular, Joung *et al*. report a band gap variation from 0.21 to 1.43 eV with a decrease in the sp^2 fraction from 80 to 55% [12]. Gue *et al*. obtained a similar trend: with a rise in oxygen coverage from 0.17 to 0.62, the badgap increased from 0.9 eV to 2.4 eV [27]. The effect of the epoxy to hydroxyl ratio has been investigated by Liu *et al*., revealing that at a fixed coverage rate, an increase in the hydroxyl groups content cause an enlargement of the energy gap [28]. Finally, Katsnelson and colleagues, concluded that randomly distributed oxygen containing groups cause a greater reduction in conductivity compared to clustered ones, since the latter produce less electron scattering [29].

Upon chemical and thermal treatments, the structural changes occurring on the basal plane are accompanied by a transition from an insulating to semiconductive behaviour. However, despite GO's deoxygenation, the impossibility to recover a perfect sp^2-hybridized plane means that rGO's charge transport mechanism differs from that of graphene. The disordered structure of a single rGO sheet, consisting in sp^2 domain surrounded by sp^3 carbons, is characterized by hopping transport phenomenon at low temperatures, involving electron inelastic tunneling processes between two localized states around the Fermi level (E_F) [30]. Several studies [30, 31, 32, 12, 33, 34] report a good agreement between low temperature resistance data and two different hopping conduction mechanism, i.e., Mott variable range hopping (M-VRH) and Efros-Shklovskii variable range hopping (ES-VRH). The most significant difference between M-VRH and ES-VRH is that the former considers a constant density of states (DOS) around E_F, while the latter state that, because of the Coulomb interaction between electron-hole pairs, the DOS vanisher linearly in the vicinity of E_F. The general form of the variable range hopping is reported in Equation (2.1):

$$R(T) = R_0 \exp\left(\frac{T_0}{T}\right)^p \tag{2.1}$$

Where R_0 is a pre-exponential factor, T_0 is the characteristic temperature and p is the characteristic exponents of the specific conduction model. More precisely, p = 1 for thermally activated processes, p = ½ for ES-VRH model and p = $1/(n+1)$ for M-VRH model; n represents the spatial dimensionality of the system, so p = ½ or ¼ for 2D-VRH and 3D-VRH, respectively. Assuming a negligible temperature dependance of the pre-exponential factor, the hopping parameter T_0 for the two model is expressed through the following equations (Equation (2.2)):

$$T_0 = T_M = \left(\frac{3}{k_B N(E_F)\xi^2}\right) \qquad T_0 = T_{ES} = \left(\frac{2.8e^2}{4\pi\varepsilon\varepsilon_0 k_B \xi^2}\right) \tag{2.2}$$

Where ξ is the localization length, ε_0 is the value of the permittivity in vacuum, ε is rGO's dielectric constant, k_B the Boltzmann constant and $N(E_F)$ is the DOS near E_F [12]. Numerous authors have reported about the conduction mechanism in rGO. Joung *et al*. and Haque *et al.* obtained a good data fitting with p~0.5 in a temperature range of 295-40 K, reflecting ES-VRH conduction mechanism for hydrazine-reduced rGO and pulsed-laser deposited rGO [12, 35]. On the contrary, three other research groups reported about the charge transport in chemically derived graphene, finding that rGO samples displayed a 2D-VRH conduction mechanism [30, 33, 34]. Cheah and colleagues claim that the degree of disorder of reduced graphene oxide is the cause of this variance in results: partially disordered samples, characterized by high sp^2/sp^3 ratios, generally follow Mott-VHR behavior, while the charge transport in highly disordered structures is better described by Efros-Shklovskii VHR [36]. This aspect highlights the importance of the reduction mechanism in controlling the electrical properties of rGO-based devices.

The fitting of the high temperature conduction regime with an Arrhenius model is widely accepted. The transition from a VRH to band-like transport mechanism is supposedly promoted by the restoration of the sp^2 domain, making rGO with low oxidation degrees more likely to experience an Arrhenius-type conduction at lower temperatures [34, 30, 35].

Finally, recent studies opened the way for the interpretation of the charge transport mechanisms in multilayer reduced graphene oxide. Kovtun *et al*. suggested that charges can move in three dimensions by traveling through a network of stacked sp² domain belonging to different rGO planes, effectively avoiding the defective regions [26]. Figure 2.4 shows a schematic representation of overlapping sp² areas and the inter-sheet conductive path. This mechanism of conduction is further supported by the findings of Cınar and colleagues, who discovered that multilayer charge transport leads to higher conductivity values compared to those recorded on a single sheet for highly defective rGO, while film stacking constitutes a source of scattering for low defective samples [37].

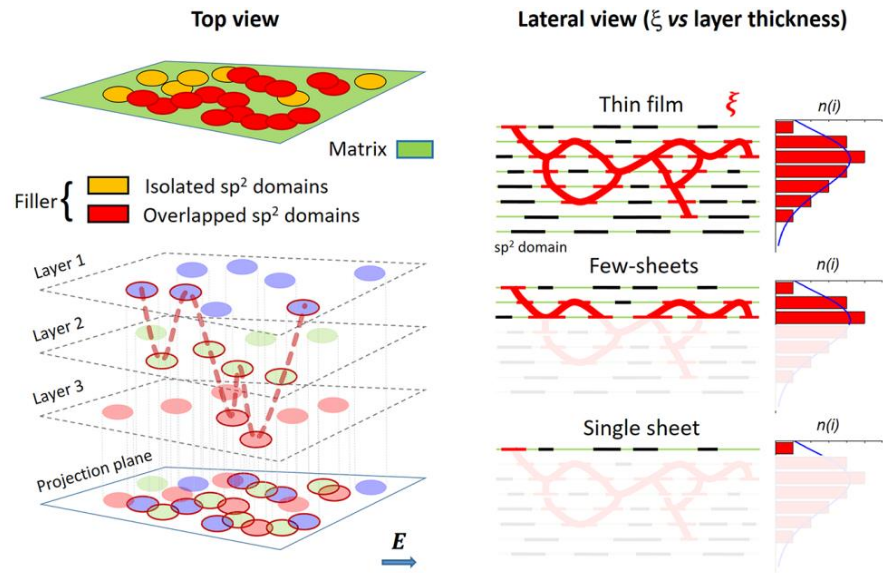

Figure 2.4: Schematic representation of overlapping sp² domains and the inter-sheet conductive path [26].

2.1.3. Graphene oxide's reduction strategies

To restore the sp²-hybridized honeycomb structure that characterize graphene sheets, graphene oxide must undergo treatments for the removal of oxygen functionalities. Different reduction techniques have been proposed, such as photocatalytic reduction, microwave irradiation, hydrothermal reduction, thermal reduction, solvothermal reduction and chemical reduction. In particular, the last three reduction methods have drawn the attention of the scientific community because of their effectiveness and ease of implementation.

It is important to mention that the product of the reduction efforts does not fully resemble pristine graphene: defect in the form of vacancies and residual oxygen moieties greatly affect the thermal, electrical and mechanical properties of the final result. For this reason, healing treatments, often involving a carbon source, are put in place to restore the basal plane and consequently improve the properties dependent on the delocalization of the π band over the honeycomb structure.

2.1.3.1. Thermal annealing

Thermal annealing is a reduction method that involves solely the heating of graphene oxide in a controlled atmosphere (high vacuum conditions, or inert and reducing gases) to promote the removal of oxygen-containing groups. Two different approaches to thermal annealing can be employed: the first one involves a rapid heating of the GO sample up to very high temperatures (~2000°C), while the second, called low temperature thermal annealing, consist in exposing graphene oxide to temperature not higher than 500°C [20]. The former approach exploits the high reactivity of oxygen at elevated temperature to promote the sudden evolution and expansion of CO and CO_2. These gases, trapped between graphene oxide layers, generates huge pressures that promote the exfoliation of rGO sheets. McAllister *et al*. demonstrated that the pressure required to separate two GO sheets, bonded together through Van der Waals forces, is equal to 2.5 MPa, a value 1-2 orders of magnitude lower than the pressure estimated during thermal annealing between 200°C and 1000°C [38]. The main drawback of thermal exfoliation of GO is the removal of carbon atoms from the basal plane, which damages the structure and causes the fragmentation of graphene sheets into small, wrinkled pieces [39]. This effect can be partially mitigated if GO exfoliation is performed before thermal annealing. X-Ray photoelectron spectroscopy (XPS) measurements have been conducted on thermally reduced samples, revealing the dependance of the degree of deoxygenation on the annealing temperature; in particular it has been found that the higher the temperature of the reduction procedure, the more efficiently the O-groups are removed from GO surface. Different authors [38, 40, 41] have reported an increase in electrical conductivity of reduced graphene oxide sheets after thermal treatments at progressively high temperatures. Limitations to this kind of reduction technique are related to the high costs of the process, as maintaining elevated temperature in a furnace for many hours is very expensive, and to the nature of the substrate, since not every material can withstand very high temperature. The latter is a problem frequently encountered in graphene-based sensor production, since interdigitated electrodes cannot be exposed to temperatures higher than 300-400°C (more details reported in Section 3.2.1).

The second approach to thermal annealing is based on the observation that oxygen-containing groups can be removed from the carbon plane starting from temperatures around 200°C [42]. Alam *et al.* have studied through thermogravimetric analysis (TGA) the evolution of mass loss of GO during a thermal annealing experiment [43]. They discovered that a 30% mass loss occurs at a temperature around 200°C, because of the thermal decomposition of unstable oxygen moieties, such as hydroxyl, carbonyl and carboxylic groups. Moreover, Fourier-transform infrared (FTIR) analysis and four-point probe resistance measurements conducted by Ramamoorthy *et al*. showed the flattening of the peak associated to hydroxyl groups starting from 200°C. They also noticed a notable reduction in resistance for sample annealed at 300°C, compared to those treated at lower temperatures. This last observation suggest that GO's transition temperature must lie in between 200 °C and 250 °C [44]. Additionally, XPS spectra obtained by Mattevi *et al.* revel a high rate of oxygen groups loss between 100-250°C and a decrease in C-O components up to 450°C [45]. Finally, molecular dynamics (MD) simulations of the structure of progressively reduced GO confirm the desorption of hydroxyl and epoxy groups at low temperatures but also the high thermal stability of carbonyl and ether groups [39]. In conclusion, low temperature thermal annealing allows for a partial removal of oxygen function groups with lower damages to the carbon basal plane and without altering the nature of the substrate on which GO is deposited. However, this technique can require long annealing times to obtain acceptable results.

2.1.3.2. Solvothermal annealing

Solvothermal reduction is presented in literature as an environmentally friendly and easily scalable reduction technique that promotes graphene oxide deoxygenation by exploiting the high temperature reducing character of the solvent in which GO is dispersed [46].

In hydrothermal processes, usually carried out in a sealed container, overheated supercritical (SC) water not only stimulate the removal of oxygen moieties, but it also promotes the recovery of π-conjugation in the basal plane. Zhou *et al.* suggested a reduction mechanism that involves the acid-catalyzed dehydration of hydroxyl groups, possible thanks to the acid environment that characterized superheated H_2O. The limit of this approach is the aggregation of rGO sheets, which is an irreversible condition [47]. Stable rGO dispersions can be obtained by solvothermal annealing in organic solvents, such as N,N-dimethylformamide (DMF) and N-methyl-2-pyrrolidone (NMP) [48]. In particular, the very high boiling point of NMP (~200°C) allows to perform the reduction at atmospheric pressure, as described by Dubin *et al*. The mechanism of deoxygenation of GO was inferred to be accomplished through a simultaneous action of thermal annealing and interaction with NMP molecules, while the colloidal stability was supposedly related to the hydrogen bond between the latter and rGO. With this technique the authors were able to yield rGO sheets with a final conductivity of $1.38 \cdot 10^3$ S/m, a value not as high as that achievable through other reduction methods (i.e., hydrazine reduction or high temperature thermal annealing), but that can still be suitable for several applications [49, 50].

2.1.3.3. Healing strategies with carbon source

As previously mentioned, one of the strategies that can employed to repair the damages caused the removal of oxygen containing groups is exposing rGO sheets to a carbon source during thermal annealing. Several carbon sources have been investigated so far, such as acetylene [51], ethylene [52], methane [53, 54, 55, 56], benzene [57, 58] and ethanol [56, 53, 20, 59]. In this work, benzene and ethanol were tested as possible species for sp^2 bond repair.

There are not many studies focused on the evaluation of benzene as viable carbon source for rGO healing, in all likelihood because of its high toxicity and environmental risk. However, aromatic molecules may be a suitable resource for rGO repair, due to their known interaction (π–π bond) with the delocalized π-bond cloud of graphene-like structures. Hassan *et al.* explored the dispersion force mediated interactions between defective graphene and benzene, finding two different trends depending on the nature of the defect itself. In correspondence of in-plane defects, like vacancies or substitutional oxygen atoms, benzene shows a binding energy comparable to that recorded on pristine graphene [57]. On the contrary, defects that present a spatial extension outside the plane (hydroxyl, epoxy, and carboxyl groups) exhibit a reduced interaction with benzene molecules. This result is predictable as the geometric constraints imposed by larger defect hinders the nearing of benzene molecules to the planar graphene-like structure. Park *et al.*, instead, investigated the effect of microwave-irradiated thermal reduction with the addition of intercalated benzene in the GO structure. The results of Raman, X-ray spectroscopy (XRS), atomic force microscopy (AFM) and X-ray diffraction (XRD) characterization revealed that by heating the sample up to 400°C with a heating rate of 100°C/min, it is possible to promote benzene pyrolysis, generation acetylene molecules; the latter are then able to react with surrounding defect sites forming new C-C bond [58]. A schematic illustration of the reaction mechanism is reported in Figure 2.5.

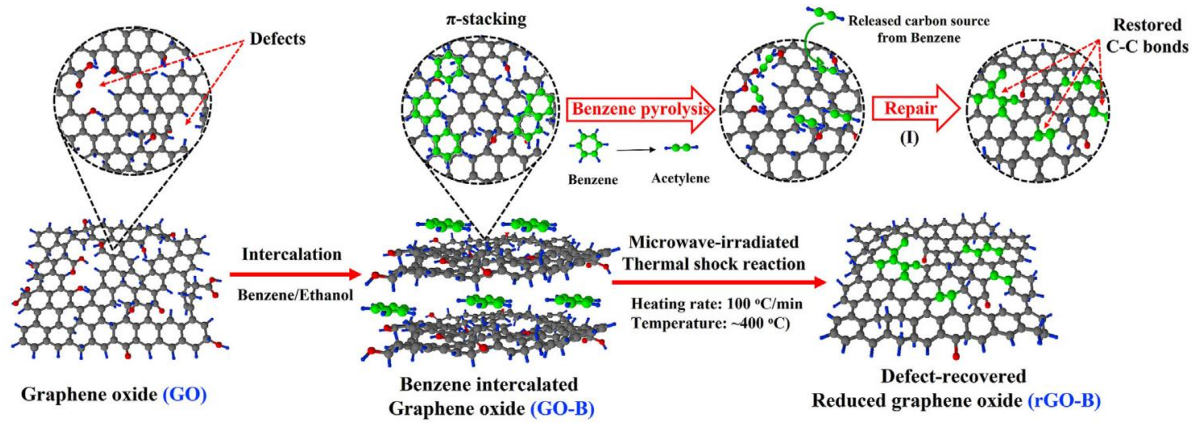

Figure 2.5: Schematic illustration of the reaction between GO and benzene during microwave-irradiated thermal reduction. Adapter from [58].

On the other hand, ethanol is a more traditional carbon source, whose use is well documented in the literature. For instance, De Silva *et al.* demonstrated ethanol vapors effectiveness in restoring the graphitic structure at 800°C, a temperature high enough to remove the majority of oxygen-containing groups and also pyrolyzing the healing species [20]. Kanishka *et al.* obtained a similar result in comparable conditions, confirming that high temperature thermal annealing assisted by ethanol is a suitable high-quality rGO production technique. Gong *et al.*, instead, explored the possibility of using intercalated ethanol for defects repair at low temperatures (200°C). The results of their experimental studies and theoretical simulations are particularly interesting: at 200°C, ethanol does not participate in the reduction reaction as a reductant but interact quite effectively with etch holes caused by CO_2 evolution, and with carbon dangling bonds. Once integrated into the etch holes of rGO, ethanol promotes the formation of a new hexagonal carbon ring. In this way it increases the degree of graphitization of the final product and reducing the risk of defects enlargement caused by migration of epoxides and hydroxyls [56]. In Figure 2.6, the reaction pathways of a etch hole and ethanol is illustrated.

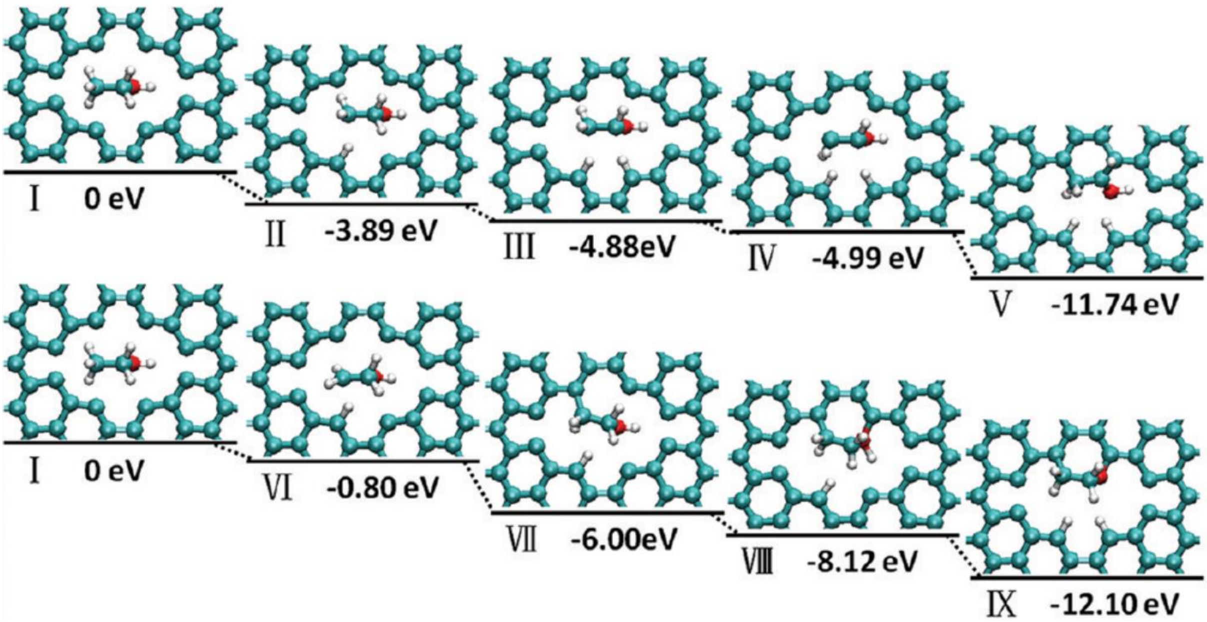

Figure 2.6: Reaction pathways of a etch hole and ethanol. Adapted from [56].

2.1.3.4. Chemical reagent reduction

Chemical reduction of graphene oxide is based on the interaction of the latter with different reducing agent. This reduction technique is particularly popular among scientists because its ease of execution, since it is usually carried out at room temperature or at moderate heating and with basic instrumentation. It also regarded as an effective and scalable procedure of mass producing rGO in cost effective way [39]. So far, it has been proven that many commonly available reductants, such as hydrazine [60], sodium borohydride [61, 62], and hydroiodic acid [46, 63] are able to effectively reduce GO. Among the cited species, hydrazine is reported as the most efficient in the removal of oxygen functional groups [64]. Unfortunately, the use of hydrazine entails several disadvantages: it is a toxic substance, that presents significant environmental and safety risks; it is explosive, making its use unsafe in an industrial setting; it tends to introduce nitrogen doping in the carbon basal plane [65, 66, 67]. Consequently, the research in GO reducing agent is moving in the direction of green substances, such as L-ascorbic acid, L-cysteine, glycine and green tea [68]. L-ascorbic acid (L-AA), also called vitamin C, was proven to be an excellent reducing agent, which allows to achieve high C/O ratios and conductivity values comparable to those obtained with hydrazine [64, 62, 69]. Besides being non-toxic, highly efficient, and not pollutant, this chemical is soluble not only in water, but also in common organic solvent such as N,N-dimethylformamide (DMF) and N-methyl-2-pyrrolidone (NMP) . This aspect has been fundamental in this work, as explained in Section 3.2.5.

The mechanism of reduction of graphene oxide through L-ascorbic acid is still partially unknown but it can be speculated with a good degree of certainty that two different reactions take place on the surface of GO sheets. Both the reactions are triggered by the dissociation of L-AA, caused by the electron density withdrawing from the substituted furan, which gives a strongly acidic character to the two hydroxyls groups. The protonation of GO's reactive groups, i.e., vicinal hydroxyls and epoxides, follows, accompanied by the attacks of the nucleophilic agent (i.e., the oxyanion of L-aa: $C_6H_7O_6^-$) on the sp^2-carbon of the epoxy group or the sp^3-carbon of the hydroxyl group. Hydroxyl and water are the byproduct of this first reaction. The epoxy-oxyanion intermediate goes through a second condensation, and, after that, a thermally induced red-ox reaction finally yields reduced graphene oxide (r-GO), dehydroascorbic acid and water molecules [64, 68]. Figure 2.7 and Figure 2.8 report a schematic representation of the reaction biproduct and the reaction pathway, respectively.

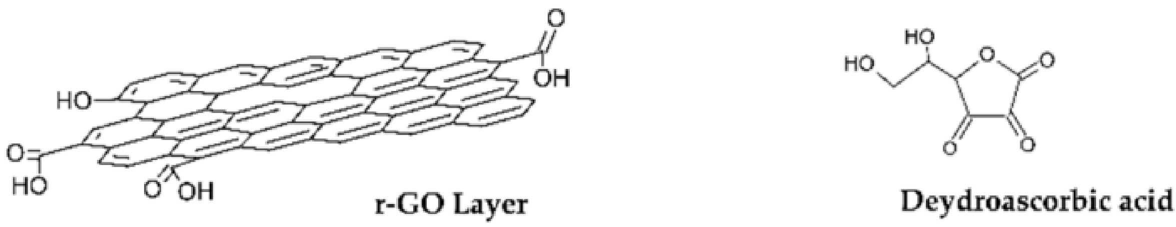

Figure 2.7: Byproduct of GO reduction with ascorbic acid [68].

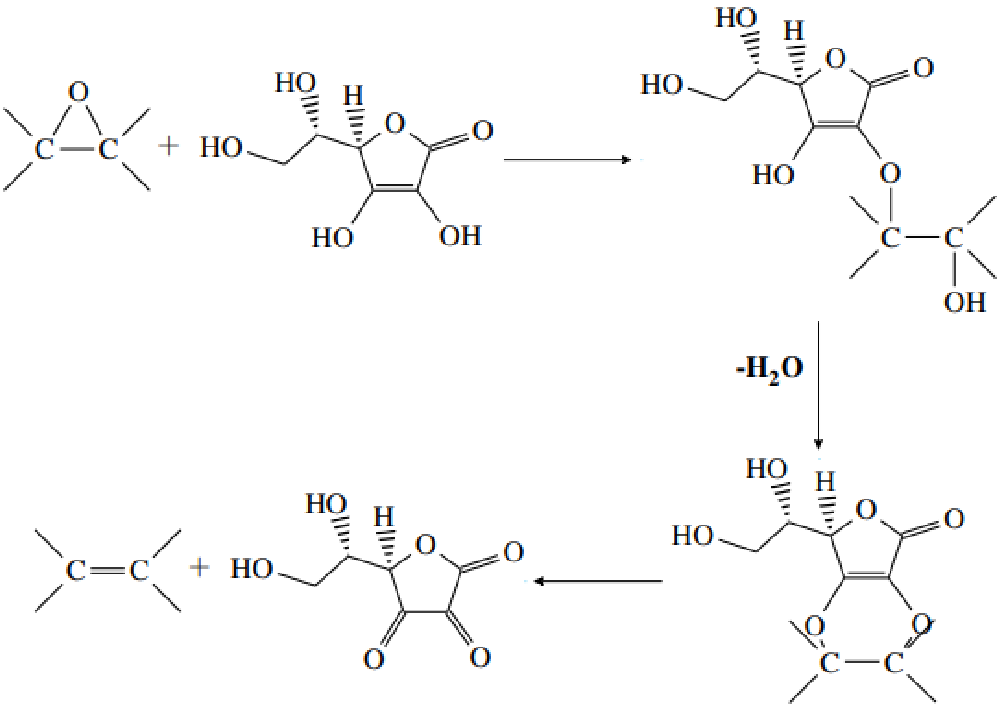

(a) Reduction of epoxy groups

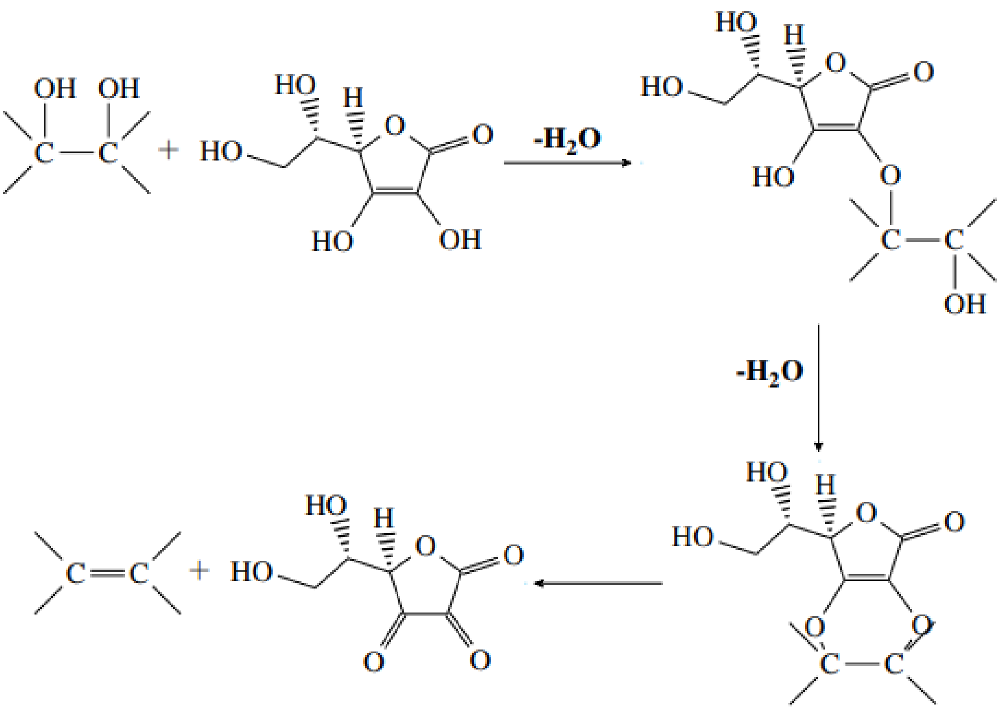

(b) Reduction of hydroxyl groups.

Figure 2.8: Schematic of reaction pathway for the chemical reduction of graphene oxide with L-ascorbic acid. Adapted from [67].

2.2. Lead sulphide nanoparticles

During the last two decades, semiconductor-based gas sensors have gained considerable attention thanks to their ease of application in gas monitoring devices and their inexpensiveness compared to other options available on the market. One of the most effective strategies to enhance semiconductors sensing capabilities is to utilize them in their nanostructure form. By doing so, the surface-to-volume ratio is increased, thus allowing a more efficient interaction with the target gas, and the electronic properties can be controlled by tuning the size and shape of the nanoparticles (NPs). Among different types of semiconductors, metal oxides and semiconducting chalcogenide proved to be good candidates for gas sensing application. For instance, SnO_2 and ZnO, belonging to the former group, present fast response and recovery time and good sensitivity to many dangerous volatile organic compounds (VOCs), such as CO, CO_2, C_2H_6O and CH_4 [70, 71, 72, 73]. However, despite their appealing characteristics, metal oxides operate well only at high temperatures, provided by power-hungry heating elements. This aspect limits their employment in explosive and flammable gaseous environments [74]. On the contrary, some semiconducting chalcogenides, tested for the detection of gases like NH_3, NO_2, C_2H_6O and CH_3OH, show good sensitivity even at room temperature [75, 76, 77]. In particular, several studies report high sensitivity, full recoverability and rapid response of lead sulphide NPs-based sensors towards many of the species just listed [78, 79, 80, 75].

Relatively recent studies have highlighted the possibility of employing nanostructured PbS in methane sensors. Methane is a colorless, odorless and highly explosive gas that is frequently used in industrial and household settings, whose low explosive limit (5% in air) has prompted scientists to look for effective solutions for its detection. With this goal in mind, a variety of sensing techniques have been developed, including piezoelectric, electrochemical, spectroscopic, solid-state, chromatographic, and metal oxide-based sensing devices [25]. However, due to the limited sensitivity of these systems or their high energy consumption, scientists have turned their attention to nanostructured lead sulphide, which stands out for its sensitivity at ambient temperature and simplicity of production. Given the promising results reported in literature [78, 79, 80, 75], lead sulphide nanoparticles have been employed in this work for the decoration of reduced graphene oxide flakes, to show how the latter may be used for gas sensing applications.

2.2.1. Properties of lead sulphide nanoparticles

Lead sulphide is a chalcogenide semiconductor characterized by a narrow direct band gap ~ 0.4 eV, high charge carrier mobility equal to 0.44 $cm^2 \cdot V^{-1} \cdot s^{-1}$, and a large exciton Bohr radius of 18 nm, which implies strong quantum confinement of both electrons and holes at relatively large size [81, 82]. Lead sulphide's structural, thermal, optical, and electrical properties are size dependent, meaning that by transitioning from a 3D (bulk PbS) to a 0D system (quantum dots, QDs) it is possible to tune these properties to makes PbS structures suitable for a wide range of applications. In particular, one of the most interesting aspects of reducing the lead sulphide size down to the nanoscale is the opening of the electronic and optical band gap, which completely change the absorbance spectrum and the conductivity of the system. For instance, a good correlation between PbS quantum dot size and band gap energy is provided by Equation (2.3), formulated by Moreels and colleagues by fitting experimental data collected on quantum dots (size range fitted: 3.9-13.3 nm) [83]:

$$E_0 = 0.41 + \frac{1}{0.0252d^2 + 0.283d} \tag{2.3}$$

Where d is the diameter of a quantum dot. Other research group demonstrated that also the degree of charge transfer between a molecule (4-Mpy in their study) and PbS QDs is size dependent: Fu *et al*. were able to determine that the maximum degree of charge transfer is reached at 8.9 nm in diameter, while for smaller particles it rapidly decreases [84]. This aspect is particularly important in case of PbS application in gas sensing devices since the primary sensing mechanism is given by the interaction of the nanoparticles with the target gas through charge transfer.

Finally, to ensure the ideal operating conditions for the devices in which PbS nanoparticles are integrated, it is crucial to evaluate their thermal and oxidative stabilities, heavily influenced by the large specific surface area. Sadovnikov and colleagues [85] tested the lead sulphide nanoparticles by annealing them in vacuum or air and recording the variation in particles size and PbS content (Figure 2.9). The results of their experiments suggest that, in vacuum conditions, lead sulphide nanopowders are thermally stable up to 700 K, temperature over which recrystallization takes place. In oxygen-full environments, instead, the early phases of lead sulfide oxidation yield lead sulfate, via the reaction in Equation (2.4):

$$PbS + 2O_2 = PbSO_4 \tag{2.4}$$

As the temperature rises to 623 K, lead oxide begins to develop, only to disappear at higher temperatures. In the end only PbS and $PbSO_4$ are left, in agreement with the theory of metal sulfide oxidation, according to which sulfate formation is just an intermediate stage [86].

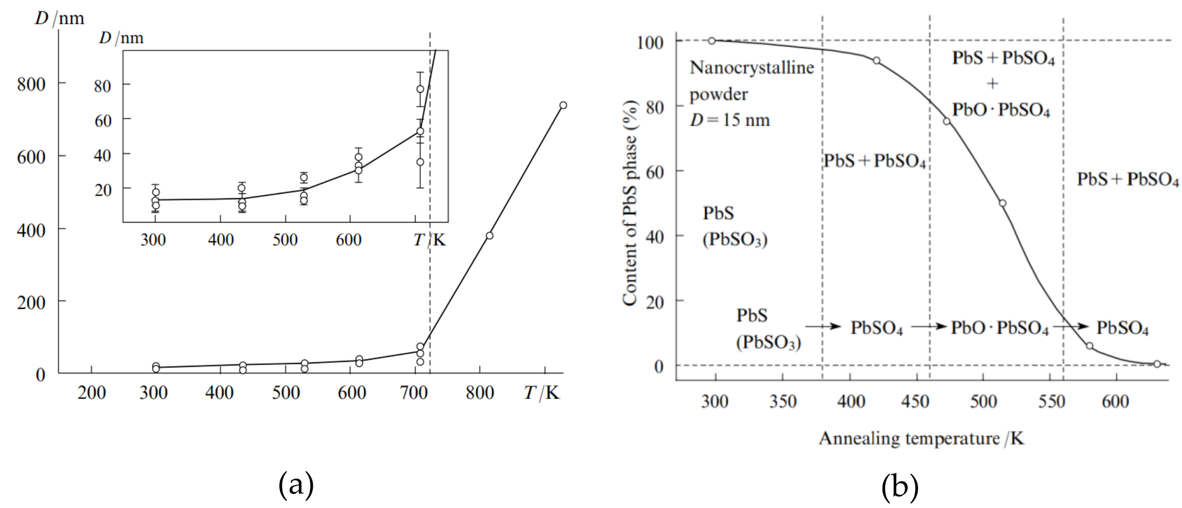

Figure 2.9: Plot of (a) effect of vacuum annealing temperature on PbS particles size and (b) content of PbS phase in PbS powder vs. annealing temperature in air [85].

Since methane sensors' typical working temperature falls within the thermal and oxidative stability range of lead sulfide, modest temperature increases have no detrimental effects on gas detection activities, even in an air environment.

2.2.2. Synthesis of lead sulphide nanoparticles

Great efforts have been made over the last three decades to create viable synthetic techniques to produce high quality, crystalline semiconductor nanocrystals with tunable physical and chemical characteristics. The synthesis routes reported in literature are often classified into four types, based on the condition of the reaction medium: vapor-phase, solid-phase, liquid-phase, and two-phase approach. However, vapor-phase and solid-phase synthesis are often characterized by poor control over the nanoparticles' size and shape, making them inadequate for the accurate and reliable synthesis of well-defined NPs. On the contrary, the liquid phase approach proved to be an efficient method for nanoparticles synthesis. In particular, solution-phase synthesis of lead chalcogenides, based on a two-stage process for NCs' formation (i.e., nucleation and crystal growth), allows for good control over particles' size, shape and density by adjusting three key reaction parameters: reagents' concentration and activity, injection temperature and reaction time [87]. An interesting approach to lead sulphide NPs production is presented by the highly reproducible and inexpensive one-pot method, consisting in the synthesis of colloidal PbS nanoparticles directly in an aqueous medium [88]. This synthetic method, usually performed at room temperature, require the use of water-soluble reagents and the addition of a capping agent, introduced to control nanocrystal size and avoid their aggregation, which may cause surface imperfections and charge carriers localization [89]. The probability of occurrence of side reaction, resulting in the formation of hydrates or hydroxo complexes have been explored by Kozhevnikova *et al.*; they conclude that, given the reversibility of most of the side reactions, PbS synthesis in aqueous medium is feasible [88]. At last, Mishra and colleagues, evaluated the influence of the previously mentioned reaction parameters in a simple chemical synthesis of PbS NPs. The results of their study revealed that temperature and growth time control the nanoparticles size, while their shape changes by varying the reagent-to-reducing agent ratio [90]. As a result, by changing these parameters diverse morphological, optical, and structural properties of nanostructures may be obtained.

2.3. Sensing mechanism of PbS/rGO methane sensors

The gas sensing mechanism of PbS nanoparticles is a fairly known process, which starts with the absorption of oxygen atoms on the surface of the NCs. According to several studies, the O_2 molecules that interact with the NPs at their surface act as acceptor dopants, changing an inherently N-type semiconductor into a P-type semiconductor [91, 80, 25, 75]. When methane is later introduced in the atmosphere, it promotes the desorption of oxygen from the PbS NCs surface, which causes the release of negative charges that triggers electron-hole recombination. Consequently, as response to the decrease in concentration of the majority carriers (holes), the resistance of the semiconductors increases [75]. Figure 2.10 highlights the difference in resistance variation for a p-type and n-type semiconductors exposed to a target gas.

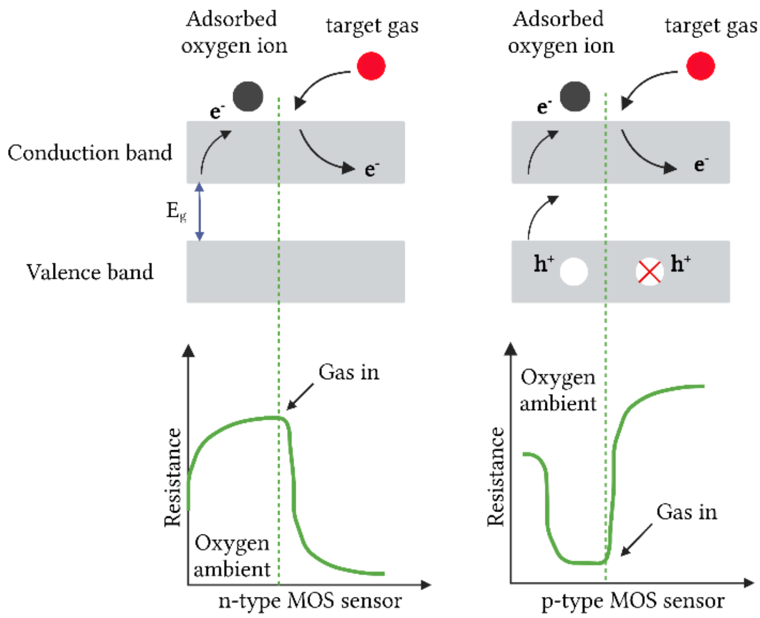

Figure 2.10: Difference in resistance variation for a n-type and p-type semiconductors exposed to a target gas. Illustration adapted from [92].

An interesting study conducted by Mosahebfard and colleagues shows that methane adsorption onto O_2-adsorbed PbS clusters is far more likely to take place than methane adsorption onto pristine PbS clusters. They reached this conclusion by evaluating the binding energies of the PbS/O_2/CH_4 and PbS/CH_4 systems (5.77 eV and 0.176 eV, respectively), and by comparing HOMO–LUMO theoretical calculations of PbS cluster, PbS/CH_4, PbS/O_2 and PbS/O_2/CH_4 systems with their experimental observations [93]. Given the limited charge transfer between neighboring PbS nanoparticles, it is convenient to introduce conductive rGO flakes to enhance the carrier transportation. Indeed, when PbS nanoparticles are deposited on reduced graphene oxide flakes, a variation in the majority carriers of PbS NCs, caused by O_2-absorbance, leads to a change in the carrier concentration of rGO flakes too. In particular, the equating of the Fermi levels of the two components, linked to the band bending of the energy levels, causes further holes accumulation in PbS NCs valence band. When the PbS/rGO system is exposed to methane, the injection of electrons in PbS NCs results in a decrease of the majority carriers of the rGO sheets and ultimately in an increase of its overall resistance. The fast carrier transportation to the electrodes provided by the percolative path on the rGO flakes allows for a quicker response and higher sensitivity at lower methane concentration, compared to a more traditional sensor composed just of nanoparticles [25].

3 Experimental Methods

The experimental methods and the characterization techniques employed for the synthesis and characterization of GO, rGO and PbS nanoparticles are illustrated in this chapter. First, a description of the substrates and the technique for their preparation is presented, followed by a detailed explanation of the procedures employed for the production of the GO dispersions and their deposition. The processes of GO's thermal annealing, healing treatment and chemical reduction are outlined. Afterwards, a thorough account of the synthesis procedure for lead sulphide nanoparticles is reported, as are the details about PbS's ink production and deposition.

The second section is dedicated to the description of the characterization methods employed in this work, such as scanning electron microscopy (SEM), Raman spectroscopy, X-ray photoelectron spectroscopy (XPS), X-ray diffraction (XRD) and X-ray Fluorescence (XRF), electrical measurements and finally gas sensing measurements.

3.1. Chemicals

The chemicals used in this thesis are presented in Table 3.1. Milli-Q water, ammonia and N-Methyl-2-pyrrolidinone were employed to prepare solutions and reaction mixtures. Benzene and absolute ethanol were used as carbon source during healing treatments. Lead(II) nitrate, sodium sulphide and 2-Mercaptoethanol were utilized as lead source, sulfur source and capping agent, respectively. Chemical reduction was performed with L(+)-Ascorbic acid dissolved in NMP. Three graphene oxides sources, provided by different suppliers and exhibiting distinct chemical and morphological structures, were tested for the for the production of the gas sensors.

Table 3.1: Chemicals employed in this work.

Chemical	Chemical Formula	Supplier	Additional information
Benzene	C_6H_6	VWR Chemicals	Reagent grade
Absolute Ethanol	CH_3CH_2OH	VWR Chemicals	Reagent grade
Ammonia	NH_4OH	Chem-Lab NV	25% weight solution
N-Methyl-2-pyrrolidone	C_5H_9NO	Acros Organics	HPLC Solvent
Lead(II) nitrate	$Pb(NO_3)_2$	Sigma-Aldrich	99.999% trace metals basis, water soluble
Sodium sulphide	Na_2S	Sigma-Aldrich	Water soluble
2-Mercaptoethanol	C_2H_6OS	Sigma-Aldrich	14.3 M (pure liquid), Reagent grade
L(+)-Ascorbic acid	$C_6H_8O_6$	VWR Chemicals	99.0-100.5% USP
Graphene oxide	-	Graphenea	Powder
Graphene oxide	-	Sigma-Aldrich	Water dispersion, 1 mg/mL
High-temperature annealed graphene oxide	-	Angstron Materials (US)	High-temperature annealed graphene oxide, powder

3.2. Sample preparation, reduction techniques and synthesis procedure

3.2.1. Substrate cleaning and preparation

Single-side polished (SSP) flat prime-grade silicon/silica wafers were used as main substrates for the characterization of graphene oxide flakes and lead sulphide nanocrystals. The wafers, which came in a 4" diameter, with a 500-550 μm thick central silicon layer and 2850 Å ± 5% wet thermal oxide layers on both sides (0.001-0.005 Ω·cm resistivity), were subsequently cut into ~ 0.5 cm² pieces for easy handling. Afterward, the substrates were thoroughly cleaned, first in acetone to remove any trace of organic contamination, then with methanol and finally with deionized and distilled water, to remove residual particles.

Ready-made CMOSEnvi™ dies (patented VOCSens) were also employed for characterization purposes but they were mainly utilized as substrates for the production of the final devices. A schematic drawing of the dies is reported in Figure 3.1.

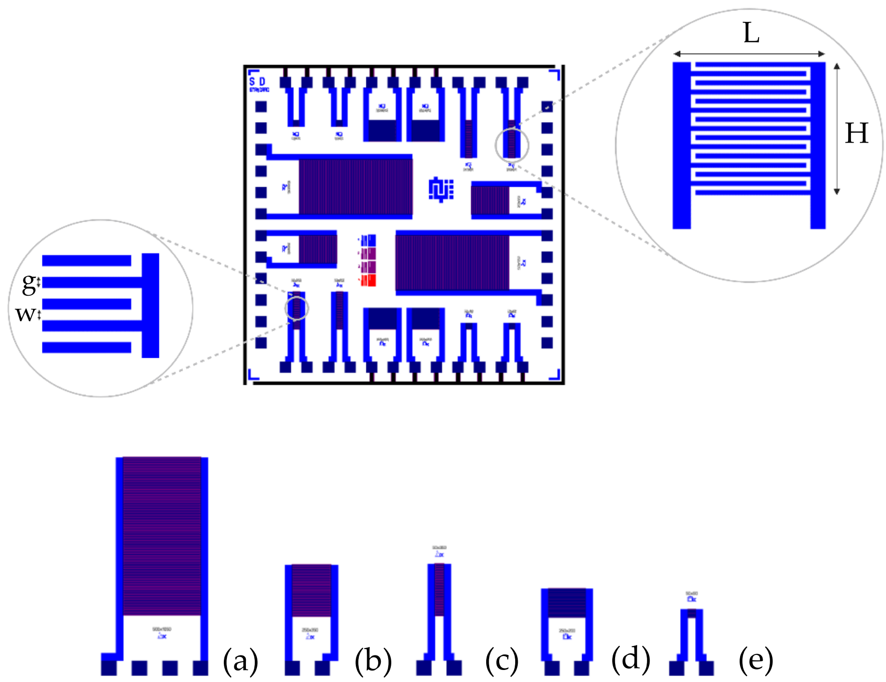

Figure 3.1: Schematic representation of patented VOCSens CMOSEnvi™ die; (a)-(e) interdigitated electrodes (IDE) patterned on the dielectric substrate.

The CMOSEnvi™ were fabricated starting from a 400 μm thick, <100> oriented silicon layer, N-doped with phosphorus (2-3 Ω·cm resistivity), on top of which a 300 nm thick silicon oxide layer was grown. Ti:Au (200:2000 Å) metallic lines were then patterned on top of the insulating layer, with a width of 2 μm and with a gap of 5 ± 1 μm between each other. The dies came with a top protective blue coating, removed by immersion in a hot acetone bath (80°C). A washing with methanol and Milli-Q water followed to ensure a clean surface.

Graphene oxide and lead sulphide nanocrystals were deposited on electrodes (a)-(b)-(c) (Figure 3.1), the specifics of which are stated in Table 3.1.

Table 3.2: Details about the interdigitated electrodes (IDE).

Electrodes	Number of fingers	Length (L) [μm]	Hight (H) [μm]
(a)	150	500	1050
(b)	50	250	350
(c)	50	50	350
(d)	50	200	250
(e)	15	50	60

3.2.2. Preparation of diluted graphene oxide dispersions

As mentioned in section 3.1, three graphene oxides suppliers have been considered in this research. In order to provide GO dispersion with the most suitable characteristics (dispersibility, concentration and flakes size) for the intended purpose, solutions with different solvents, concentration and sonication time were produced.

Morphological and spectroscopic studies required relatively high concentration solutions of graphene oxide, to easily identify it on the surface of the substrates, once drop casted. Hence, the GO powders provided by Graphene were dispersed in Milli-Q water with a concentration of 0.5 mg/mL and 0.25 mg/mL; to break the clustered GO, improve the dispersion of GO sheets, and reduce the dimension of the biggest GO flakes, ultrasonic treatment (USC1200D, VWR International) at 45 kHz and 60 W was performed for 15 to 60 minutes. The same procedure was employed for the production of solutions with rGO powders provided by Angstron Materials. However, the loss of surface polarity, caused by the lower number of oxygenated groups on the surface of the GO sheets, increases its hydrophobicity, which negatively affects the homogeneity of the material once drop casted. Small amount of aqueous ammonia (~100 μl / 10 mL) was added in order to adjust pH value, promoting the colloidal stability of GO sheets. Additionally, N-Methyl-2-pyrrolidone, already proven to provide long-term stability for both graphene oxide and reduced graphene oxide, was tested for the production of rGO dispersions, with the same concentration as the aqueous dispersion [94]. Given the results of the morphological studies on the Angstron Materials' GO powders, that are going to be presented in the next chapter, ultrasonic treatment was performed for longer period of time, up to 4 hours at 45 kHz and 60 W. Finally, Sigma-Aldrich GO, provided in the form of water dispersion with a concentration of 1 mg/mL, was diluted down to 0.5 mg/mL and 0.25 mg/mL. Different sonication times were tested to obtain a homogeneous dispersion of small flakes, from 10 minutes to 90 minutes.

Experiments on the healing effect of ethanol and benzene were completed starting from 0.25 mg/mL aqueous solution of the three graphene oxides, that were then mixed with 0.25 mg/mL of absolute ethanol/Milli-Q water solution and absolute benzene/Milli-Q water solution in a 1:1 volume ratio. The mixing procedure was done directly in the syringe employed for the drop casting on the substrates.

Thermal reduction experiments were conducted on aqueous solutions of the three graphene oxides with a 0.25 mg/mL concentration, sonicated for 60 minutes.

Lastly, a 0,025 mg/mL solution of GO from Graphenea was produced by diluting the supernatant of a 0,1 mg/mL solution (agitation by hand of the bottle and extraction after 10 minutes) already subjected to ultrasonic treatment at 45 kHz and 60 W for 30 minutes (USC1200D, VWR International). To further reduce the size of the flakes, the diluted dispersion was then sonicated for 60 more minutes at 37 kHz and 126 W (Elmasonic P60H). This last GO solution was intended for chemical reduction experiments.

3.2.3. Deposition technique

Both graphene oxide and lead sulphide nanocrystals dispersion were deposited through drop casting. The drop casting station, schematized in Figure 3.2, was supplied with a bench stereomicroscope, equipped with a movable sample platform and two adjustable lamps, and a ceramic heating element, on which the substrate was sticked with a small amount of conductive silver paste. A power supply unit (RSPD

3303C) and a digital multimeter (DMM) (RSPD 3303C), placed on the side, were connected to the heating element and a thermocouple.

The solutions were drop casted on the substrate trough a 0.3 mL insulin syringe with sterile interior, the needle of which, having a diameter of 0.25 mm, was cut straight. The volume of the droplets varied between few µL to hundreds of nL.

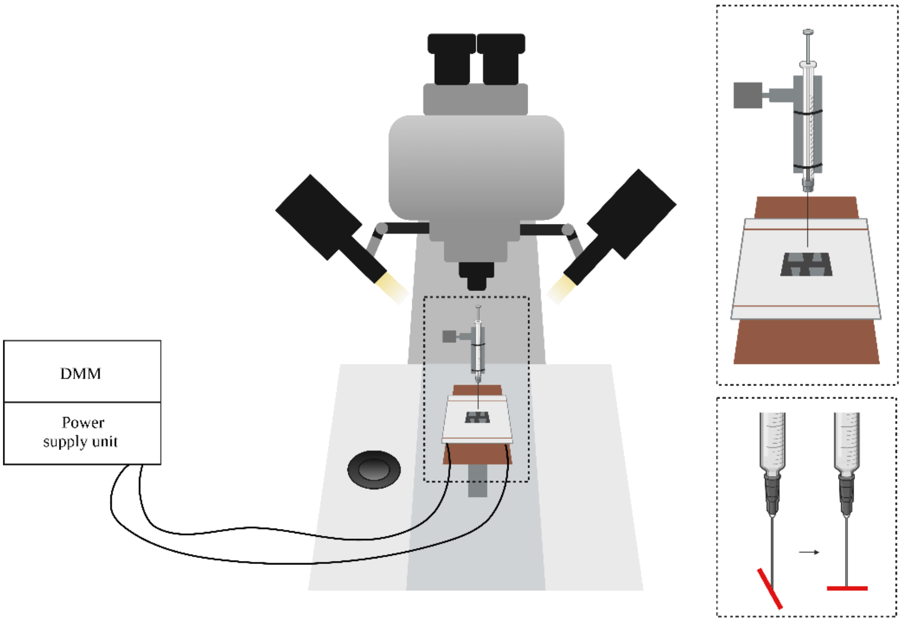

Figure 3.2: Schematic representation of the drop casting station.

3.2.4. Graphene oxide's thermal annealing and healing treatment

Once the wire bonding to the dual inline packaging was completed, being careful to perform this operation at lower temperature than usual (~ 100°C) to prevent any pre-annealing (Figure 3.3), the die was ready to be placed the vacuum chamber for the thermal annealing.

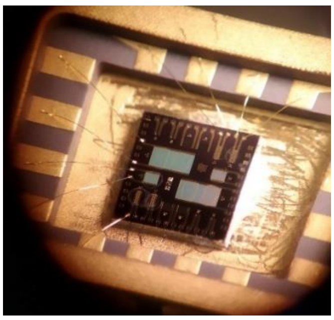

Figure 3.3: Wire bonding of sensors on the packaging.

The vacuum chamber was equipped with both a dry scroll vacuum pump (Edwards XDS10, ultimate vacuum= $6 \cdot 10^{-2}$ mbar) and a turbomolecular pump (Pfeiffer Balzers

TPU 240, PMP 01 330, ultimate pressure= 10^{-8}-10^{-9} mbar). An infrared lamp (64635 HLX, Osram), powered by a bench power supply unit (72-2925 Single Output DC Bench Power Supply, Tenma) was positioned on top of the transparent lid to heat the substrate up to the desired temperature, monitored with a thermocouple. The resistance variations were recorded by DMM (2110 5 ½ Digit Multimeter, Keithley). A schematic representation of the thermal annealing and healing treatment station is reported in Figure 3.4.

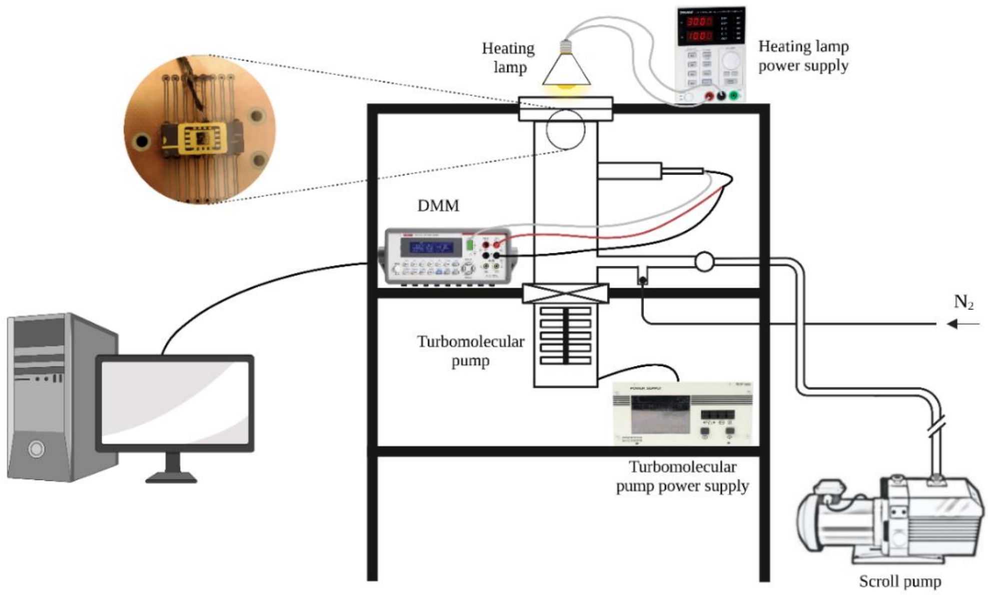

Figure 3.4: Schematic representation of the thermal annealing and healing treatment station.

The description of the selected temperature profile follows:

1. the first step consists in a 30-minutes heating at 80°C, to promote the evaporation of any residual liquid from the surface of the die;

2. the second step brings the system to 320°C, the maximum temperature reached during the process. Such temperature, maintained for 3 hours, was chosen to avoid damages to the structure of the IDEs; however, in literature [39, 44] is reported that, even at lower temperatures, a large number of functional groups could be easily removed, without extreme damages to the structure of graphene oxide's sheets. Given the unsatisfactory results (Section 4.1.2) of the resistance measurements, the annealing time of the GO-Graphenea based sensor was increased to 8 hours.

3. a rapid cooling follows. When the thermocouple registers a temperature around 30°C, it is possible to open the lid and extract the die.

3.2.5. Graphene oxide's solvothermal annealing and chemical reduction

To evaluate the performance of Vitamin C towards the reduction of graphene oxide, the latter was reduced at different temperature for 30 minutes. Samples intended for XPS characterization were produced by reducing GO dispersions (0.1 mg/mL), while GO meant for Raman spectroscopy and IV curve acquisition was reduced when already drop casted on IDEs (0,025 mg/mL). For comparison purposes, a simple solvothermal annealing in NMP and a healing treatment with ethanol were carried out by heating the dispersion at 199°C. Ascorbic acid and absolute ethanol concentrations were set at 0.8 M [95]. Details about the experiments are reported in Table 3.3.

Table 3.3: Details about the reduction reactions.

Type of treatment	Solution	Temperature
Chemical reduction	Milli-Q water/L-Ascorbic acid (0.141 g/mL)	80 °C
Chemical reduction	NMP/Ascorbic acid (0.141 g/mL)	80 °C
Chemical reduction + Solvothermal annealing	NMP/Ascorbic acid (0.141 g/mL)	199 °C
Solvothermal annealing	NMP	199 °C
Healing treatment	NMP/absolute ethanol (0.369 g/mL)	199 °C

After the reduction process with ascorbic acid, it was possible to visually recognize the increase in hydrophobicity of the dispersed rGO caused by the reduction of oxygenated group on its surface.

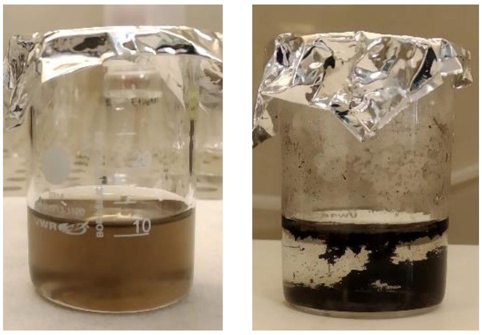

(a) (b)

Figure 3.5: GO dispersion in Milli-Q water before (a) and after (b) reduction with ascorbic acid at 80°C.

After the completion of the five treatments, the dispersions were centrifugated (15 minutes, 6000 rmp) and washed three times with Milli-Q water, to remove most of the ascorbic acid, ethanol and NMP residues. After the last centrifugation the deposit was separated from the liquid phase and completely dried. The dies, instead, were washed in acetone, methanol and water and then dried at 200°C for 30 minutes in the vacuum chamber described in Section 3.2.4.

3.2.6. Lead sulphide nanoparticles synthesis and drop casting

Lead sulphide nanocrystals were synthetized following an easy room temperature process, as described in [80, 75, 25]. Lead (II) nitrate ($Pb(NO_3)_2$), sodium sulphate (Na_2S) and 2-mercaptoethanol ($HOCH_2CH_2SH$) (14.3 M), all provided by Sigma-Aldrich, were employed as lead source, sodium source, and capping agent, respectively.

First, 1.53 g of $Pb(NO_3)_2$ was dissolved in 50 mL of degassed milli-Q water (0.1 M concentration) and introduced into a triple-neck round-bottom flask kept under argon flow, to prevent products oxidation. Then, 100 mL of 0.1 M 2-mercaptoethanol solution was introduced dropwise in the reaction flask via a separatory funnel under stirring. The dropwise addition of the capping agent took ~ 1 hour to be completed. Finally, a solution of 360 mg of sodium sulphate dissolved in 50 mL of milli-Q water (0.1 M concentration) was introduced in the flask dropwise in the course of ~ 4 hours. The sudden change of colour of the liquid after only few droplets (~ 15-20 droplets) of Na_2S solution were introduced is a good indicator of the reaction taking place. The mixture was stirred for ~ 10 hours to ensure the completion of the reaction, reported in Equation (3.1):

$$Pb(NO_3)_{2\,(aq)} + Na_2S_{\,(aq)} \rightarrow PbS_{(s)} + 2NaNO_{3\,(aq)} \tag{3.1}$$

The removal of byproducts and residual organic capping was achieved by repeating three times the centrifugation of the mixture (6000 rmp, 15 minutes) followed by washing with fresh Milli-Q water. The solution was then centrifuged one last time to remove the PbS from aqueous media. The wet paste was later dried in a furnace (Carbolite GSM 11/8) set at 50°C for 10 hours and crushed with mortar and pestle until obtaining a fine powder. The theoretical yielding of the reaction is 1.11 g of lead sulphide. Figure 3.6 shows a complete flow chart of the preparation PbS nanocrystals by chemical synthesis.

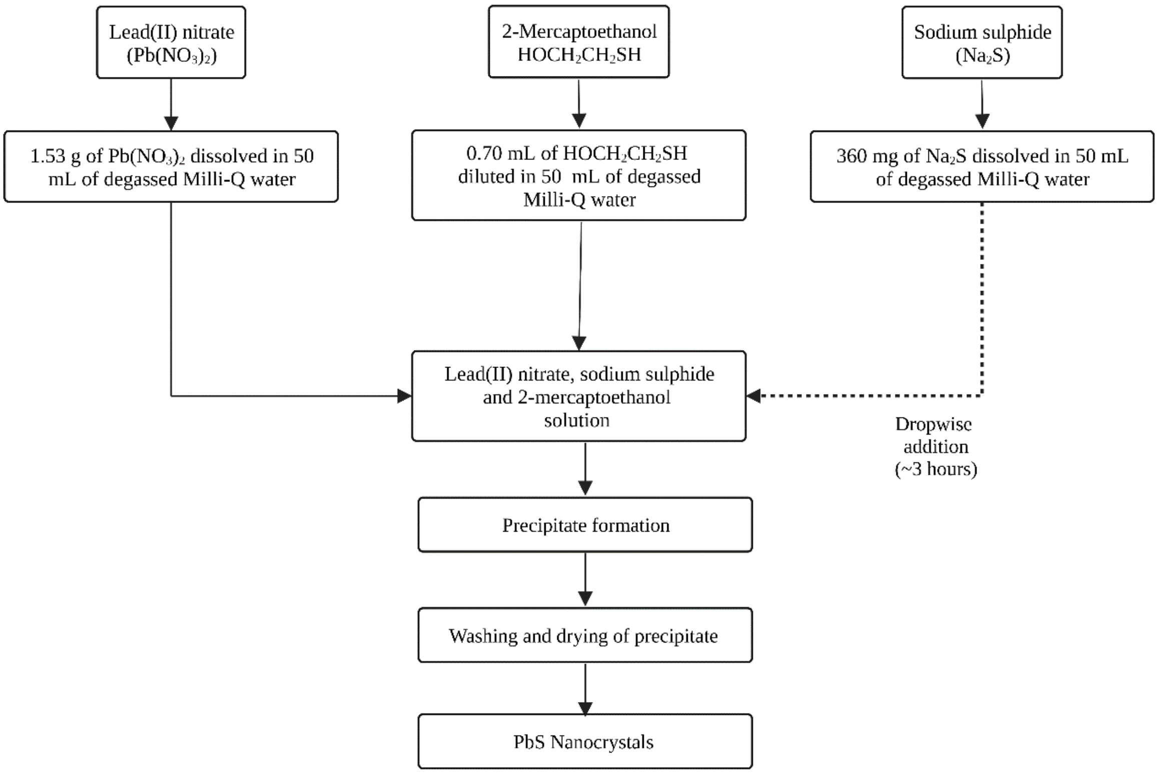

Figure 3.6: Flow chart of the preparation PbS nanocrystals by chemical synthesis.

The powders synthetized with the procedure hereby described were then employed for the production of inks to be drop casted on top of graphene oxide flakes, deposited on interdigitated electrodes. The inks were obtained by adding to 4 mL glass vials 3 mL of Milli-Q water and 15 mg of PbS powder. In order to obtain a homogeneous solution and shutter the biggest clusters, the vials were sonicated for 4 hours in an ultrasonic bath (USC1200D, VWR International) at 45 kHz and 100 W. The temperature of the water in the bath was kept under 30°C by adding ice, to avoid possible annealing of the nanocrystals.

The dispersion was later drop casted on top of the reduced graphene oxide flakes at the station described in Section 3.2.3, by extracting ~ 0.15 mL of the supernatant (agitation by hand of the bottle and extraction after 10 minutes). The remaining capping agent surrounding the nanoparticles was then removed by washing the dies in acetone, methanol, and water. A final drying at 80°C in the vacuum chamber allowed the evaporation of residual water particles, while a treatment at 280°C promote the reduction of the nanoparticles and consequently the removal of the natural oxide layer. This final treatment completed the production process of the supposed sensor.

3.3. Characterization methods

In this paragraph, the main characterization technique employed in the analysis of the graphene oxide flakes and lead sulphide nanoparticles are going to be reviewed. First, scanning electron microscopy (SEM) was employed to evaluate the morphology, the size and the thickness of the graphene oxide flakes, to assess the diameter of the PbS NPs and verify the decoration of the GO films with the latter. Raman spectroscopy was used to investigate the structural properties and the defectivity of the graphene oxide before and after each treatment. Carbon/oxygen ratio and degree of graphitization were studied through X-ray photoelectron spectroscopy. The degree of reduction of the graphene oxide flakes was further evaluated through resistance measurements. Finally X-ray fluorescence spectroscopy (XRF) and X-ray diffraction spectroscopy (XRD) were utilized to assess the composition and verify the crystallinity of the lead sulphide powders.

3.3.1. Scanning Electron Microscopy

Scanning electron microscopy (SEM) is a type of microscope that makes use of a collimated beam of electrons to obtain images of samples with a resolution down to the nanometer scale. The large depth of field and the high control on the degree of magnification makes this powerful tool suitable for surface morphology characterization, fracture analysis, surface contamination assessment and semiconductor inspection [96].

Generally, the beam of high-energy electrons is generated by an electron source (thermionic and field emission sources are the most common ones) and focused on a small spot on the surface of the sample by means of magnetic lenses. Figure 3.7 shows a schematic representation of the SEM components.

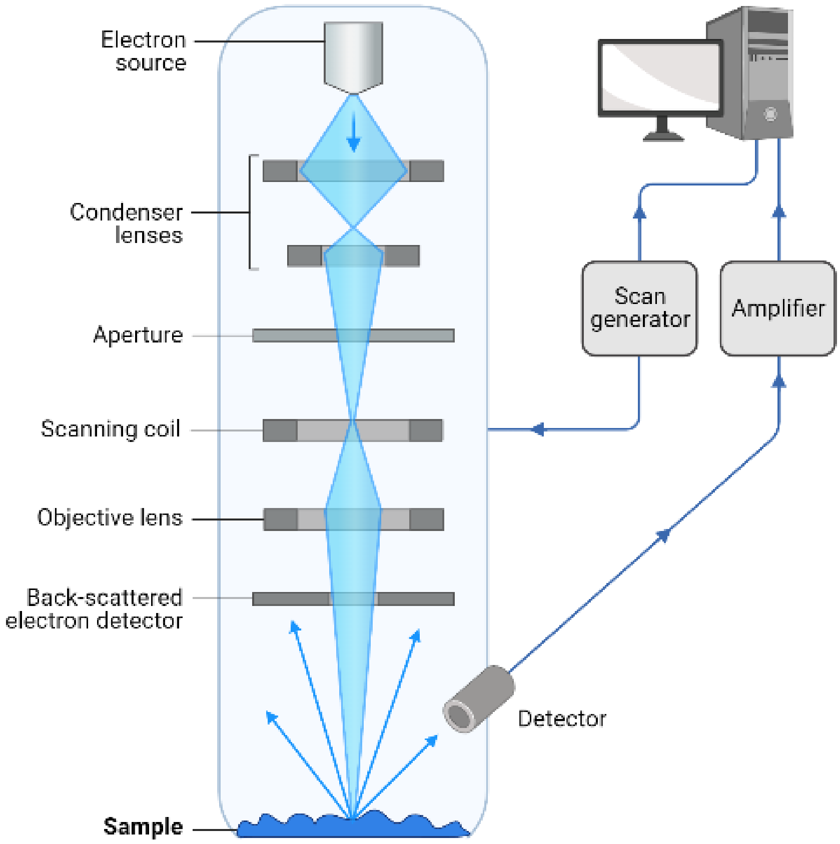

Figure 3.7: Schematic of a scanning electron microscopy. Reproduced from [97].

The interaction of the collimated electron beam with the surface of the sample produces different types of signals which are evaluated for the imaging process as presented in Figure 3.8. Elastic interactions generate the so-called back scattered electrons (BSEs), beam electrons deflected from the surface of the sample without energy loss. On the contrary, inelastic interactions cases the transfer of energy from the impinging electrons to the surface atoms. As result, low-energy secondary electrons (SEs) originated from the surface layer of the sample [98]. The former signal provides compositional information and lower resolution images, while the latter supplies topographic information [99].

Other signals are produced from the inelastic interaction between the electrons and the surface specimen – cathodoluminescence (visible light fluorescence), characteristic X-ray radiation and Auger electrons – but are rarely detected in a standard equipment.

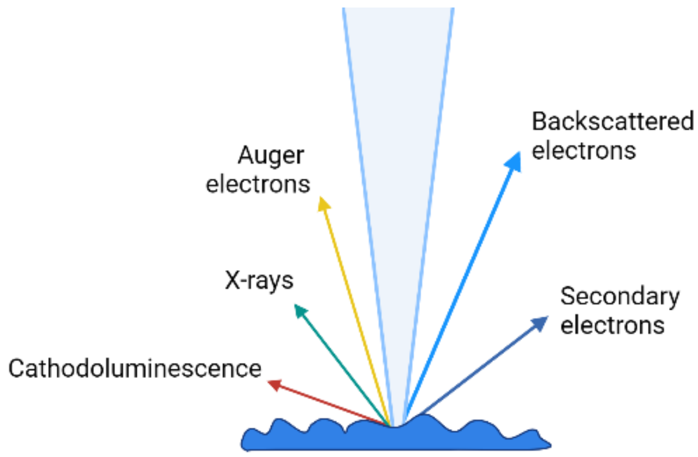

Figure 3.8: Schematic of electron-matter interaction.

The output signals from the SEs and BSEs detectors are amplified and shown on the display unit. Raised surface and insulating materials appear as brighter areas, because of a higher amount of impinging electrons and charging effect, respectively.

A ZEISS Gemini scanning electron microscope with InLens and Secondary Electrons Secondary Ions (SESI) detectors was employed in this work. The samples were mounted on a stainless-steel specimen holder by means of double-face adhesive carbon tape and introduced in the vacuum chamber of the microscope. Images were acquired using an electron high tension (EHT) voltage between 3 and 7 eV at short working distance.

3.3.2. Raman Spectroscopy

Raman spectroscopy is a well-established non-destructive technique for material characterization. It involves the irradiation of the sample surface with a monochromatic laser of frequency ν_0, causing the excitation of molecules from their starting energy level to a virtual energy level. When the excited molecules decay to a lower energy level, light is re-emitted with a frequency dependent on the scattering phenomena that has taken place. Three cases can be distinguished:

1. if the molecule decays to the initial vibrational state, elastic scattering or Rayleigh scattering occurs with the diffusion of a photon of the same energy as the excitation photon;
2. if the molecule presents a higher vibrational energy after revolving back to a lower energy level, inelastic scattering or Stokes scattering occurs with the diffusion of a photon of lower energy as the excitation photon;

3. if the vibrational energy of the molecule decreases with respect to the initial one after decaying, inelastic scattering or anti-Stokes scattering occurs with the release of a photon of higher energy as the excitation photon.

The Raman spectrum consists of higher wavelength (lower frequency) emissions or Stokes bands, appreciably more intense than the corresponding anti-Stokes bands.

Raman spectroscopy is particularly useful in the investigation of graphene-based materials because it makes possible to acquire information regarding the type of disorder, edge and grain boundaries, thickness, doping, strain and thermal conductivity of the structure under analysis [100] [101].

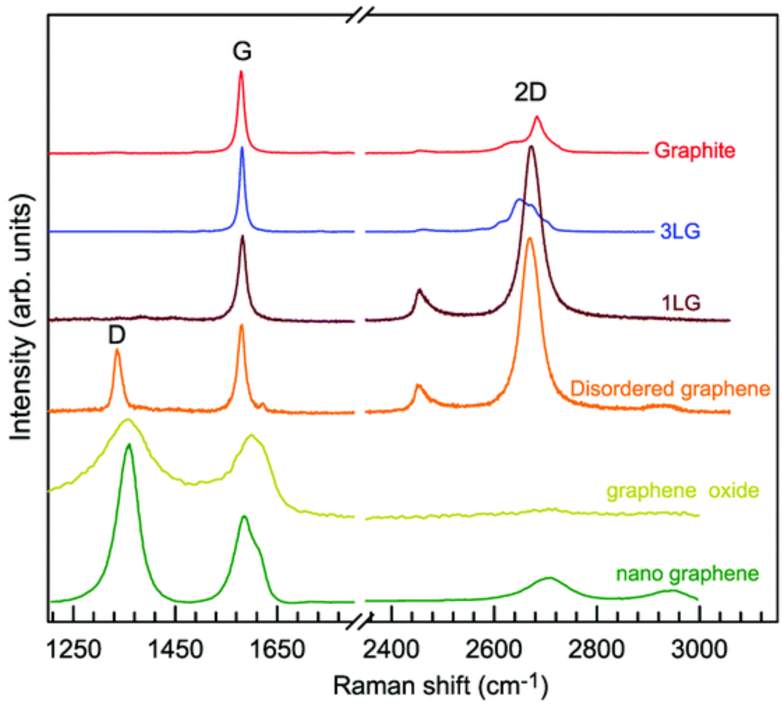

Figure 3.9: Raman spectra of graphene-based materials: graphite, 1LG, 3LG, disordered graphene, graphene oxide and nanographene. Reproduced from [102].

Figure 3.9 shows the recorded Raman spectrum of graphite, multilayer graphene (3LG), monolayer graphene (1LG), disordered graphene, graphene oxide and nanographene. The spectra exhibit three main characteristic features:

- the G band, centred around 1580 cm^{-1}, associated with a primary in plane vibration mode;
- the G′ or 2D band, centred around 2700 cm^{-1}, is attributed to a second order two phonon mode;

- the D band, centered around 1360 cm^{-1}, not visible in pristine graphene because of crystal symmetry [101], is instead visible when the honeycomb structure is interrupted by defects, and it arise from out-of-plane vibrations of sp^2-hybridized carbon atoms [103];

Figure 3.10 present the graphical representation of examples of phonon scattering process responsible for the graphene-based materials Raman peaks.

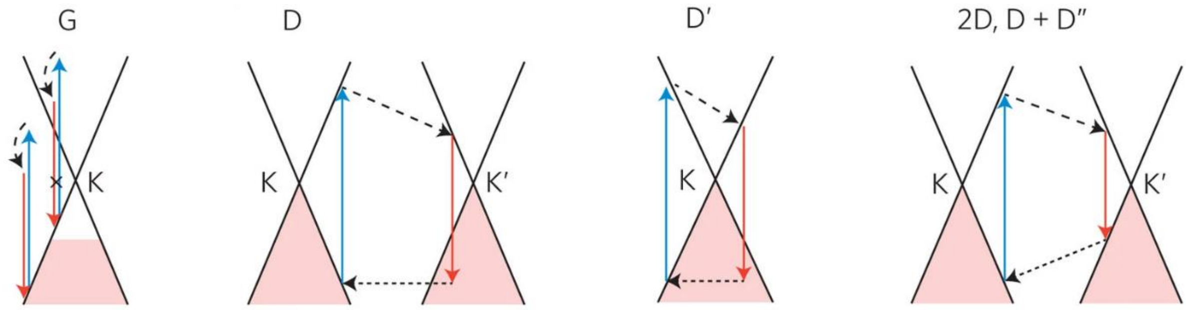

Figure 3.10: Graphical representation of examples of phonon scattering process responsible for the graphene-based materials Raman peaks. Extracted from [104].

Raman measurements were carried out at room temperature with a LabRAM HR800 Raman spectrometer (Horiba Jobin-Yvon) equipped with an external air-cooled argon ion laser operating at 514 nm (543R-AP-A01, Melles Griot) and an 800-mm focal length spectrograph. 10X (NA 0.25), 50X (NA 0.7), and 100X (NA 0.9) objectives (laser spot size ≈ 1 μm^2) were available. Wavelength calibration was performed on a standard silicon wafer by checking the zero-order peak position (0 cm^{-1}) and the Si band position (520.7 cm^{-1}).

For each sample, 12 points were taken in order to obtain a wide data set to be analysed statistically. The total acquisition time was set at 7 minutes and 28 seconds per spectrum to optimize signal-to-noise ratio. Raman-scattered light was analysed using a 2400 g/mm diffraction grating and an air-cooled CCD detector (1024X256 pixels, 26 μm). The laser excitation power was kept at 1% or 10% of the total power to avoid laser-induced annealing.

3.3.3. X-ray Photoelectron Spectroscopy

X-ray photoelectron spectroscopy (XPS) is a reliable technique that provide information regarding the elemental composition and the nature of the chemical bonds of the surface of a sample. It consists in irradiating the specimen with an X-ray beam, resulting in the ejection of core shell electrons, the kinetic energies of which are analysed by a detector and plotted against the relative number of electrons recorded. From the position of the peaks, it is possible to determine the elements and the shells from which the electrons have been ejected and the bonds the atom partake in [105]. A schematic representation of the basic components of an XPS system is reported in Figure 3.11.

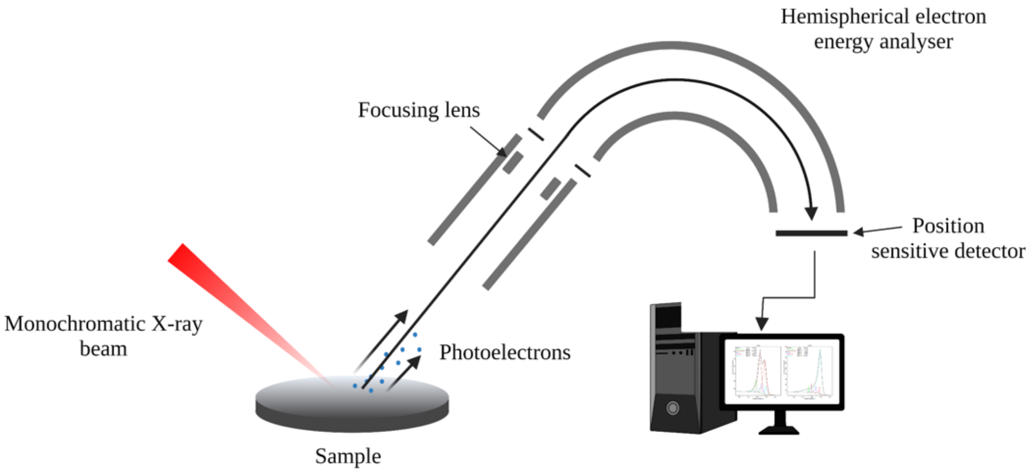

Figure 3.11: Schematic representation of the basic components of an XPS system.

In this work, XPS analysis have been conducted on graphene oxide samples to assess the degree of reduction and the healing effect of ethanol and benzene by calculating the carbon to oxygen ratio and the intensity of the peaks corresponding to carbon functional groups. Figure 3.12 shows an example of XPS specta of the C1s peak of graphene oxide and reduced graphene oxide.

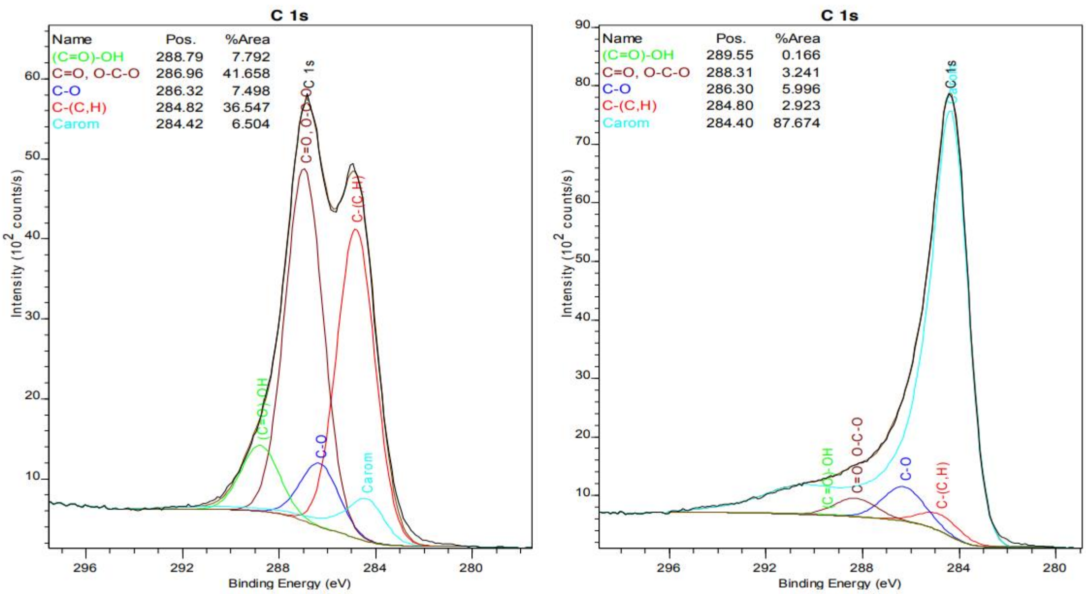

Figure 3.12: XPS spectra of the C1s peak of the GO (left) and rGO(right) [106].

XPS measurements were performed with a PHI 5000 VersaProbe III Photoelectron Spectrometer (Physical Electronics (USA)), equipped with a monochromatized micro focused Al Kα X-ray source, powered at 50 W. The pressure in the analysis chamber was kept around 10^{-6} Pa. The angle between the surface normal and the axis of the analyser lens was 45°. High-resolution scans of the C1s and O1s photoelectron peaks were recorded from a spot diameter of 200 μm using pass energy of 13 eV and step size of 0.1 eV. Charge stabilization was achieved thanks combination of Argon and electron guns. Data treatment was achieved using the CasaXPS software (Casa Software Ltd, UK).

3.3.4. X-Ray Diffraction

X-ray diffraction (XRD), or X-ray powder diffraction, is a non-destructive analytical technique widely used to assess the crystal structure, crystallite size and strain of solid samples. It is a technique based on the detection and processing of the diffracted X-rays collimated on the surface of the sample to be characterized. A signal is registered only when the incident rays interact constructively with the crystal planes, satisfying the Bragg's Law (Equation (3.2)):

$$n\lambda = 2\, d_{hkl}\, sin\theta \qquad (3.2)$$

where n is an integer, λ is the wavelength of the incident X-ray beam, d_{hkl} is the interplanar spacing and θ is the incident angle. Hence, knowing the diffraction angle and the wavelength of the incident X-ray beam, one can convert the recorded distribution of intensities into the electronic density map of the material under analysis.

In this work, lead sulphide powders have been analysed by XRD. The XRD spectrometer was operated at 30 mA, using Cu Kα radiation with a wavelength of 1.5406 Å. Data were acquired between 6° and 80° and collected with a step interval equal to 0.00831° over 2θ, with a scan speed of 0.1 sec/step.

The powder XRD patterns were then compared with a standard XRD pattern for cubic PbS, the data of which were obtained from [107] and analysed in Mercury. Y. Noda *et al.* report that the reference XRD patter, shown in Figure 3.13, was acquired at 200K and shows a lattice constant, *a*, equal to 5.9237 Å.

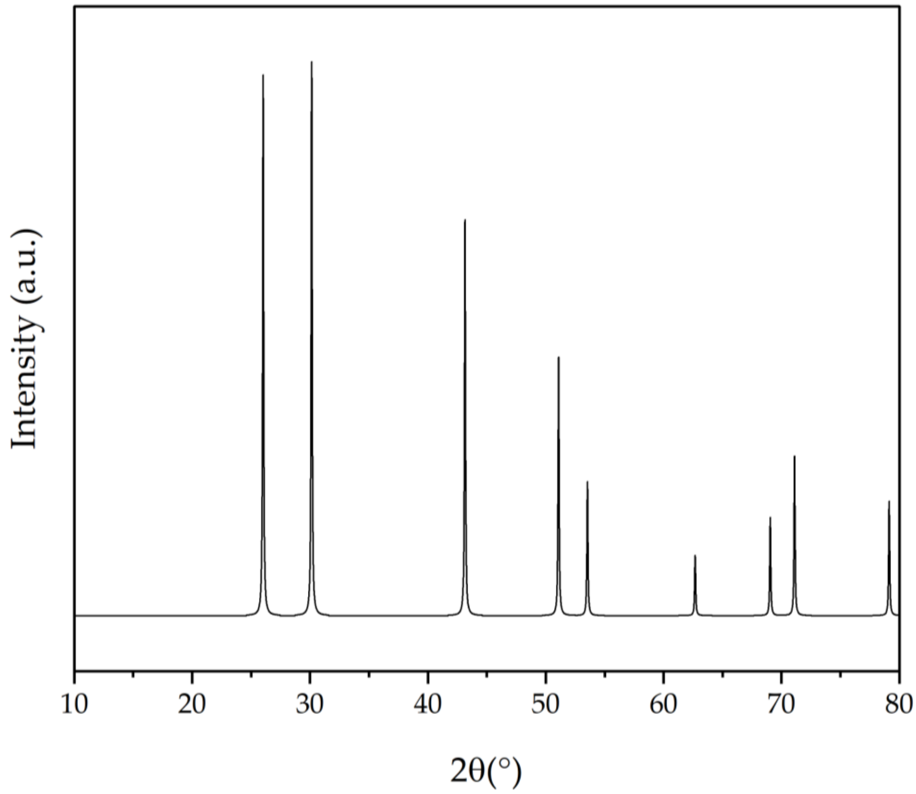

Figure 3.13: Standard XRD pattern for cubic PbS NPs. Data extracted from [107].

Lead sulphide's XRD pattern displays nine characteristic diffraction peaks located at 26.03°, 30.15°, 43.16°, 51.10°, 53.55°, 62.68°, 69.06°, 71.12° and 79.14°. The diffraction peaks are matching with crystal planes (111), (200), (220), (311), (222), (400), (331), (420) and (422) of the PbS NPs.

The Debye-Scherrer equation, here reported in Equation (3.3), was employed to estimate the crystallite size from X-ray diffraction peaks:

$$D_{hkl} = \frac{K\lambda}{B_{hkl}\, cos\, \vartheta} \tag{3.3}$$

where D_{hkl} is the crystallite size, hkl are the Miller indices of the planes being analysed, λ is the X-ray wavelength, B_{hkl} is the width (full-width at half-maximum) of the X-ray diffraction peak in radians, θ is the Bragg angle in radians and K is a constant, usually referred to as the crystallite-shape factor, which can take a value between 0.89 and 0.94. For crystallites with a cubic structure, K can be considered equal to 0.9 [108].

To be noted that Debye-Scherrer equation returns a value that can be considered the lower bound to the estimation of the nanoparticles size because there are a variety of factors can contribute to the width of a diffraction peak like inhomogeneous strain and crystal lattice imperfections [109].

3.3.5. X-Ray Fluorescence

X-ray fluorescence (XRF) is a characterization technique widely used for elemental analysis. The working principle is based on the ejection of inner shell electrons by high energy photons (X-rays or gamma-rays). Outer shell electrons consequently assume the lower energy configuration by decaying into the vacancies, emitting photons with energy equal to the energy difference between the initial and final states; examples of electronic transitions involved in the emission of X-rays are depicted in Figure 3.14. Moseley's law states that a specific pattern of emitted X-rays can be correlated to a specific element, hence allowing the determination of the composition of the sample, both in qualitative and quantitative terms [110].

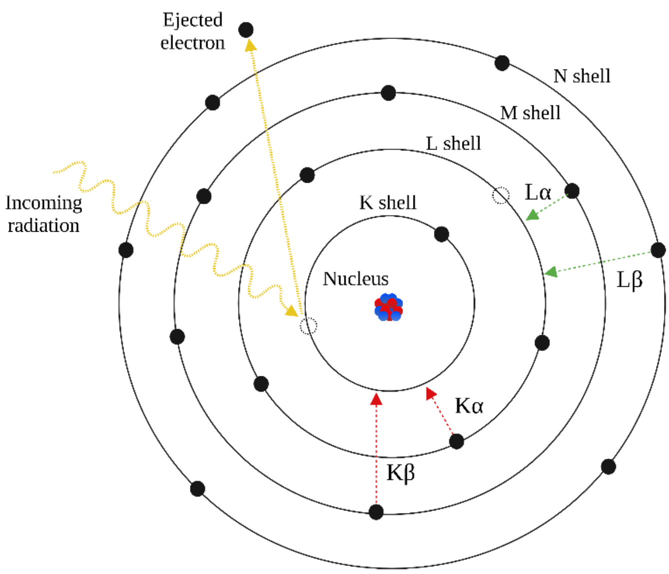

Figure 3.14: examples of electronic transitions involved in the emission of X-rays.

Dried lead sulphide powders have been analysed in a SPECTRO XEPOS energy dispersive X-ray fluorescence (ED-XRF) spectrometer, provided with a palladium and cobalt anode in the X-ray tube, to evaluate the ratio between lead and sulfur (1 was the target ratio, corresponding to the molar ratio between lead and sulfur in the asymmetric PbS unit). The XRF spectrometer detector was kept at -30°C. Data were acquired between 0 keV and 70 keV. It should be noted that organic traces are difficult to be identified through X-ray fluorescence spectroscopy.

3.3.6. Resistivity Measurements

Resistance measurements and IV curves were acquired using a Fluke 117 true RMS manual multimeter (measurable resistance range 0,1 Ω - 40 MΩ) connected to a microwave prober with 3'' chuck and four positioners and a low signal probe station equipped with a Keysight B1500A semiconductor device analyser. The latter system allowed the evaluation of the initial resistance of the graphene oxide flakes, too high to be detected by the former equipment.

3.3.7. Gas sensing measurements

Preliminary resistance variation measurements of the rGO-PbS based sensors were performed to test their gas sensing properties. The measurement set-up included: three standard gas cylinders - O2, N2 and N2/CH4 (2%) -, mass flow controllers (MFC), a humidifier (Cellkraft, P-10), a sealed chamber and a data acquisition system. The output electrical resistance of the sensor was monitored by a DMM7510 7 ½ Digit Graphical Sampling Multimeter (Keithley). Figure 3.15 shows a schematic representation of the laboratory gas sensor measurements set-up.

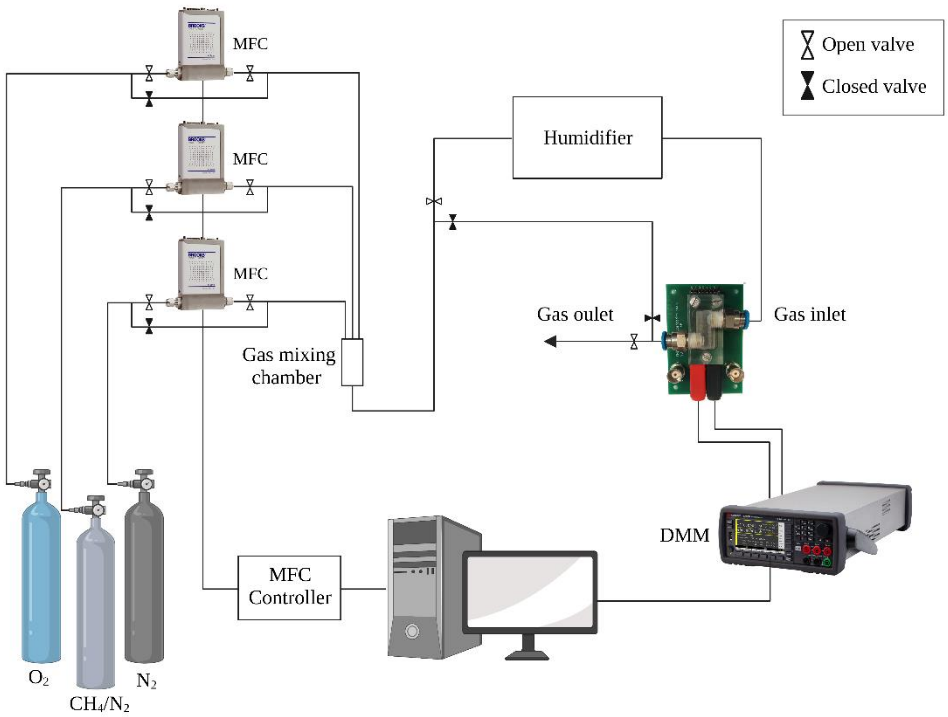

Figure 3.15: schematic representation of laboratory gas sensor measurements set-up.

The tests were conducted at room temperature (25°C), atmospheric pressure (1 atm) and 43% relative humidity. The following routine was repeated for the testing of each sensor:

- 420 sccm O_2 + 1580 sccm N_2 for the first 2 hours, to stabilize the initial resistance;
- 420 sccm O_2 + 1580 sccm N_2/CH_4 for 30 minutes, to allow sufficient exposure to the test gases;
- 420 sccm O_2 + 1580 sccm N_2 for 1 hours, to allow a full recovery.

4 Results and discussion

In this chapter the results of the analysis conducted on graphene oxide, reduced graphene oxide and lead sulphide nanoparticles will be presented. In the first section the findings about graphene oxide's morphology and sonication experiments results are reported. Once the size, texture and distribution has been optimized, the chosen graphene oxide source has been deposited on CMOSEnvi™ dies for healing treatment, thermal and chemical reduction experiments to be performed. Deconvoluted XPS and Raman spectra are reported in this section and examined for the evaluation of the reduction efficiency. Data obtained from resistance measurements carried out on reduced graphene oxide samples are finally described. The second section is dedicated to the discussion of the results of the analysis conducted on lead sulphide nanoparticles. XRF spectroscopy measurements and XRD patterns are examined in detail in this section and size and distribution of PbS nanoparticles are investigated by SEM imaging. Lastly, the results of the decoration of the rGO flakes with lead sulphide nanocrystals are presented, as well as the preliminary results about the gas sensing performance of the rGO-PbS NPs devices.

4.1. Graphene oxide

4.1.1. Morphological characterization

The morphology of the three commercially available graphene oxide was investigated through SEM imaging. SEM micrographs of the drop casted GO dispersions, reported in Figure 4.1, show that the GOs supplied by Graphenea, Sigma-Aldrich and Angstron Materials (US) present very different morphologies both before and after ultrasonication treatment.

The analysis of the former (Figure 4.1, (a)) revealed the presence of wrinkled multilayers graphene oxide flakes, with size ranging between 2 and 20 μm, consistent with what reported by the supplier. After 15 minutes of ultrasonication (details reported in Section 3.2.2), one can observe the reduction of the dimension of the biggest GO flakes; by increasing the sonication time up to 60 minutes, it is possible to yield a GO dispersion with an abundance of flat flakes with lateral size between 1 and 2 μm and smaller than ~ 0.5 μm (bimodal distribution) (Figure 4.1, (b)), suitable for the formation of a network on the surface of the interdigitated electrodes, which acts as a conductive path for charge carriers [25]. In literature it is reported that the exfoliation by ultrasonication of graphene oxide flakes is promoted by inertial cavitation, described as *a sonication regime with short lived cavitation bubbles that undergo violent and chaotic collapse* [111]. This mechanism seems to preferentially exfoliate flakes with size larger than ~ 0.5 μm, whereas smaller flakes fragmentation is less frequent.

SEM images of Sigma-Aldrich's graphene oxide (Figure 4.1, (b)-(c)) shows a completely different morphology: according to ISO standard on graphene and related two-dimensional (2D) materials nomenclature [112], it is possible to define the clusters recognizable in Figure 4.1 (c) as nano graphite oxide rather than multilayer graphene oxide. Moreover, the size and distribution of the nano platelets is not highly influenced by the ultrasonication procedure, probably because of the high adhesion forces between the flakes.

Finally, graphene oxide supplied by Angstron Materials is characterized by an accordion-like structure, as clearly shown in Figure 4.1 (e)-(f), in accordance with what reported in literature [113]. The ultrasonication treatment seems to have a limited effect on the morphology of the GO: after being treated in a sonication bath for four hours, the GO agglomerate was only partially exfoliated.

The impossibility to control the morphological characteristics of the Sigma-Aldrich's and Angstron Materials' graphene oxide made them inadequate for the production of the final devices but still useful for studies regarding the efficiency of the healing and thermal reduction procedure.

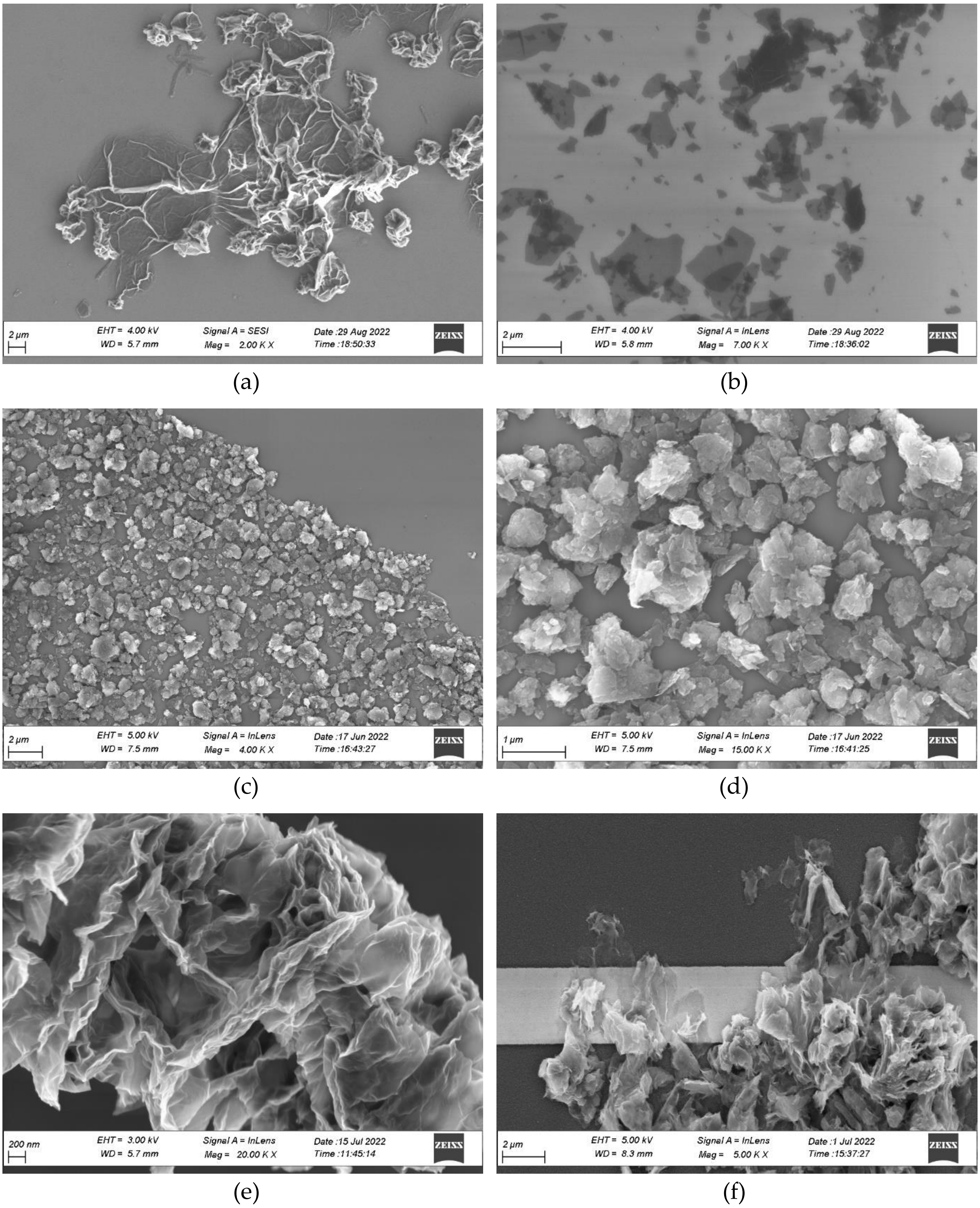

Figure 4.1: SEM images of graphene oxides provided by three different suppliers. (a)-(b) Graphenea's GO before and after 60 minutes ultrasonic bath. (c)-(d) Sigma-Aldrich's GO before and after 60 minutes ultrasonic bath. (e)-(f) Angstron Materials' GO before and after 240 minutes ultrasonic bath.

4.1.2. Thermal annealing

To investigate the efficiency of thermal annealing procedure described in Section 3.2.4, Raman spectra were acquired for each of the three graphene oxide samples considered in this work. The average Raman curves, obtained before and after the thermal treatment, are reported in Figure 4.2. Curve fitting for the Raman data were carried out in OriginPro 2022 software, fitting each peak with an appropriate number of Lorentzian curves, widely employed in the analysis of Raman spectra of graphene-based material, using the software fitting functions and the automatic parameter initialization. All the fits show good agreement with the experimental data, as underlined by the high value of reduced χ^2, greater than 0.99 for every fitting. It should be noted that, although data have been acquired for each supplied graphene oxide, the results of the analysis conducted on different GOs are not to be compared, since the interpretation of the deconvoluted spectra is dependent on the morphology of the sample [111].

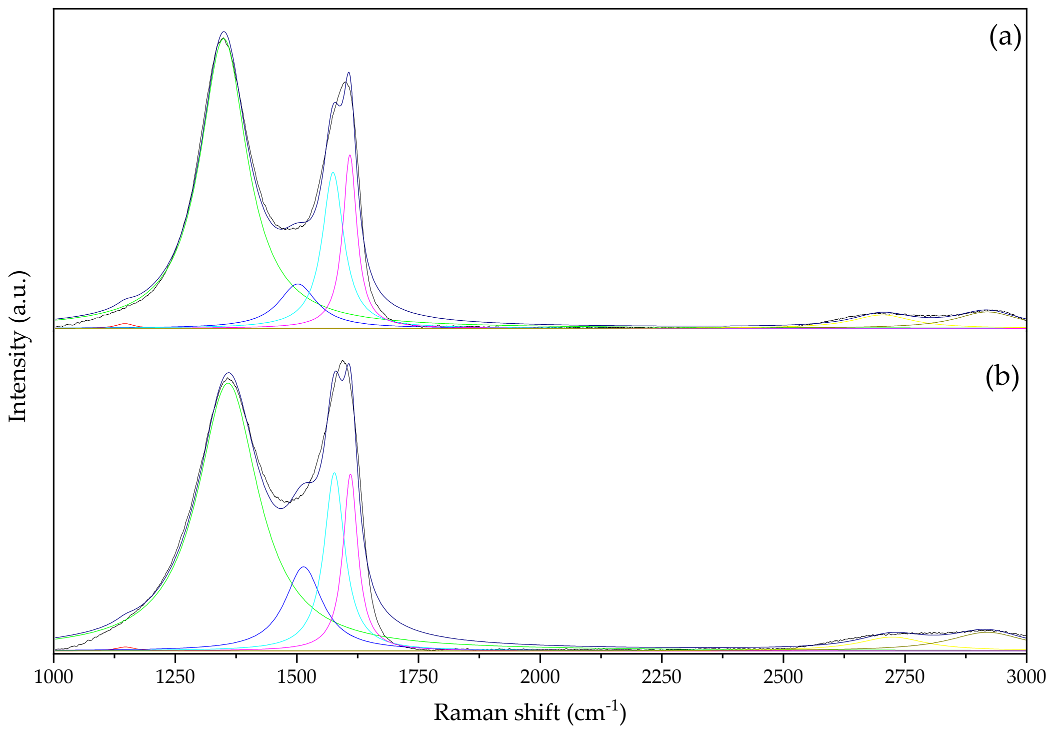

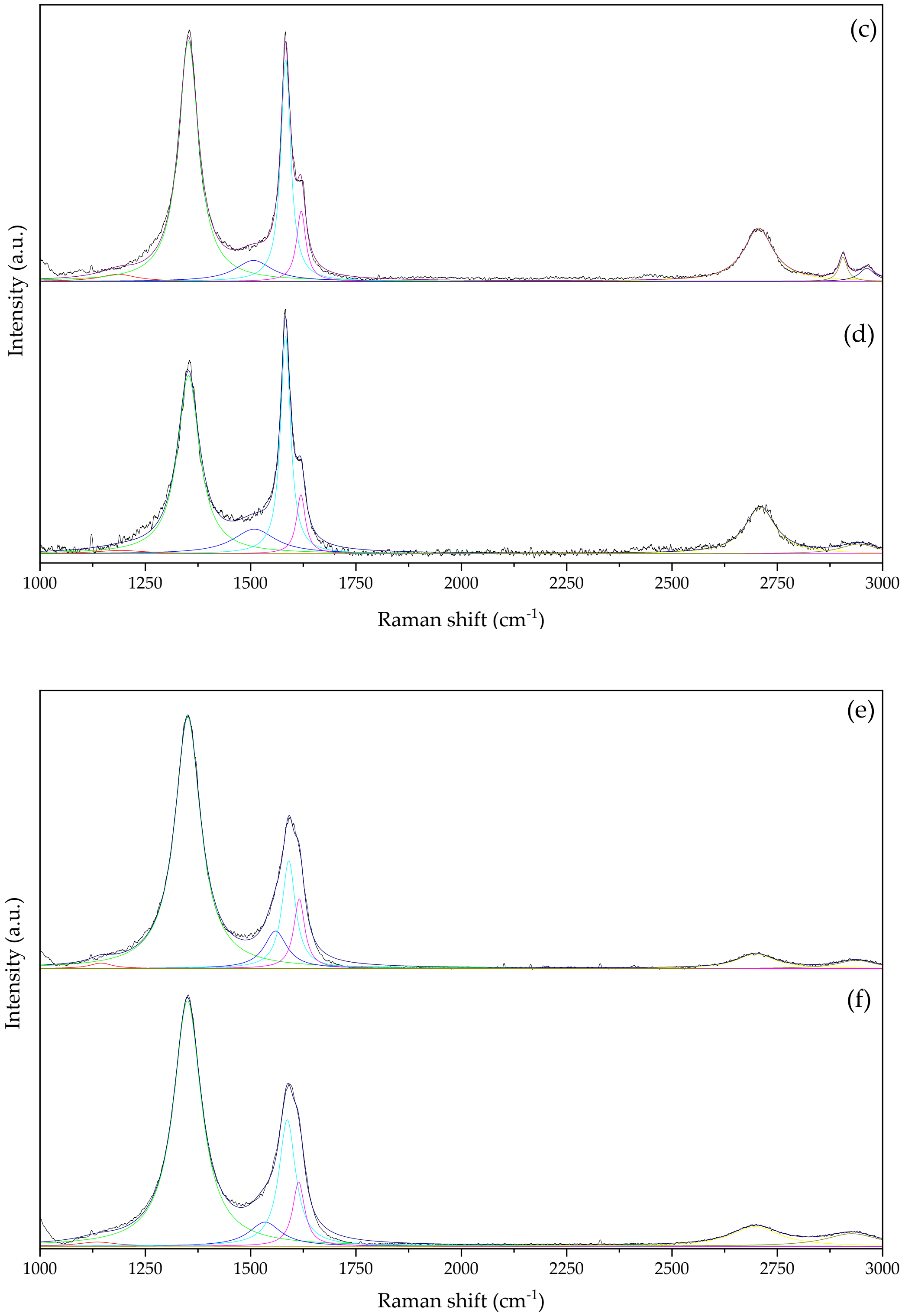

Figure 4.2: Raman spectra of the three graphene oxide sample considered: (a)-(b) Graphenea's GO before and after thermal annealing; (c)-(d) Sigma-Aldrich's GO before and after thermal annealing; (e)-(f) Angstron Materials' GO before and after thermal annealing.

The most significant features of the graphene oxide's Raman spectrum are located in the range between 1000 cm^{-1} and 2000 cm^{-1}, where, according to some authors, the experimental profile can be fitted with five Lorenzian curves, representing the first-order Raman modes, namely D*, D, D'', G and D' [114, 115, 116, 117, 118]. An example of deconvolution of the Raman spectrum of Angstron Materials' GO is represented in Figure 4.3.

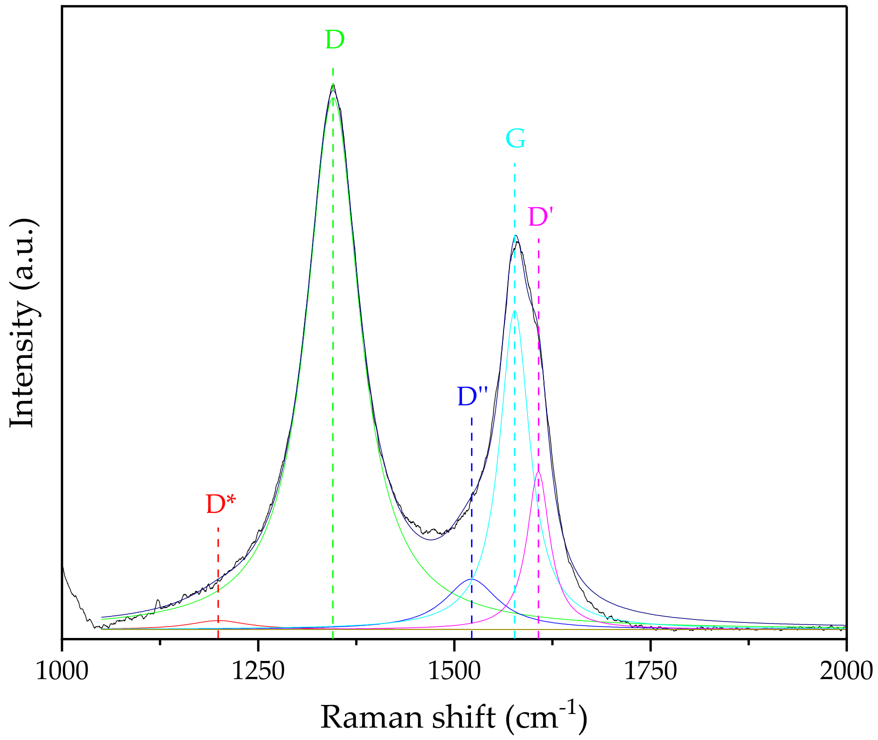

Figure 4.3: Deconvolution of the Raman spectrum of Angstron Materials' GO.

G peak, corresponding to the first order allowed Raman mode E_{2g}, and the D peak, associated with the A_{1g} breathing mode [115], are easily located, centered around 1350 cm^{-1} and 1580 cm^{-1}, respectively. A broad shoulder can be recognized between these two peaks, which can be interpreted as a new band, D''. The origin of D'' is controversial [119, 120, 121], but most authors attributed it to the presence of an amorphous phase, since this peak decreases in intensity as crystallinity increases [114]. D*, which fits the small peak centered between 1150 cm^{-1} and 1200 cm^{-1}, is usually associated to the disordered graphitic lattice caused by a sp^3 rich phase [115]. A final defect-activated mode, D', can be located at ~1610 cm^{-1}.

Traditionally, the degree of graphitization of carbon-based materials is estimated by evaluating the ratio between the relative intensity of the D band and the G band, which provides a good indication of the number of defects. However, knowing that in graphene oxide's Raman spectrum the G band is given by the superposition of the G, D'' and D* peak, it is more significant to evaluate the ratio between the intensity of the G and D peak after the fitting procedure with five Lorentzian curves. Table 4.1 reports the value of the I_D/I_G ratio before and after the thermal annealing for the three graphene oxide samples.

Table 4.1: I_D/I_G ratio before and after the thermal annealing.

Sample		I_D/I_G ratio
Graphenea's GO	Reference	1.79459 ± 0.06064
	Annealed	1.49197 ± 0.02617
Sigma-Aldrich's GO	Reference	0.97652 ± 0.09765
	Annealed	0.90826 ± 0.08
Angstron Materials' GO	Reference	2.13183 ± 0.11001
	Annealed	1.9846 ± 0.18

From the analysis of the I_D/I_G ratio, it can be inferred that during the annealing process oxygen moieties are partially removed with the simultaneous recovery of the graphitic plane structure. This hypothesis is corroborated by the sharp decrease in resistance observed during the heating of the samples. The plots of the resistance and temperature variation during the thermal annealing experiment are reported in Figure 4.4. The initial strongly insulating behavior of the samples can be attributed to the small size of the sp^2 domain, which grows as the temperature is increased from 80°C to ~ 325-330°C, resulting in an enhanced electrical conductivity. Recent studies [44] have demonstrated that significant crystallographic changes occur on GO paper at a temperature between 200°C and 250°C, to which is associated a systematic drop in resistance.

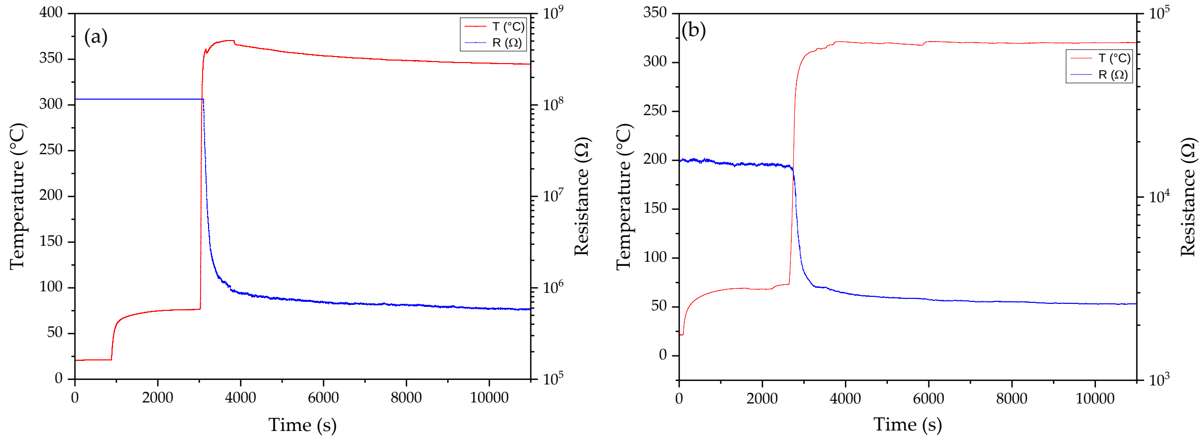

Figure 4.4: Resistance and temperature variation during the thermal annealing experiments of (a) Sigma-Aldrich's GO and (b) Angstron Materials' GO.

The limited two-wire resistance measurements range (100 Ω - 100 MΩ) of the DMM (Keithley, 2110 5½ Digit Multimeter) placed in the vacuum chamber station, illustrated in Section 3.2.4, allowed the acquisition of the resistance data only for Sigma-Aldrich's and Angstron Materials' GO samples. This implies that it was not possible to significantly recover the conductivity of the Graphenea's GO samples through thermal annealing.

This conclusion is justified by the results of the XPS characterization of the untreated GO powders. XPS spectra are represented in Figure 4.6 and the relevant data are reported in Table 4.2. Each C1s XPS spectrum has been deconvoluted into five Gaussians, as shown in Figure 4.5 : the first band centered around 282.9 eV can be interpreted as the superposition of two peaks, one associated to sp^2 hybridized carbon (282.4 eV) and the other with sp^3 hybridized carbon (282.9 eV); the binding energy at 284.8 eV, 285.9 eV and 286.9 eV, instead, have been linked to O=C-O, C=O and C-O functional groups, respectively.

The prominent peak associated to C-O function group in Graphenea's GO spectrum (Figure 4.6 (c)) suggest that the latter is characterized by a more oxidized structure compared to the other two GO powders. This observation is further proven by the evaluation of the sp^2/sp^3 ratio, calculated as the ratio between the areas of the peak located at 282.4 eV and 282.9 eV: Graphenea's powders present a very low degree of graphitization, making the process to restore ordered graphene-like 2D structure more difficult.

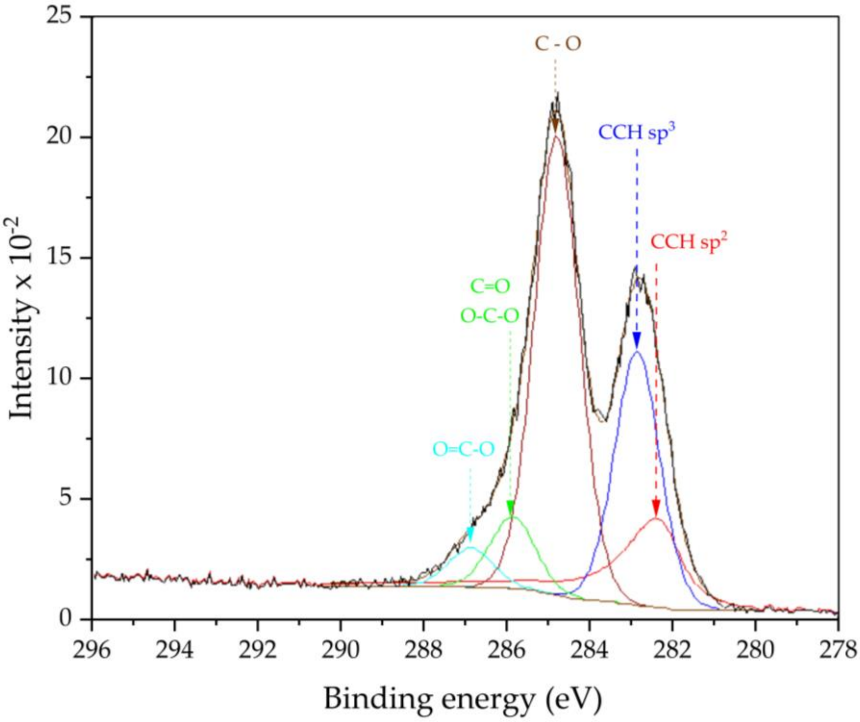

Figure 4.5: Deconvolution of the XPS spectrum of Graphenea's GO.

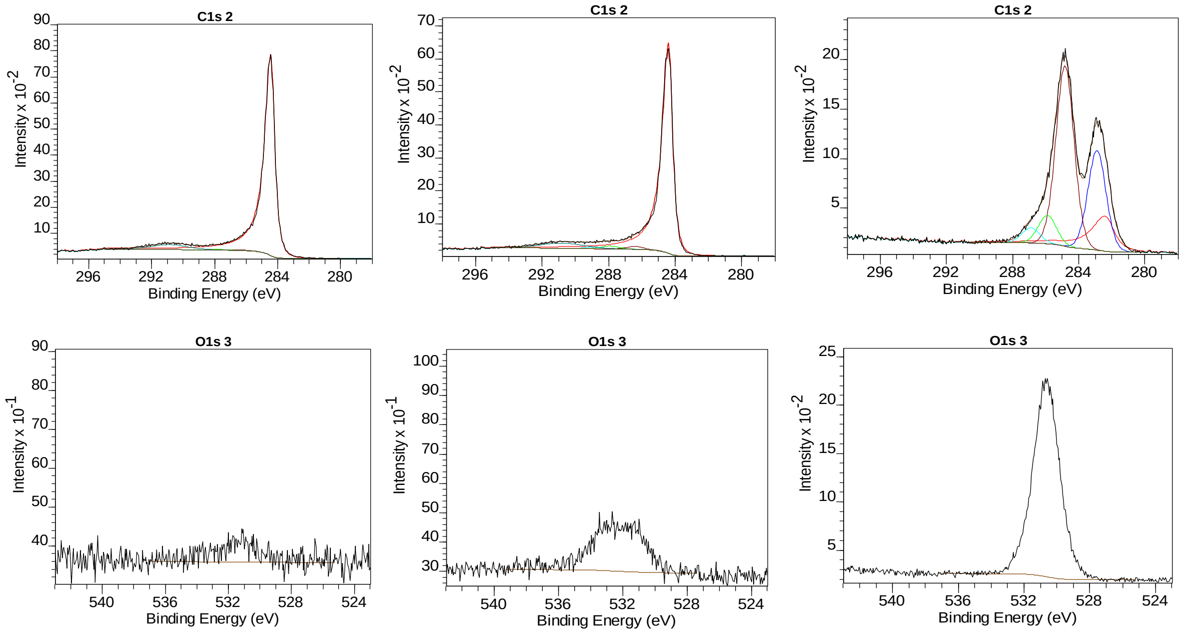

(a) (b) (c)

Figure 4.6: XPS curves of untreated (a) Angstron Materials' GO powders, (b) Sigma-Aldrich's GO powders and (c) Graphenea's GO powders.

Table 4.2: sp^2/sp^3 ratio and O/C ratio of untreated Graphenea's GO powders, Sigma-Aldrich's GO powders and Angstron Materials' GO powders.

Untreated samples	sp^2/sp^3 ratio	O/C
Graphenea's GO	0.65	0.476
Sigma-Aldrich's GO	9.00	0.052
Angstron Materials' GO	15.84	0.013

Finally, XPS data have been acquired for the three graphene oxide samples before and after thermal annealing procedures. The results regarding the improvement of the degree of graphitization are reported in Table 4.3. They seem to suggest a significant increase in the relative amount of sp^2 domains but the initial sp^2/sp^3 ratio of the drop casted specimens, which is not in good agreement with what previously reported in Table 4.2 for the GO powders, raises some concerns about the validity of the results.

This discrepancy could be related to some imperfect calibration during spectra analysis, caused by incorrect identification of the contribution around 99.5 eV, region of the spectra to be associated with Si2p (contribution of the substrate). Another limit of the XPS analysis of drop casted GO was the identification of the data referring to the actual material of interest: indeed, even if the spot size of the XPS X-ray beam was relatively small, the non-homogeneous distribution of the flakes on the drop casted area, caused by a strong coffee ring effect during drop casting (Table 4.6), made the process of GO detection very challenging. Therefore, many datapoints actually refer to the substrate contaminated by carbon residues and not to the drop casted GO. The process of recognition and elimination of the unreliable data substantially reduced the data poll to get a relevant statistical analysis of the effect of the thermal annealing on GO. This problem was not encountered during the XPS analysis of the GO original powders thanks to the higher homogeneity and thickness of the substrate and the absence of the contribution of silicon oxide.

Table 4.3: sp^2/sp^3 ratio and O/C ratio for the three graphene samples before and after thermal annealing.

Sample	sp^2/sp^3 ratio before thermal annealing	sp^2/sp^3 ratio after thermal annealing
Graphenea's GO	0	2.11
Sigma-Aldrich's GO	0.14	2.07
Angstron Materials' GO	1.41	1.44

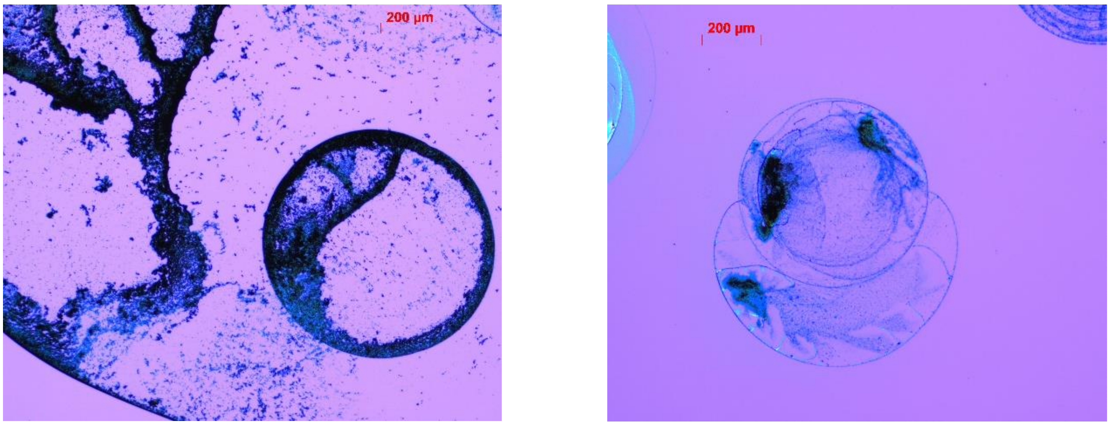

Figure 4.7: Optical image of the drop casted GO on silicon/silicon oxide substrate.

In conclusion, in this paragraph the findings of the analysis conducted on the GO samples have been outlined. The results suggest that the thermal annealing process alone is not sufficient to remove the majority of the oxygen moieties from Graphenea's graphene oxide flakes, making the process unsuitable for obtaining a conductive material.

4.1.3. Healing treatment

To evaluate the effectiveness of the GO healing treatment with ethanol and benzene, Raman spectra and XPS data were acquired. The average values of the ratio between I_D/I_G of the treated and untreated samples are represented with their respective error in Figure 4.8. The deconvolution of each Raman spectra has been carried out with the same procedure illustrated in the previous paragraph, extracting the intensity of the D and G peaks after the fitting procedure with five Lorentzian curves. It can be easily understood that, in this work, it was not possible to establish a trend regarding the improvement of the degree of graphitization in presence of a carbon source from Raman analysis.

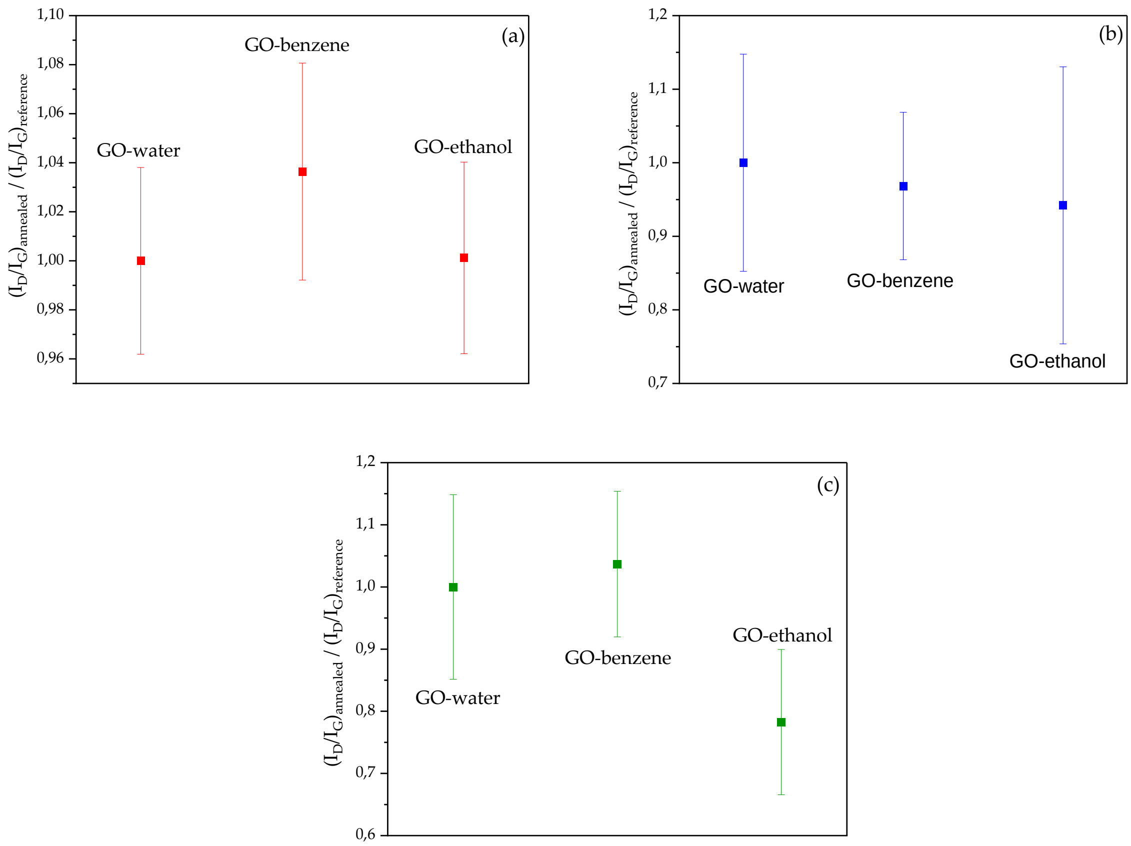

Figure 4.8: Graphical representation of the I_D/I_G ratio after the healing treatment.

A similar conclusion can be reached by observing the XPS results (Table 4.4) of the healing experiments conducted on Graphenea's GO and Angstron Materials' GO, for which the same difficulties underlined in the previous paragraph have been encountered. Even if the results indicate an increase in the oxygen content after the healing treatment with ethanol, suggesting that ethanol molecules have been absorbed on the surface of graphene oxide flakes, the limited number of reliable data does not allow to confirm that the ethanol healing treatment was successful. The results regarding benzene, are again uncertain, given the opposite tendencies of the O/C ratio before and after the healing treatment in Graphenea's GO and Angstron Materials' GO.

Table 4.4: sp^2/sp^3 ratio and O/C ratio before and after the healing treatment.

Sample		sp^2/sp^3 ratio before and after healing treatment	O/C before and after healing treatment
Graphenea's GO	Reference	0/2.11	0.41/0.21
	Benzene	0.064/2.69	0.42/0.21
	Ethanol	0.21/2.64	0.29/0.34
Angstron Materials' GO	Reference	1.41/1.44	0.14/0.36
	Benzene	0.26/2.48	0.36/0.10
	Ethanol	0.28/1.20	0.15/0.21

Therefore, the analysis on the efficiency of the healing treatment is generally inconclusive. However, the promising results reported in literature about the ability of ethanol to repair GO defect sites in conditions similar to those employed in this work [56], support the hypothesis that the employment of other characterization techniques such as FTIR measurements and XRD measurements could prove the effectiveness of ethanol in healing GO flakes.

4.1.4. Solvothermal annealing and chemical reduction

Given the unsuccessful attempt in reducing Graphenea's GO via thermal annealing, this material was subjected to chemical reduction with L-ascorbic acid at high temperatures (details reported in Section 3.2.5). The results of the Raman, XPS and electrical measurements are here described.

Raman spectra, acquired for the six different samples, were analysed with the same procedure delineated in paragraph 4.1.2. The I_D/I_G ratio, reported Table 4.5 and Figure 4.9, follows a well-defined trend: as the temperature of the reducing medium (Milli Q water or NMP) increases, the reduction process becomes more efficient. It is particularly interesting to observe that the effect of temperature alone allows for a high degree of reduction of the GO in NMP, leading to a significant decrease in resistivity of the graphene oxide flakes, as deducible from the resistance values reported in Table 4.6. This result suggests a higher effectiveness of the solvothermal reduction of GO compared to the thermal annealing in the vacuum chamber, probably related to the high temperature oxygen-scavenging properties of NMP [49]. High temperatures seem to promote also the interaction of ethanol with the defective site of graphene oxide. This hypothesis, formulated on the basis of the I_D/I_G ratio values, is confirmed by the improvement in resistivity (Table 4.6) of both the GO subjected to ethanol healing at 199°C and the GO subjected to both ascorbic acid reduction and ethanol healing at 199°C, compared with the same samples not treated with ethanol.

Table 4.5: I_D/I_G ratio after chemical reduction and solvothermal annealing.

Reduction medium	Reduction temperature (°C)	I_D/I_G ratio
-	-	1 ± 0.10366
Milli-Q water - Vitamin C	80	0.87905 ± 0.03855
NMP - Vitamin C	80	0.86788 ± 0.04876
NMP	199	0.72798 ± 0.06451
NMP - Ethanol	199	0.7625 ± 0.08139
NMP - Vitamin C	199	0.6335 ± 0.06422

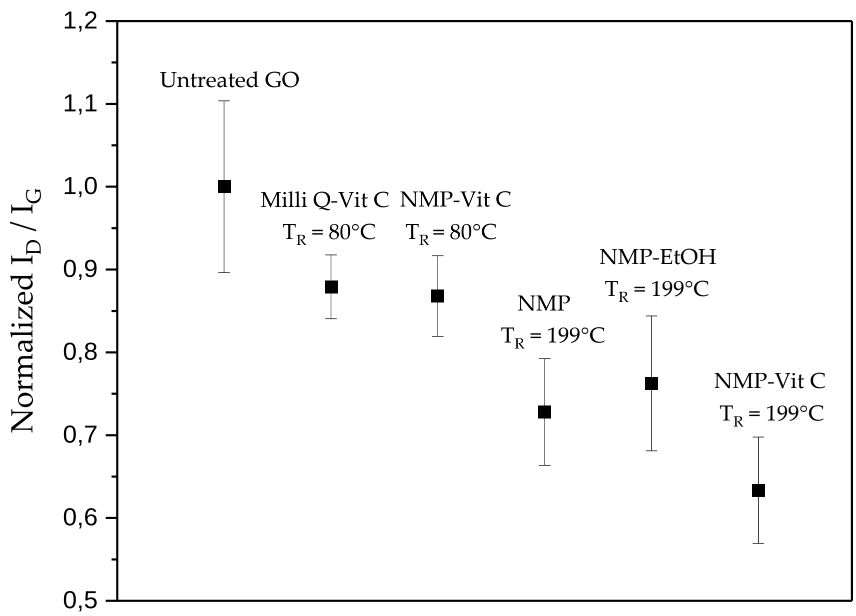

Figure 4.9: Graphical representation of the I_D/I_G ratio after chemical reduction and solvothermal annealing.

In Figure 4.10, examples of the IV curves of one graphene oxide devices, acquired at the low signal probe station PM8PS before and after reduction, are reported. A dual voltage sweep was performed between -2V and 2V with a zero-bias voltage, obtaining 402 datapoints. The compliance was set at 50 mA and the hold time at 20 ms.

The measurements were performed at the controlled temperature of 30°C and in the dark. The latter condition is important in particular for the acquisition of the IV curves before the chemical reduction, because of the very low current and high noise level.

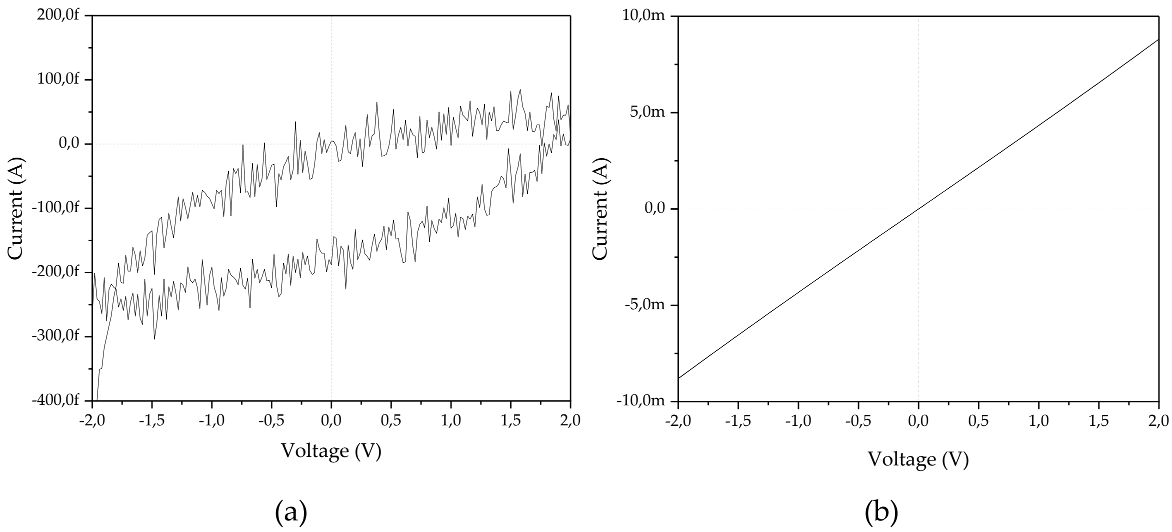

Figure 4.10: I-V characteristics of one of the devices (a) before and (b) after the reduction with ascorbic acid at 199°C.

In order to verify that the acquired signal was not to be imputed to current leakage between the fingers of the interdigitated electrodes, IV curves of untouched DIEs were acquired. No signal was detected, confirming that curve in Figure 4.10 (a) is to be ascribed to the unmodified GO. It is very clear that the unmodified material presents a non-linear behavior, with negligible conductance. The strong insulating behavior is to be attributed to the presence of a very high number of oxygenated groups on the graphene oxide flakes. After reduction, instead, a classic ohmic behaviour is obtained as expected. Resistance values, reported in Table 4.6, were extracted from each IV curve, at 1 V for the untreated GO samples (operation voltage for the final device) and by linear fitting for the reduced graphene oxide devices.

Table 4.6: Resistance values of GO flakes before and after the reduction process.

Reduction medium	T_R (°C)	Resistance before reduction (TΩ)	Resistance after reduction (Ω)
Milli-Q - Ascorbic acid	80	2.62 ± 1.65	834654.8 ± 21481.9

NMP - Ascorbic acid	80	3.68 ± 3.08	16519.1 ± 86.1
NMP	199	4.28 ± 6.08	72301.2 ± 146.8
NMP - Ethanol	199	1.74 ± 2.76	51018.8 ± 100.4
NMP - Ascorbic acid	199	4.92 ±1.28	395.0 ± 0.3
NMP - Ascorbic acid - Ethanol	199	8.34 ± 2.39	232.4 ± 3.55

A zoomed-in representation of the IV curves of the reduced samples highlights the progressive improvement of conductivity. For the sample with the highest conductivity, the resistivity decreased by 10 orders of magnitude.

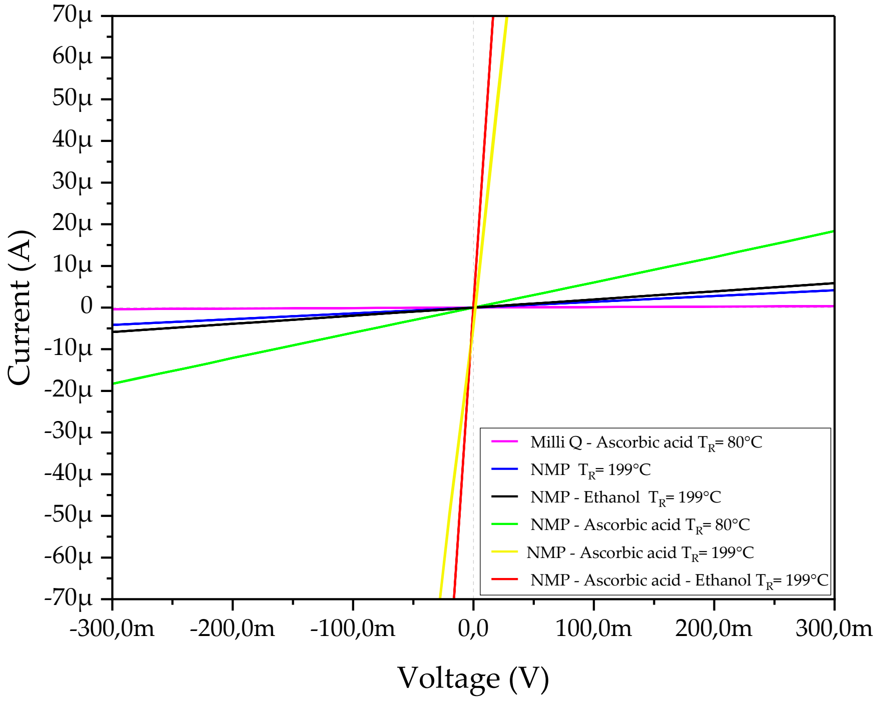

Figure 4.11: Zoomed I-V characteristics of the devices after the reduction procedure.

Furthermore, the dependence of the resistivity of reduced graphene oxide on temperature, could reveal the electronic transport mechanism of rGO. It is expected that the electronic transport in rGO is dominated by Efros-Shklovskii variable range hopping (ES-VRH) or Mott variable range hopping (M-VRH), depending on the temperature and the degree of disorder of the system, as already discussed in Section 2.1.2.1. However, in this work, this aspect was not investigated.

Finally, the results of the XPS measurements are reported in Table 4.7. The data seems to be in counter tendency with both the results of the Raman spectroscopy and electrical characterization. It is thus quite challenging to provide an interpretation of these XPS data. It can be observed that it is has been difficult to have a reliable quantitative analysis through XPS characterization, because of the quality of the samples and the difficult interpretation of the XPS spectra.

Table 4.7: sp^2/ sp^3 ratio and O/C ratio after chemical reduction and solvothermal annealing.

Reduction medium	T_R (°C)	sp^2/sp^3 ratio	C/O ratio
Untreated	-	0.65	0.47
Milli-Q - Ascorbic acid	80	100% sp^2	0.14 ± 0.008
NMP - Ascorbic acid	80	7.335 ± 3.217	0.155 ± 0.007
NMP	199	1.66 ± 0.156	0.16 ± 0.014
NMP - Ethanol	199	1.5 ± 0.028	0.165 ± 0.007
NMP - Ascorbic acid	199	3.08 ± 0.212	0.185 ± 0.007

Nevertheless, XPS measurements can be used to qualitatively assess the effectiveness of the reduction process. Figure 4.12, for instance, depicts Graphenea's GO spectra before and after chemical and solvothermal reduction at 199°C. The two peaks associated to the oxygen functional groups clearly diminish in intensity as a result of the reduction procedure, indicating that the final product was successfully deoxigenated.

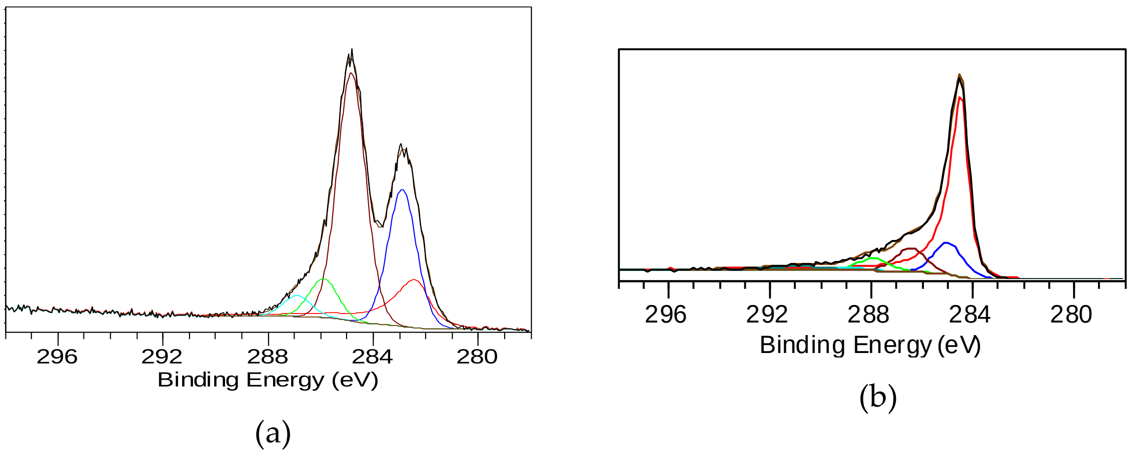

Figure 4.12: XPS spectra of Graphenea's GO samples (a) before and (b) after the reduction with ascorbic acid at 199°C.

In conclusion, chemical reduction with ascorbic acid has proved to be a feasible route for the reduction of graphene oxide. The contribution of the solvothermal annealing, possible thanks to the use of a solvent (NMP) with a high boiling point (202 °C), is important to allow a sufficient lowering of the resistance of GO. Finally, it has been proven that ethanol healing process at 199°C allows a further increase in conductivity.

4.2. Lead sulphide nanocrystals

Quantitative information about the composition of the PbS powders were gathered through XRF spectroscopy. The samples obtained from the four synthesis performed in this work are named PbS_1, PbS_2, PbS_3 and PbS_4. The results, reported in Table 4.8 and Table 4.9, reveal that only the second and last synthesis yielded a powder with a lead-to-sulphur ratio compatible with the presence of PbS nanoparticles. The high lead content of the first sample can be explained by considering that, during the synthesis, the dripping of Na_2S solution got jammed, promoting the formation of amorphous lead nanoparticles. This theory is supported by the fact that XRD pattern, represented in Figure 4.13 (a), reveals a weakly crystalline sample.

The third sample, instead, was obtained by reducing by half the volume of capping agent in the synthesis mixture (50 mL of 0.1 M 2-mercaptoethanol instead of 100 mL); it could be inferred that this adjustment caused the formation of amorphous lead nanoparticles alongside crystalline ones. The XRD pattern (Figure 4.13(b)), indeed, shows the presence of peaks associated with crystalline PbS but lacks those related to crystalline lead.

Table 4.8: XRF results for PbS_1, PbS_2, PbS_3, and PbS_4, respectively.

Element		Concentration	Abs. Error
Pb	Lead	84.45 %	0.03
		21.27 %	0.01
		79.77 %	0.02
		70.61 %	0.03
S	Sulphur	4.170 %	0.004
		2.587 %	0.003
		3.948 %	0.004
		7.775 %	0.006
Na	Sodium	0.849 %	0.066
		1.38 %	0.14
		0.691 %	0.057
		0.886 %	0.065

Al	Aluminium	0.0787	%	0.0020
		0.1921	%	0.0050
		0.0715	%	0.0018
		0.0738	%	0.0017
Cd	Cadmium	0.0539	%	0.0011
		0.00857	%	0.00029
		0.0473	%	0.0011
		0.03924	%	0.00092

Table 4.9: Pb/S molar ratio

Sample	Pb/S molar ratio
PbS_1	3.134
PbS_2	1.272
PbS_3	3.127
PbS_4	1.405

XRD patterns of PbS_2 and PbS_4 are presented in Figure 4.13 (c) and (d). The two profiles show clearly defined peaks, the broadening of which confirms the crystalline nature of the two powders.

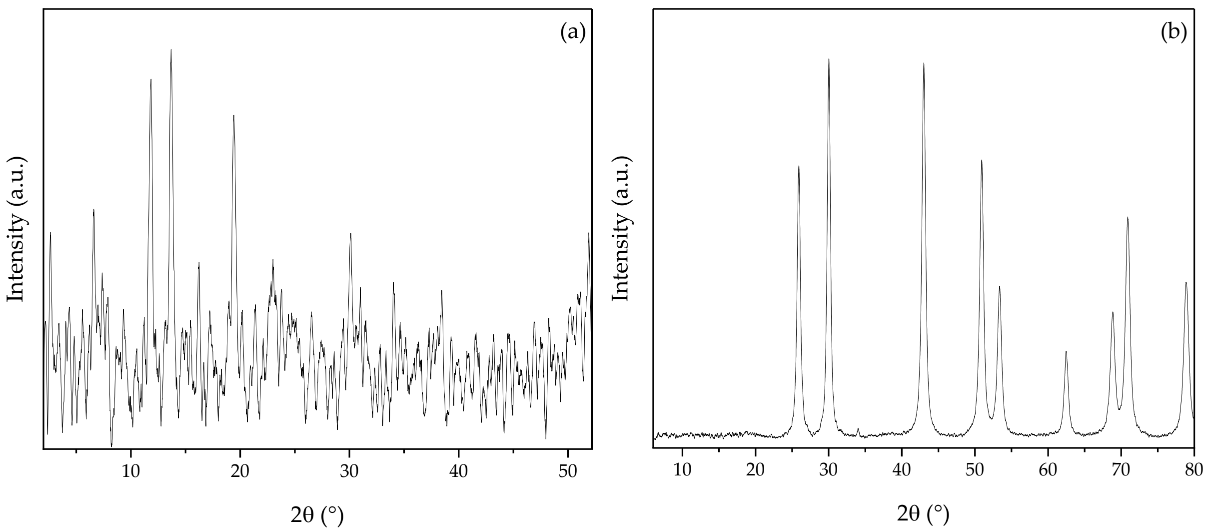

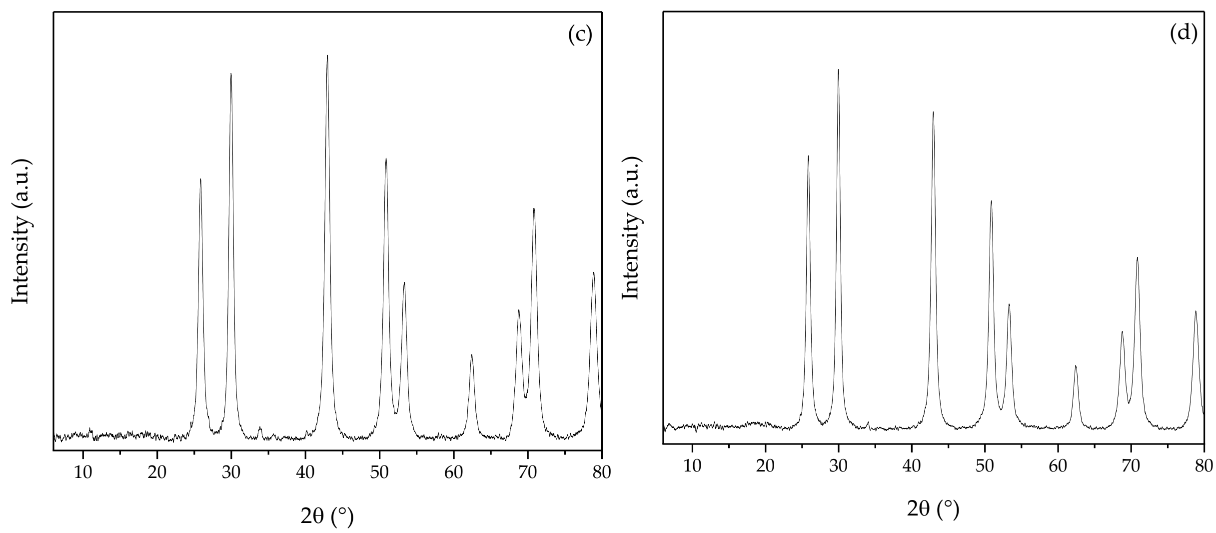

Figure 4.13: XRD pattern of (a) PbS_1 and (b) PbS_3, (c) PbS_2 and (d) PbS_4.

The diffraction pattern of PbS_2 and PbS_3 shows peaks at approximately 25.8°, 29.9°, 42.9°, 50.8°, 53.3°, 62.4°, 68.8°, 70.8° and 78.8°, corresponding to planes (111), (200), (220), (311), (222), (400), (331), (420) and (422). These data are in good agreement with what reported by Y. Noda *et al.* [107], and consistent with the cubic structure of PbS.

The analysis of the XRD patterns was carried out in OriginPro 2022, using a pseudo-Voigt function in the curve-fitting process. The pseudo-Voigt (pV) profile, widely used to analyse experimentally observed powder XRD line, is described as a linear superposition of Lorentz and Gauss curves and can be considered as a close approximation to the Voigt function [122]. The mathematical definition of the pseudo-Voigt function is reported in Equation (4.1).

$$y = y_0 + A\left[m_u \frac{2}{\pi}\frac{w}{4(x-x_C)^2 + w^2} + (1-m_u)\frac{\sqrt{4\ln 2}}{\sqrt{\pi}w} e^{-\frac{4\ln 2}{w^2}(x-x_C)^2}\right] \tag{4.1}$$

$$L = \frac{2}{\pi}\frac{w}{4(x-x_C)^2 + w^2} \tag{4.2}$$

$$G = \frac{\sqrt{4\ln 2}}{\sqrt{\pi}w} e^{-\frac{4\ln 2}{w^2}(x-x_C)^2} \tag{4.3}$$

The contribution of the Lorentzian and Gaussian (Equation (4.2) and (4.3)) is weighted by m_u, the profile shape factor, also referred to as the Lorentz fraction. Moreover, w represent the full width at half maximum, x_C the position of the maximum of the function and A the area below the curve. The R-squared values for the pseudo-Voigt function fitting of the PbS_2 and PbS_4's XRD profile is 0.997 and 0.998, indicating an almost perfect fit of the experimental data. Bragg's law, described in Equation (3.2), was employed to determine the interplanar distances d_{hkl}, from which it was possible to estimate the lattice constant a using the formula outlined in Equation (4.4). The average value of a is in good agreement with the value reported in literature, equal to 5.9237 Å [107], for both PbS_2 and PbS_4.

$$a = d\sqrt{h^2 + k^2 + l^2} \quad (4.4)$$

As mentioned in Section 3.3.4, the average crystallite size was calculated by the Debye-Scherrer equation (Equation (3.3)). The mean crystallite size, reported in Table 4.10, turned out to be smaller than the exciton Bohr radius of lead sulphite (18 nm) [84], allowing the classification of the PbS crystallites as quantum dots.

Table 4.10: Peak positions, Miller indices, lattice constant and crystallite size of PbS nanoparticles in sample PbS_2 and PbS_4.

Sample	2θ (°)	hkl	Lattice constant (Å)	Crystallite size (nm)	Average crystallite size (nm)
PbS_2	25.856	111	5.964	11.521	10.801 ± 0.689
	29.968	200	5.959	11.823	
	42.945	220	5.952	10.993	
	50.864	311	5.949	11.028	
	53.317	222	5.947	10.772	
	62.434	400	5.945	10.997	
	68.800	331	5.943	9.851	
	70.839	420	5.944	10.483	
	78.861	422	5.941	9.745	
PbS_4	25.949	111	5.942	13.140	11.942 ± 0.958
	29.966	200	5.959	13.629	
	42.952	220	5.951	12.174	
	50.867	311	5.949	12.102	
	53.314	222	5.948	11.538	
	62.443	400	5.944	11.863	
	68.799	331	5.943	11.053	
	70.845	420	5.944	11.311	
	78.860	422	5.942	10.667	

The PbS NPs size and shape was further investigated by image analysis of micrograph acquired by scanning electron microscopy. The average size of the PbS NPs was estimated from measurements conducted on 250 nanoparticles in ImageJ (RRID:SCR_003070). SEM images (Figure 4.14) indicates the presence of spherical particles, with an average diameter of 12.399 ± 2.719 nm for PbS_2 and 11.072 ± 3.102 nm for PbS_4, consistent with the size evaluation obtained by the Debye-Scherrer formula. Additionally, the homogeneous PbS NPs' distribution in Figure 4.14 (b)-(d) suggests that the sonication time and drop casting techniques have been well optimized.

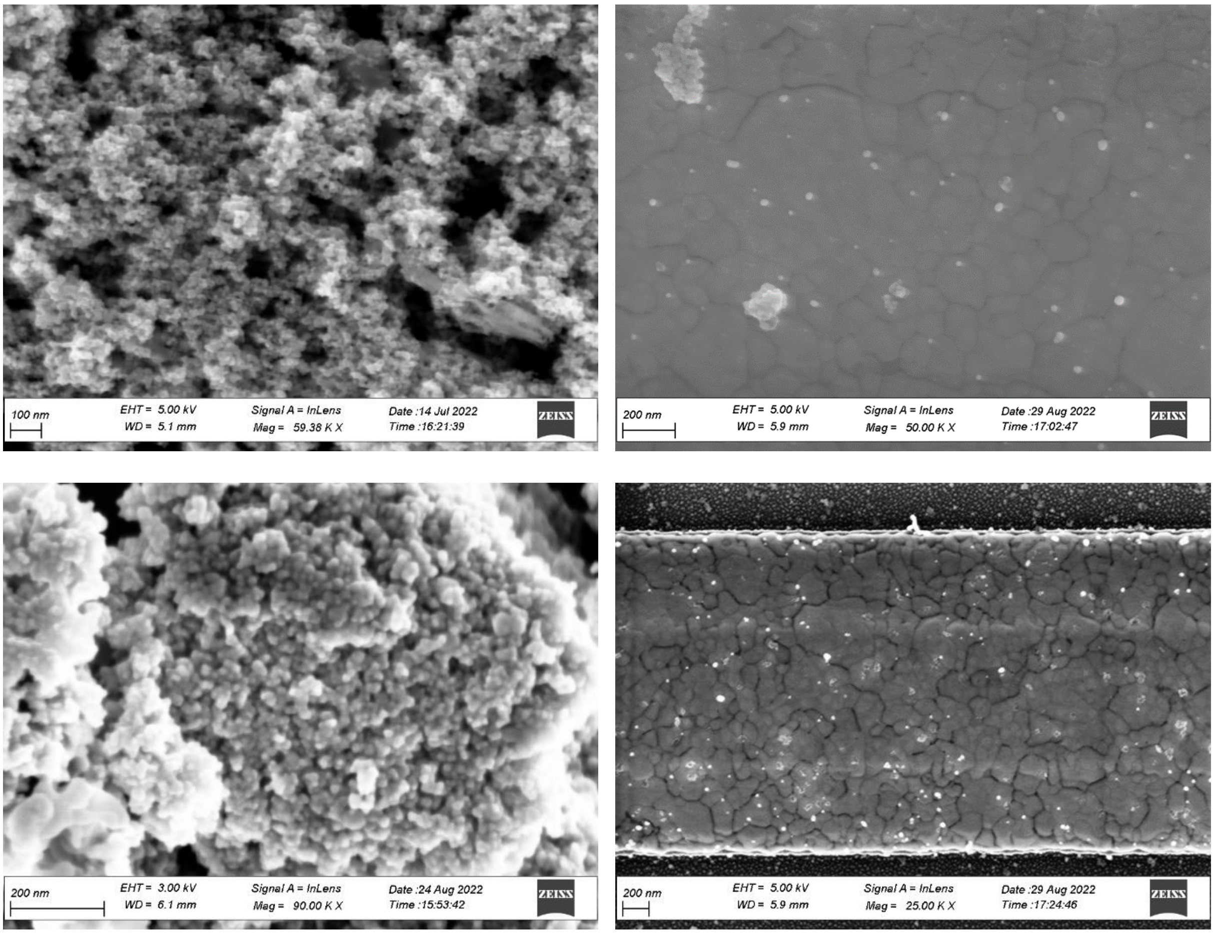

Figure 4.14: Micrograph of the lead sulfide nanoparticles of samples (a)-(b) PbS_2 and (c)-(d) PbS_4.

4.3. Decoration of rGO flakes with lead sulphide nanocrystals

The process of decoration of the reduced graphene oxide flakes was achieved at the drop casting station, as illustrated in Section 3.2.6. SEM images of the decorated rGO are reported in Figure 4.15. It can be observed that PbS nanoparticles tend to strongly adhere to rGO flakes especially in correspondence of the area between metallic fingers. The drop casting procedure and the following bath in acetone, methanol and water does not seem to affect the distribution of the nanocrystals, that appear homogeneously distributed on top of the graphene oxide flakes.

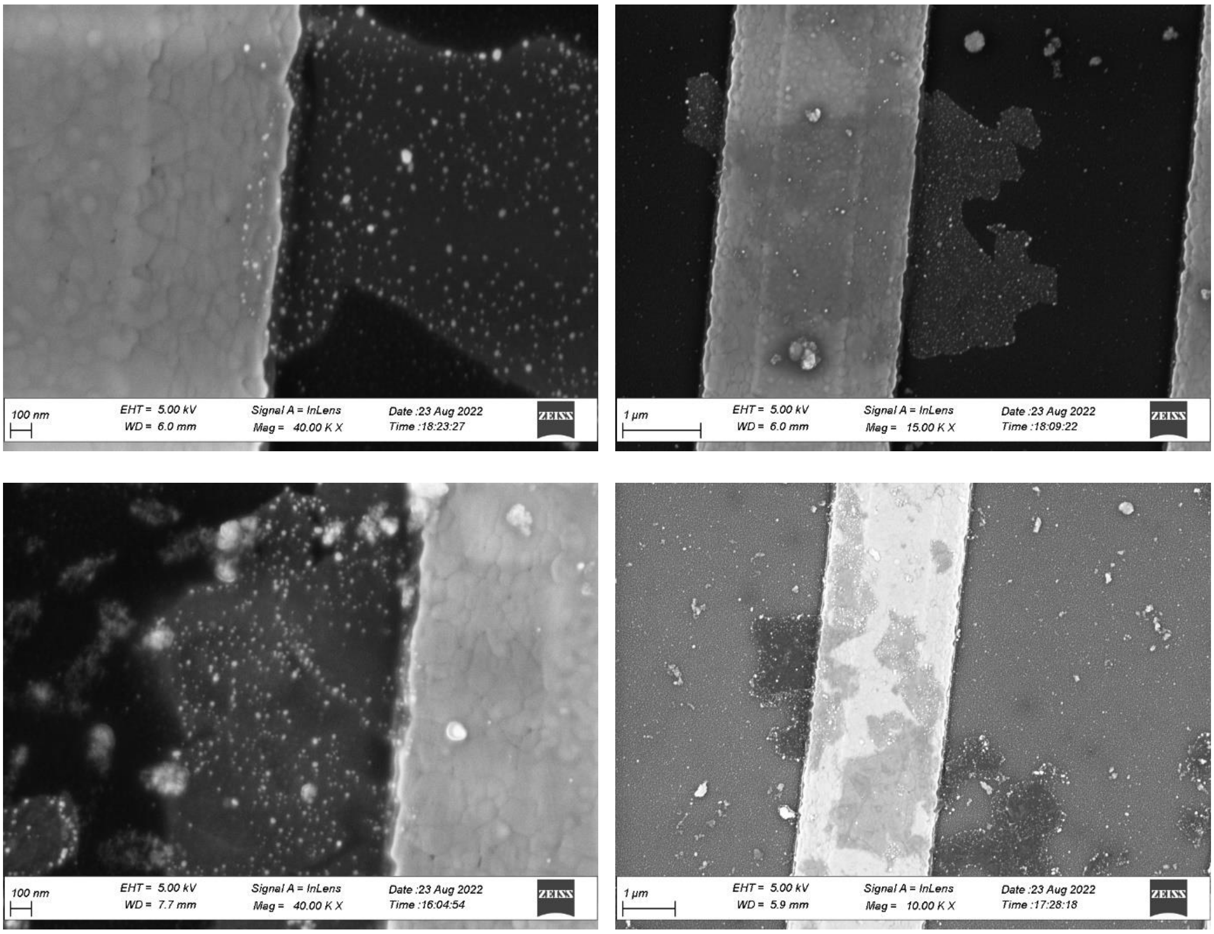

Figure 4.15: micrograph acquired by scanning electron microscopy of rGO flakes decorated with lead sulphide nanoparticles.

4.4. Preliminary gas sensing measurements

Finally, preliminary measurements of the devices' response to methane atmosphere (2%) have been performed in the gas sensing measurements setup described in Section 3.3.7. All the devices tested demonstrated no sensitivity to methane. An example of the signal detected during the experiments is reported in Figure 4.16 (a). In order to investigate the causes of poor performance of the devices, high amount of lead sulphide nanocrystals (480 droplets) was drop casted on top of the interdigitated electrodes, but the response of the device did not improve (Figure 4.16 (b)).

As already stated in Section 2.3, the device's sensitivity mechanism is related to the interaction of methane molecules with the surface of the lead nanoparticles; therefore, it can be hypothesized that the cause of the absence of sensitivity is related to the uncontrolled growth of the oxide layer around the lead sulphide nanocrystals. This aspect was not investigated in this work but further studies about the oxidation state of the lead sulphide nanoparticles are needed to achieve good sensing behaviour of the rGO-PbS NPs devices here presented.

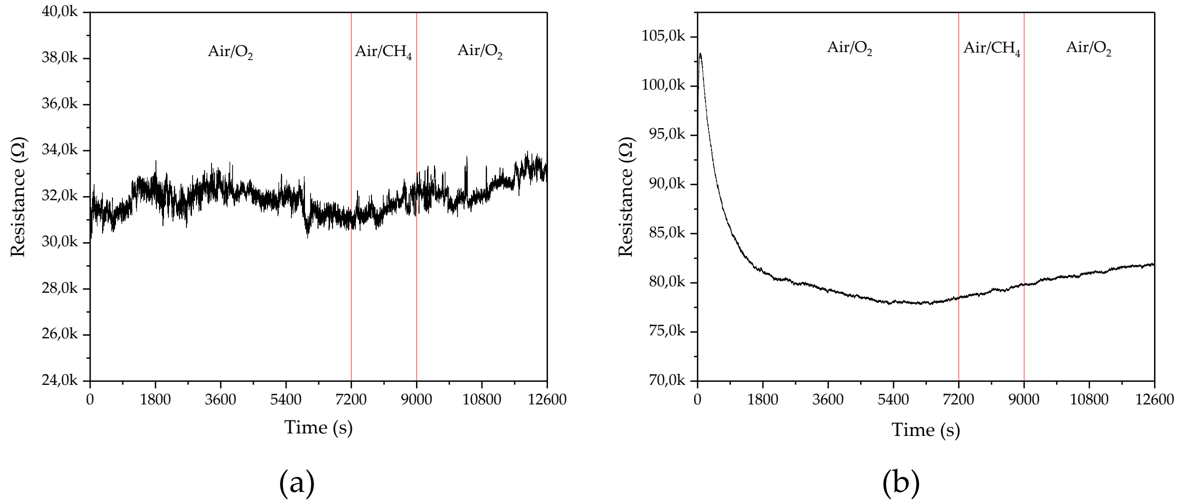

Figure 4.16: Curve of the resistance response of (a) rGO-PbS NPs and (b) PbS NPs to methane atmosphere under the conditions mentioned in Section 3.3.7.

4.5. Areas of improvement

The key area of this work that may be improved will be briefly discussed in this section.

4.5.1. A step towards green chemistry

One aspect that undoubtedly requires additional study is the improvement of the health safety of the chemical reduction process of graphene oxide. N-Methyl-2-pyrrolidone, the high boiling point solvent employed in this work, despite being regarded as one of the most effective liquid media for GO reduction, is at the top of the list of 'substances of very high concern' in many solvent selection guides, because of its proven reprotoxicity and neurotoxicity. Therefore, its substitution with less hazardous and environmentally friendly solvents it of paramount importance.

Some greener high-boiling point options are already available on the market, namely dimethyl sulfoxide (DMSO, T_B=189°C), dihydrolevoglucosenone (Cyrene, T_B=226°C) and ethyl lactate (EL, T_B=154°C), listed in order of increasing safety. Multiple reports already demonstrated the compatibility of these three solvents with graphene oxide and its reduced form making them suitable for the applications described in this work [123, 124, 125]. Most notably, cyrene outperformed NMP and DMF as dispersion medium for graphene sheets because of its ideal polarity and high viscosity, which resulted in the production of bigger and less defective graphene flakes.

It could be argued that the employment of high boiling point organic solvents in graphene oxide solvothermal reduction processes is superfluous because water-based dispersions can be heated well above their boiling point by carrying out the reduction procedure within a sealed autoclave. However, from an industrial standpoint, the ease of execution and superior quality of the final product provided by the use of green organic solvents make the latter option more appealing.

4.5.2. Deposition technique for commercial implementation

Another aspect that should be addressed prior to the commercial implementation of reduced graphene oxide-based sensors is the deposition technique of graphene oxide. In this work, a drop casting method, illustrated in Section 3.2.3, has been employed for the deposition of GO on top of the interdigitated electrodes. However, the uncontrollable variability of the deposition parameter makes this technique ineligible for industrial applications.

While many technologies are explored as potential cost-effective scalable sensors production methods, inkjet printing stands out because its drop-on-demand approach does not require the use of the masks or stencils. Additionally, as inkjet printing is primarily a non-contact process, it works with a wide range of substrates. Different authors report on the inkjet printing of GO and rGO, highlighting that cartridge temperature, nozzle diameter, substrate wettability, solvent viscosity and GO dispersion stability are all crucial factors to consider in order to prevent printer's clogging and achieve consistent results, particularly in terms of the electronic properties of the deposited material [126, 127, 128].

4.5.3. Multilayer structure for highly sensitive gas sensors

One final area of improvement concerns the possibility of increasing the sensitivity and lowering the gas detection limit. These goals can be achieved by further reducing the size of the nanoparticles and depositing the conductive rGO and sensitive PbS NPs in a stratifies structure as shown in Figure 4.17, by alternating the drop casting of the two components. This geometry ought to offer more surface area for the gas molecules to interact with the nanoparticles, resulting in the enhancement of the sensing response at lower gas concentrations [129].

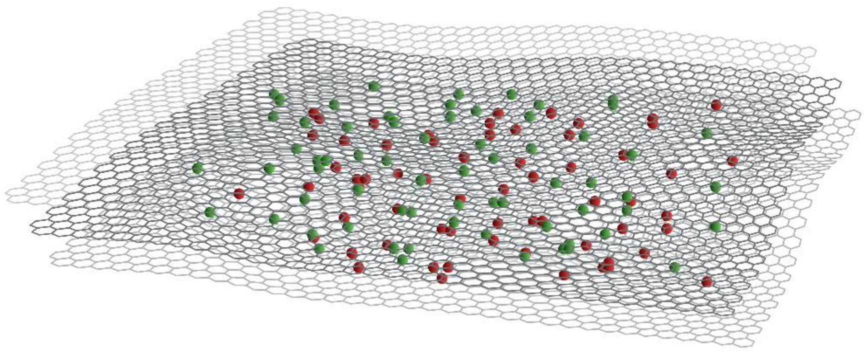

Figure 4.17: Alternation rGO-PbS nanoparticles structure for improving methane sensitivity.

5 Conclusions

Reduced graphene oxide planes decorated with semiconductor nanostructures are considered among the most promising candidates for a new generation of low-cost, energy-efficient, and highly sensitive environmental monitoring devices. In particular, rGO/PbS chemiresistive sensors have been considered for the detection of low concentration of methane. To date, in literature several GO's reductions technique have been reported but many do not provide sufficient deoxygenation, are time and energy consuming or require expensive equipment. Additionally, synthetic techniques to produce high quality, crystalline semiconductor nanoparticles are often performed at high temperature and provide poor control over the nanoparticles' size and shape.

In this work, different GO's reduction methods have been investigated and new protocols have been developed with the aim of improving the effectiveness of the deoxygenation process. The decrease in the number of oxygen moieties and the recovery of the sp^2-hybridazed carbon planes, achievable though solvothermal annealing and chemical reduction with ascorbic acid at high temperature, allowed the restoration of the conductive character of the basal plane. Accordingly, the initial resistance decreased by 10 orders of magnitude, a number greater than anything recorded in the literature so far for GO reduction with ascorbic acid.

Moreover, a simple water-based synthesis route for lead sulphide nanoparticles has been explored and the yielded PbS quantum dots were employed in rGO flakes' decoration. The successful adhesion of the small sensing element to the basal conductive plane allowed to perform preliminary measurements of the devices' response to methane atmosphere, which indicate no sensitivity towards the analyte; in this regard, further investigation about the chemical and thermal stability of the calchogenides quantum-dots should be conducted.

At last, possible areas of improvement of this work have been assessed, highlighting the possibility of using less hazardous chemicals, a more reproducible approach to GO and PbS deposition, and a multilayer structure to increase the interaction between the nanoparticles and the analyte. Additionally, XPS measurements should be collected on pressed graphene oxide and reduced graphene oxide powders, to avoid surface inhomogeneities and substrate interference, that have greatly affected the results of the analysis presented in this work. Finally, additional data about the mechanism of removal of oxygen containing group at different reduction temperatures could be acquired through FTIR analysis; instead, conductive AFM could be employed to obtain more information about the conduction mechanism in reduced rGO flakes.

Bibliography

[1] E. Hernández, C. Goze, P. Bernier and A. Rubio, "Nanotubes, Elastic Properties of C and BxCyNy Composite," *Physical Review Letters,* vol. 80, no. 20, pp. 4502-4505, 1998.

[2] M. Sang, J. Shin, K. Kim and K. Yu, "Electronic and Thermal Properties of Graphene and Recent Advances in Graphene Based Electronics Applications.," *Nanomaterials (Basel),* vol. 9, no. 3, p. 374, 2019.

[3] A. Kuzmenko, E. Van Heumen, F. Carbone and V. d. M. D., "Universal optical conductance of graphite," *Physical Review Letters,* vol. 100, no. 11, pp. -, 2008.

[4] Y. Zheng, G.-X. Ni, C.-T. Toh, M.-G. Zeng, C. Shu-Ting, K. Yao and B. Özyilmaz, "Gate-controlled nonvolatile graphene-ferroelectric memory.," *Applied Physics Letters,* vol. 94, no. 16, 2009.

[5] W. Choi, I. Lahiri, R. Seelaboyina and Y. Kang, "Synthesis of graphene and its applications: a review," *Critical Review Solid State Mater,* vol. 35, pp. 52-71, 2010.

[6] L. Xuesong, C. Weiwei, A. Jinho, K. Seyoung, N. Junghyo, Y. Dongxing, P. Richard, V. Aruna, J. Inhwa, E. Tutuc, S. K. Banerjee, L. Colombo and R. S. Ruoff, "Large-Area Synthesis of High-Quality and Uniform Graphene Films on Copper Foils," *Science,* vol. 324, no. 5932, pp. 1312-1314, 2009.

[7] P. Sutter, "Epitaxial graphene: how silicon leaves the scene.," *Nature Materials,* vol. 8, no. 3, pp. 171-172, 2009.

[8] K. S. Novoselov, A. K. Geim, S. V. Morozov, D. Jiang, Y. Zhang, S. V. Dubonos, I. V. Grigorieva and A. A. Firsov, "Electric field effect in atomically thin carbon films.," *Science,* vol. 306, pp. 666-673, 2004 .

[9] H. L. Poh, F. Šaněk, A. Ambrosi, G. Zhao, Z. Sofer and M. Pumera, "Graphenes prepared by Staudenmaier, Hofmann and Hummers methods with consequent thermal exfoliation exhibit very different electrochemical properties," *Nanoscale,* vol. 4, no. 11, pp. 3515-3522, 2012.

[10] A. Talyzin, G. Mercier, A. Klechikov, M. Hedenström, D. Johnels, D. Wei, D. Cotton, A. Opitz and E. Moons, "Brodie vs Hummers graphite oxides for preparation of multi-layered materials," *Carbon,* vol. 115, pp. 430-440, 2017.

[11] L. Shahriary and A. A. Athawale, "Graphene oxide synthesized by using modified Hummers' approach," *International Journal of Renewable Energy and Environmental Engineering,* vol. 2, no. 1, pp. 58-63, 2014.

[12] D. Joung and S. I. Khondaker, "Efros-Shklovskii variable range hopping in reduced graphene oxide sheets of varying carbon sp2 fraction.," *Physics Review,* vol. 86, no. 23, 2012.

[13] U. Hofmann and R. Holst, "Über die säurenatur und die methylierung von graphitoxyd.," *Berichte der Deutschen Chemischen Gesellschaft,* vol. 72, p. 754–771, 1939.

[14] G. Ruess, " Über das graphitoxyhydroxyd (graphitoxyd).," *Monatshefte für Chemie,* vol. 76, p. 381–417, 1946.

[15] W. Scholz and H. P. Boehm, "Untersuchungen am graphitoxid. VI. Betrachtungen zur struktur des graphitoxids.," *Zeitschrift für anorganische und allgemeine Chemie* , vol. 369 , p. 327–340, 1969.

[16] H. He, T. Riedl, A. Lerf and J. Klinowski, "Solid-State NMR Studies of the Structure of Graphite Oxide," *Journal of Physical Chemisty* , vol. 100, pp. 19954-19958, 1996.

[17] T. Szabó, O. Berkesi, P. Forgó, K. Josepovits, Y. Sanakis, T. Szabó, O. Berkesi, P. Forgó and K. Josepovits, "Evolution of surface functional groups in a series of progressively oxidized graphite oxides.," *Chemistry of Materials,* vol. 18, p. 2740–2749, 2006.

[18] S. Begum, M. Ansari and L. H. Sen, "Model, synthesis and applications of graphene oxide: a review," *Nanomaterials and Energy,* vol. 3, no. 2, pp. 61-65, 2014.

[19] D. R. Dreyer, S. Park, C. W. Bielawski and R. S. Ruof, "The chemistry of graphene oxide," *Chemical Society Review,* vol. 39, p. 228–240, 2010.

[20] K. K. H. De Silva, H.-H. Huang, R. Joshi and M. Yoshimura, "Restoration of the graphitic structure by defect repair during the thermal reduction of graphene oxide.," *Carbon* , vol. 166, pp. 74-90, 2020.

[21] P. Chamoli, S. Banerjee, K. Raina and K. Kar, "Characteristics of graphene/Reduced graphene oxide," in *Handbook of Nanocomposite Supercapacitor Materials I: Characteristics*, Springer International Publishing, 2020, pp. 155-177.

[22] S. Liu, Z. Wang, Y. Zhang, Z. Dong and T. Zhang, "preparation of zinc oxide nanoparticles-reduced graphene oxide-gold nanoparticles hybrids for NO2 reduction," *RSC Advanced,* vol. 5, p. 91760, 2015.

[23] Z. Abideen, J.-H. Kim, A. Mirzaei, H. W. Kim and S. S. Kim, "Sensing behaviour to ppm-level gasses and synergistic sensing mechanism in metal-functionalized rGO-Zn nanofibers," *Sensors and Actuators,* vol. 255, pp. 1884-1896, 2018.

[24] R. Ghanbari, R. Safaiee, M. Sheikhi, M. M. Golshan and Z. Horastani, "Graphene decorated with silver nanoparticles as a low temperature methane gas sensor," *ACS Applied Materials & Interfaces,* vol. 11, no. 24, pp. 21795-21806, 2019.

[25] H. Roshan, M. H. Sheikhi, M. K. Faramarzi Haghighi and P. Padidar, "High-performance room temperature methane gas sensor based on lead sulfide/reduced graphene oxide nanocomposite," *IEEE Sensors Journal,* vol. 20, no. 5, pp. 2526-2532, 2020.

[26] A. Kovtun, A. Candini, A. Vianelli, A. Boschi, S. Dell'Elce, M. Gobbi, K. H. Kim, L. S. Avila, P. Samorì, M. Affronte, A. Liscio and V. Palermo, "Multiscale charge transport in van der Waals thin films: reduced graphene oxide as a case study," *ACS Nano,* vol. 15, no. 2, p. 2654–2667, 2021.

[27] L. Guo, R. Shao, Y. Zhang, H. B. Jiang, X. B. Li, S. Y. Xie, B. B. Xu, Q. D. Chen, J. F. Song and H. Sun, "Bandgap tailoring and synchronous microdevices patterning of graphene oxides," *Journal Physical Chemistry,* vol. 116, no. 5, p. 3594, 2012.

[28] K. Lian, Y. Ji, X. F. Li, M. X. Jin, D. J. Ding and Y. Luo, "Big bandgap in highly reduced graphene oxides," *Journal Physical Chemistry,* vol. 117, no. 12, p. 6049, 2013.

[29] M. I. Katsnelson, F. Guinea and A. K. Geim, "Scattering of electrons in graphene by clusters of impurities," *Physical Review,* vol. 79, no. 19, p. 195426, 2009.

[30] B. Muchharla, T. N. Narayanan, K. Balakrishnan, P. M. Ajayan and S. Talapatra, "Temperature dependent electrical transport of disordered reduced graphene oxide," *2D Materials,* vol. 1, no. 1, pp. -, 2014.

[31] R. Kumar, S. Dhawan, H. Singh and A. Kaur, "Charge transport mechanism of thermally reduced graphene oxide and their fabrication for high performance shield against electromagnetic pollution," *Materials Chemistry and Physics,* vol. 180, pp. 413-421, 2016.

[32] X.-M. Huang, L.-Z. Liu, S. Zhou and J.-J. Zhao, "Physical properties and device applications of graphene oxide," *Frontiers of Physics,* vol. 15, no. 3, p. 33301, 2020.

[33] A. B. Kaiser, C. Gómez-Navarro, R. S. Sundaram, M. Burghard and K. Kern, "Electrical Conduction Mechanism in Chemically Derived Graphene Monolayers," *Nano Letters,* vol. 9, no. 5, pp. 1787-1792, 2009.

[34] G. Eda, C. Mattevi, H. Yamaguchi, H. Kim and M. Chhowalla, "Insulator to Semimetal Transition in Graphene Oxide," *Journal Physical Chemistry* , vol. 113, p. 15768–15771, 2009.

[35] A. Haque, M. A.-A. Mamun, M. F. N. Taufique, P. Karnati and K. Ghosh, "Large magnetoresistance and electrical transport properties in reduced graphene oxide thin film," *IEEE Transactions on Magnetics,* vol. 54, no. 12, pp. 1-9, 2018.

[36] C. Y. Cheah, C. Gómez-Navarro, L. C. Jaurigue and A. B. Kaiser, "Conductance of partially disordered graphene: crossover from temperature-dependent to field-dependent variable range hopping," *IOP Publishing,* vol. 25, no. 46, pp. 465303- 465311, 2013.

[37] M. N. Cınar, A. Antidormi, V.-H. Nguyen, A. Kovtun, S. Lara-Avila, A. Liscio, J.-C. Charlier, S. Roche and H. Sevincli, "Toward optimized charge transport in multilayer reduced graphene oxide," *Nano Letters 2022, 22, 2202−2208,* vol. 22, p. 2202−2208, 2022.

[38] M. McAllister, J.-L. Li, D. Adamson, H. Schniepp, A. Abdala, J. Liu, M. Herrera-Alonso, D. L. Milius, R. Car, R. K. Prud'homme and I. A. Aksay, "Single sheet functionalized graphene by oxidation and thermal expansion of graphite.," *Chemical materials ,* vol. 19, no. 18, p. 4396–4404, 2007.

[39] S. Pei and H. Cheng, "The reduction of graphene oxide," *Carbon ,* vol. 50, no. 9, pp. 3210-3228, 2012.

[40] Z.-S. Wu, W. Ren, L. Gao, J. Zhao, Z. Chen, B. Liu, D. Tang, B. Yu, C. Jiang and H.-M. Cheng, "Synthesis of Graphene Sheets with High Electrical Conductivity and Good Thermal Stability by Hydrogen Arc Discharge Exfoliation," *ACS Nano,* vol. 3, p. 411–417 , 2009.

[41] X. Wang, L. Zhi and K. Müllen, "Transparent, Conductive Graphene Electrodes for Dye-Sensitized Solar Cells," *Nano Letters,* vol. 8, p. 323–327, 2008.

[42] H. Tingchao, Q. Xiaoying, C. W. J. Rui, H. Zhang and S. Handong, "Enhanced Optical Nonlinearity in Noncovalently Functionalized Amphiphilic Graphene Composites.," *Chempluschem,* vol. 77, no. 8, pp. 688-693, 2012.

[43] N. S. Alam, N. Sharma and L. Kumar, "Synthesis of Graphene Oxide (GO) by Modified Hummers Method and Its Thermal Reduction to Obtain Reduced Graphene Oxide (rGO)," *Graphene,* vol. 6, pp. 1-18, 2017.

[44] H. Ramamoorthy, K. Buapan, T. Chiawchan, K. Thamkrongart and R. Somphonsane, "Exploration of the temperature-dependent correlations present in the structural, morphological and electrical properties of thermally reduced free-standing graphene oxide paper.," *Journal of Material Science,* vol. 56, p. 15134–15150, 2021.

[45] C. Mattevi, G. Eda, S. Agnoli, S. Miller, K. A. Mkhoyan, O. Celik, D. Mastrogiovanni and G. Granozzi, "Evolution of Electrical, Chemical, and Structural Properties of Transparent and Conducting Chemically Derived Graphene Thin Films," *Advanced Functional Materials ,* vol. 19, p. 2577–2583, 2009.

[46] S. Pei, J. Zhao, J. Du, W. Ren and H.-M. Cheng, "Direct reduction of graphene oxide films into highly conductive and flexible graphene films by hydrohalic acids," *Carbon,* vol. 48, no. 15, pp. 4466-4474, 2010.

[47] Y. Zhou, Q. Bao, L. A. L. Tang, Y. Zhong and K. P. Loh, "Hydrothermal dehydration for the "green" reduction of exfoliated graphene oxide to graphene and demonstration of tunable optical limiting properties," *Chemical Materials ,* vol. 21, p. 2950–2956, 2009.

[48] B. Yuan, C. Bao, X. Qian, P. Wen, W. Xing, L. Song and Y. Hu, "A facile approach to prepare graphene via solvothermal reduction of graphite oxide," *Materials Research Bulletin,* vol. 55, p. 48–52, 2014.

[49] S. Dubin, S. Gilje, K. Wang, V. Tung, K. Cha, A. Hall, J. Farrar, R. Varshneya, Y. Yang and R. Kaner, "A one-step, solvothermal reduction method for producing reduced graphene oxide dispersions in organic solvents," *ACS Nano ,* vol. 4, no. 7, p. 3845–3852, 2010.

[50] V. H. Pham, T. V. Cuong, S. H. Hur, E. Oh, E. J. Kim, E. W. Shin and J. S. Chung, "Chemical functionalization of graphene sheets by solvothermal reduction of a graphene oxide suspension in N-methyl-2-pyrrolidone," *Journal of Materials Chemistry,* vol. 21, p. 3371–3377, 2011.

[51] Y. Liang, J. Frisch, L. Zhi, H. Norouzi-Arasi, X. Feng, J. P. Rabe, N. Koch and K. Mullen, "Transparent, highly conductive graphene electrodes from acetylene-assisted thermolysis of graphite oxide sheets and nanographene molecules," *Nanotechnology ,* vol. 20, no. 43, p. 434007, 2009.

[52] V. López, R. S. Sundaram, C. Gómez-Navarro, D. Olea, M. Burghard, J. Gómez-Herrero, F. Zamora and K. Kern, "Chemical Vapor Deposition Repair of Graphene Oxide: A Route to Highly-Conductive Graphene Monolayers," *Advanced materials ,* vol. 21, pp. 4683-4686, 2009.

[53] C.-Y. Su, Y. Xu, W. Zhang, J. Zhao, A. Liu, X. Tang, C.-H. Tsai, Y. Huang and L.-J. Li, "Highly Efficient Restoration of Graphitic Structure in Graphene Oxide Using Alcohol Vapors," *ACS Nano,* vol. 4, no. 9, pp. 5285-5292, 2010.

[54] B. Dai, L. Fu, L. Liao, N. Liu, K. Yan, Y. Chen and Z. Liu, "High-quality single-layer graphene via reparative reduction of graphene oxide," *Nano Research,* vol. 4, no. 5, pp. 434-439, 2011.

[55] D. Zhu, H. Pu, P. Lv, Z. Zhu, C. Yang, R. Zheng, Z. Wang, C. Liu, E. Hu, J. Zheng, K. Yu, W. Wei, L. Chen and J. Chen, "Healing of reduced graphene oxide with methane + hydrogen plasma," *Carbon,* vol. 120, pp. 274-280, 2017.

[56] C. Gong, M. Acik, R. M. Abolfath, Y. Chabal and C. Kyeongjae, "Graphitization of graphene oxide with ethanol during thermal reduction," *Journal of Physical Chemistry ,* vol. 116, p. 9969–9979, 2012.

[57] M. Hassan, M. Walter and M. Moseler, "Interactions of polymers with reduced graphene oxide: van der Waals binding energies of benzene on graphene with defects," *Physical Chemistry ,* vol. 16, no. 1, pp. 33-37, 2014.

[58] O.-K. Park, N. H. Kim and J. H. Lee, "Rapid effective reduction by microwave-irradiated thermal reaction for large-scale production of high-quality reduced graphene oxide," *Carbon ,* vol. 187, pp. 330-337, 2021.

[59] R. Negishi, M. Akabori, T. Ito, Y. Watanabe and Y. Kobayashi, "Band-like transport in highly crystalline graphene films from defective graphene oxides," *Scientific Reports,* vol. 6, no. 1, pp. -, 2016.

[60] S. Stankovich, D. A. Dikin, R. D. Piner, K. A. Kohlhaas, A. Kleinhammes, Y. Jia, Y. Wu, S. T. Nguyen and R. S. Ruoff, "Synthesis of graphene-based nanosheets via chemical reduction of exfoliated graphite oxide," *Carbon,* vol. 45, no. 7, p. 1558–1565, 2007.

[61] H.-J. Shin, K. K. Kim, A. Benayad, S.-M. Yoon, H. K. Park, I.-S. Jung, M. H. Jin, H.-K. Jeong, J. M. Kim, J.-Y. Choi and Y. H. Lee, "Efficient Reduction of Graphite Oxide by Sodium Borohydride and Its Effect on Electrical Conductance," *Advanced Functional Material,* vol. 19, p. 1987–1992, 2009.

[62] W. Gao, L. B. Alemany, L. Ci and P. M. N. Ajayan, "New insights into the structure and reduction of graphite oxide," *Natural Chemistry,* vol. 1, p. 403–408, 2009.

[63] I. K. Moon, J. Lee, R. S. Ruoff and H. Lee, "Reduced graphene oxide by chemical graphitization," *Natural Communication ,* vol. 73, no. 1, p. 2041, 2010.

[64] M. Fernandez-Merino, L. Guardia, J. Paredes, S. Villar-Rodil, P. Solis-Fernandez, A. Martinez-Alonso and J. M. D. Tascòn, "Vitamin C is an ideal substitute for hydrazine in the reduction of graphene oxide suspensions," *Journal of Physical Chemistry ,* vol. 114, no. 14, p. 6426–6458, 2010.

[65] W. Chen, L. Yan and P. R. Bangal, "Chemical reduction of graphene oxide to graphene by sulfur-containing compounds," *The Journal of Physical Chemistry,* vol. 141, no. 47, p. 19885–19890, 2010.

[66] D. Li, M. B. Muller, S. Gilje, R. B. Kaner and G. G. Wallace, "Processable aqueous dispersions of graphene nanosheets," *Nature Nanotechnology,* vol. 3, no. 2, p. 101–105, 2008.

[67] J. Gao, F. Liu, Y. Liu, N. Ma, Z. Wang and X. Zhang, "Environment-Friendly Method To Produce Graphene That Employs Vitamin C and Amino Acid," *Chemistry of materials,* vol. 22, p. 2213–2218, 2010.

[68] M. Palomba, G. Carotenuto and A. Longo, "A Brief Review: the use of L-ascorbic acid as a green reducing agent of graphene oxide," *Materials,* vol. 15, pp. 6456-6472, 2022.

[69] J. Zhang, H. Yang, G. Shen, P. Cheng, J. Zhang and S. Guo, "Reduction of graphene oxide viaL-ascorbic acid," *Chemical Commununication,* vol. 46, p. 1112–1114, 2010.

[70] J. Guo, J. Zhang, M. Zhu, D. Ju, H. Xu and B. Cao, "High-performance gas sensor based on ZnO nanowires functionalized by Au nanoparticles," *Sensors and Actuators B: Chemical,* vol. 199, pp. 339-345, 2014.

[71] L. Wang, Y. Kang, X. Liu, S. Zhang, W. Huang and S. Wang, "ZnO nanorod gas sensor for ethanol detection," *Sensors and Actuators B: Chemical,* vol. 162, no. 1, pp. 237-243, 2012.

[72] J. Rebholz, C. Dee, U. Weimar and N. Barsan, “A self-doping surface effect and its influence on the sensor performance of undoped SnO2 based gas sensors,” *Procedia Eng.* , vol. 120, p. 83–87., 2015.

[73] Y. Liu, E. Koep and M. Liu, “A highly sensitive and fast-responding SnO2 sensor fabricated by combustion chemical vapor deposition,” *Chemistry Materials,* vol. 17, p. 3997–4000, 2005.

[74] G. Jiménez-Cadena, J. Riu and F. X. Rius, “Gas sensors based on nanostructured materials,” *Analyst,* vol. 132, no. 11, pp. 1083-1099, 2007.

[75] A. Mosahebfard, H. D. Jahromi and M. H. Sheikhi, “Highly Sensitive, Room Temperature Methane Gas Sensor Based on Lead Sulfide Colloidal Nanocrystals,” *IEEE Sensor Journal,* vol. 16, no. 11, pp. 4174-4179, 2016.

[76] L. Bharatula, M. Erande, I. Mulla, C. Rout and D. Late, “Sn2 nanoflakes for efficient humidity and alcohol sensing at room temperature,” *RCS Advanced,* vol. 6, no. 107, pp. 105421-105427, 2016.

[77] R. Li, K. Jiang, S. Chen, Z. Lou, T. Huang, D. Chen and G. Shen, “SnO2/SnS2 nanotubes for flekìxible room temperature NH3 gas sensors,” *RSC Advanced,* vol. 223, pp. 52503-52509, 2017.

[78] D. Zhang, G. Dong, Y. Cao and Y. Zhang, “Ethanol gas sensing properties of lead sulfide quantum dots-decorated zinc oxide nanorods prepared by hydrothermal process combining with successive ionic-layer adsorption and reaction method,” *Journal of Colloid and Interface Science,* vol. 528, p. 184–191, 2018.

[79] P. S. Kuchi, H. Roshan and M. H. Sheikhi, “A novel room temperature ethanol sensor based on PbS:SnS2 nanocomposite with enhanced ethanol sensing properties,” *Journal of Alloys and Compounds 816 (2020) 152666,* vol. 816, pp. 152666-152674, 2020.

[80] A. Mosahebfard, H. Roshan and M. H. Sheikhi, “Enhancement of methane gas sensing characteristics of lead sulfide colloidal nanocrystals by silver nanoparticles decoration,” *IEEE Sensor Journal,* vol. 17, no. 11, pp. 3375-3380, 2017.

[81] M. Suganya and A. Balu, “PbS nanopowder – synthesis, characterization and antimicrobial activity,” *Materials Science-Poland,* vol. 35, pp. 322 - 328, 2017.

[82] Z. Q. Mamiyev and N. O. Balayeva, “Preparation and optical studies of PbS nanoparticles,” *Optical Materials,* vol. 46, p. 522–525, 2015.

[83] I. Moreels, K. Lambert, D. Smeets, D. De Muynck, T. Nollet, J. C. Martins, F. Vanhaecke, A. Vantomme, C. Delerue, G. Allan and Z. Hens, “Size-Dependent Optical Properties of Colloidal PbS Quantum Dots,” *ACS Nano,* vol. 3, no. 10, p. 3023–3030, 2009.

[84] X. Fu, Y. Pan, X. Wang and J. R. Lombardi, “Quantum confinement effects on charge-transfer between PbS quantum dots and 4-mercaptopyridine,” *Journal of Chemical Physics,* vol. 134, no. 2, 2011.

[85] S. I. Sadovnikov, A. I. Gusev and A. A. Rempel, “Nanostructured lead sulfide: synthesis, structure and properties,” *Russian Chemical Reviews,* vol. 85, no. 7, pp. 731-758, 2016.

[86] S. I. Sadovnikov, N. S. Kozhevnikova and A. A. Rempel, “Oxidation of Nanocrystalline Lead Sulfide in Air,” *Russian Journal of Inorganic Chemistry,* vol. 56, no. 12, p. 1864–1869, 2011.

[87] J. Chang and E. R. Waclawik, “Colloidl semiconductor nanocrystals: controlled synthesis and surface chemistry in organic media,” *RSC Advances,* vol. 4, pp. 23505-23527, 2014.

[88] N. Kozhevnikova, S. Sadovnikov and A. Rempel', “One-pot synthesis of lead sulfide nanoparticles,” *Russian Journal of General Chemistry,* vol. 81, no. 10, pp. 2062-2066, 2011.

[89] C. Pal, L. Sosa-Vargas, J. J. Ojeda, A. K. Sharma, A. N. Cammidge, M. J. Cook and A. K. Ray, “Charge transport in lead sulfide quantum dots/phthalocyanines hybrid nanocomposites,” *Organic Electronics,* vol. 44, pp. 132-143, 2017.

[90] A. K. Mishra and S. Saha, “Synthesis and characterization of PbS nanostructures to compare with bulk,” *Chalcogenide Letters,* vol. 17, no. 3, pp. 147-159, 2020.

[91] H. Roshan, A. Mosahebfard and M. H. Sheikhi, “Effect of gold nanoparticles incorporation on electrical conductivity and methane gas sensing characteristics of lead sulfide colloidal nanocrystals,” *IEEE Sensors Journal,* vol. 18, no. 5, pp. 1940-1945, 2018.

[92] S. Choopun, N. Hongsith and E. Wongrat, “Metal-oxide nanowires for gas sensing,” *Nanowires-Recent Advances,* pp. 3-24, 2012.

[93] A. Mosahebfard, R. Safaiee and M. Sheikhi, “Density functional theory of influence of methane adsorption on the electronic properties of a PbS cluster,” *Pramana – J. Phys. ,* vol. 93, no. 9, pp. 1-6, 2019.

[94] D. Konios, M. M. Stylianakis, E. Stratakis and E. Kymakis, “Dispersion behaviour of graphene oxide and reduced graphene oxide,” *Journal of Colloid and Interface Science ,* vol. 430, p. 108–112, 2014.

[95] M. Tasa, Y. Altin and A. C. Bedeloglu, “Reduction of graphene oxide thin films using a stepwise thermal annealing assisted L-ascorbic acid,” *Diamond and related materials ,* vol. 92, pp. 242-247, 2019.

[96] W. Smith and J. Hashemi, in *Foundations of Materials Science and Engineering. 5th ed.*, Boston, Mass, McGraw-Hill, 2010, p. 1068.

[97] F. Mokobi, “Scanning Electron Microscope (SEM)- Definition, Principle, Parts, Images,” 11 March 2022. [Online]. Available:

https://microbenotes.com/scanning-electron-microscope-sem/. [Accessed 30 September 2022].

[98] R. Schmitt, "Scanning Electron Microscope," in *CIRP Encyclopedia of Production Engineering*, Berlin, Springer, Berlin, Heidelberg, 2019, p. 1085–1089.

[99] "What is SEM? Scanning Electron Microscopy Explained," Thermofisher, 12 July 2022. [Online]. Available: https://www.thermofisher.com/blog/materials/what-is-sem-scanning-electron-microscopy-explained/. [Accessed 30 September 2022].

[100] A. Eckmann, A. Felten, A. Mishchenko, L. Britnell, R. Krupke, K. S. Novoselov and C. Casiraghi, "Probing the Nature of Defects in Graphene by Raman Spectroscopy," *Nano Letters,* vol. 12, no. 8, pp. 3925-3930, 2012 .

[101] I. Childres, L. A. Jauregui, W. Park, H. Cao and Y. P. Chen, "Raman Spectroscopy of Graphene and Related Materials," in *New Developments in Photon and Materials Research*, New York, USA, Nova Science Publishers, 2013, pp. 403-418.

[102] J.-B. Wu, M.-L. Lin, X. Cong, H.-N. Liu and P.-H. Tan, "Raman spectroscopy of graphene-based materials and its applications in related devices," *Chem. Soc. Rev.,* vol. 47, no. 5, pp. 1822-1873, 2018.

[103] A. Ambrosi, C. K. Chua, A. Bonanni and M. Pumera, "Electrochemistry of Graphene and Related Materials," *Chemical Reviews,* vol. 114, no. 14, pp. 7150-7188, 2014.

[104] A. C. Ferrari and D. M. Basko, "Raman spectroscopy as a versatile tool for studying the properties of graphene," *Nature Nanotechnology,* vol. 8, no. 4, pp. 235-246, 2013.

[105] D. Brandon and W. Kaplan, "Chemical analysis of surface composition," in *Microstructural Characterization of Materials.*, Wiley, 2008, pp. 424-429.

[106] F. J. J. Mederos-Henry, *Decoration of nanocarbon supports with magnetic nanoparticles for the control of electromagnetic propagation,* Louvain-la-Neuve, Belgium: Université catholique de Louvain, 2019.

[107] Y. Noda, K. Masumoto, S. Ohba, Y. Saito, K. Toriumi, Y. Iwata and I. Shibuya, "Temperature dependence of atomic thermal parameters of lead chalcogenides, PbS, PbSe and PbTe," *Acta Crystallographica Section C,* vol. 48, no. 8, pp. 1443-1445, 1987.

[108] K. Barmak and K. Coffey, "X-ray diffraction for characterizing metallic films," in *Metallic Films for Electronic, Optical and Magnetic Applications*, Woodhead Publishing, 2014, pp. 3-38.

[109] A. Vorokh, "Scherrer formula: estimation of error in determining small nanoparticle size," *Nanosystems: Physics, Chemistry, Mathematics,* pp. 364-369, 2018.

[110] J. Singh, “Moseley's Law - Characteristics X-rays | Solved Problems,” PsiPhiETC, 01 October 2019. [Online]. Available: https://www.concepts-of-physics.com/modern/moseleys-law.php. [Accessed 05 October 2022].

[111] P. Turner, M. Hodnett, R. Dorey and J. D. Carey, “Controlled sonication as a route to in-situ graphene flake size control,” *Scientific Reports,* vol. 9, no. 1, pp. 2045-2053, 2019.

[112] International Organization for Standardization (ISO). Nanotechnologies-Vocabulary-Part 13: Graphene and related two-dimensional (2D) materials., ISO/TS 80004-13, 2017.

[113] S. Colonna, D. Battegazzore, M. Eleuteri, R. Arrigo and A. Fina, “Properties of graphene-related materials controlling the thermal conductivity of their polymer nanocomposites,” *Nanomaterials,* vol. 10, no. 11, pp. 2079-2099, 2020.

[114] D. Lòpez-Diaz, M. Lòpez Holgado, J. Garcìa-Fierro and M. M. Velàzquez, “Evolution of the Raman spectrum with the chemical composition of graphene oxide.,” *Journal of Physical Chemistry,* vol. 121, pp. 20489-20497, 2017.

[115] S. Claramunt, A. Varea, D. Lopez-Díaz, M. M. Velazquez, A. Cornet and A. Cirera, “The importance of interbands on the interpretation of the Raman spectrum of graphene oxide,” *Journal of Physical Chemistry,* vol. 119, pp. 10123-10129, 2015.

[116] A. A. K. King, B. R. Davies, N. Noorbehesht, P. Newman, T. L. Church, A. T. Harris, J. M. Razal and A. I. Minett, “New Raman metric for the characterisation of graphene oxide and its derivatives,” *Scientific Reports,* vol. 6, pp. 19491-19497, 2016.

[117] A. Y. Lee, K. Yang, N. Duc Anh, C. Park, S. Mi Lee, T. G. Lee and M. S. Jeong, “Raman study of D* band in graphene oxide and its correlation with reduction,” *Applied Surface Science,* vol. 536, 2021.

[118] F. Berrellez-Rayes and S. Alvarez-Garcia, “Insight into the interaction of graphene oxide and Adsorbed RhB by Raman spectral deconvoluted scanning,” *Journal of Physical Chemistry,* vol. 123, pp. 30021-30027, 2019.

[119] R. Saito, M. Hofmann, G. Dresselhaus, A. Jorio and M. Dresselhaus, “Raman Spectroscopy of Graphene and Carbon Nanotubes.,” *Carbon,* vol. 43, pp. 1731-1742, 2005.

[120] A. Sadezky, H. Muckenhuber, H. Grothe, R. Niessner and U. Pöršhl, “Raman microspectroscopy of soot and related carbonaceous Raman microspectroscopy of soot and related carbonaceous.,” *Carbon,* vol. 43, pp. 1731-1742, 2005.

[121] R. J. Nemanich and S. A. F. Solin, “First- and second-order Raman scattering from finite-size crystals of graphite.,” *Physics Review,* vol. 20, pp. 391-401, 1979.

[122] P. Barnes, S. Jacques and M. Vickers, “Peak Shape Functions: Pseudo-Voigt and Other Functions,” Birkbeck College, University of London, 2006. [Online].

Available: http://pd.chem.ucl.ac.uk/pdnn/peaks/others.htm. [Accessed 17 October 2022].

[123] J. Fernandes, S. S. Nemala, G. De Bellis and A. Capasso, "Green solvents for the liquid phase exfoliation production of graphene: the promising case of cyrene," *Frontiers in Chemistry* , vol. 10, pp. -, 2022.

[124] D. Mondal, J. P. Chaudhary and M. Sharmaab, "Simultaneous dehydration of biomass-derived sugars to 5-hydroxymethyl furfural (HMF) and reduction of graphene oxide in ethyl lactate: one pot dual chemistry," *RSC Advanced,* vol. 4, p. 29834–29839, 2014.

[125] P. Sungjin, J. An, I. Jung, R. D. Piner, S. J. An, X. Li, A. Velamakanni and R. S. Ruoff, "Colloidal suspensions of highly reduced graphene oxide in a wide variety of organic solvents variety of organic solvents," *Nano Letters,* vol. 9, no. 4, p. 1593–1597, 2009.

[126] D. Barmpakos, V. Belessi, R. Schelwald and G. Kaltsas, "Evaluation of inkjet-Printed reduced and functionalized water-dispersible graphene oxide and graphene on polymer substrate—Application to printed temperature sensors," *Nanomaterials (Basel),* vol. 11, no. 8, p. 2025, 2021.

[127] V. Dua, S. Surwade, S. Ammu, S. Agnihotra, S. Jain, K. Roberts, S. Park, R. Ruoff and S. Manohar, "All-organic vapor sensor using inkjet-printed reduced graphene oxide," *Angewandte Chemie International Edition,* vol. 49, pp. 2154-2157, 2010.

[128] T. a. C. C. a. F. K. a. B. P. a. C. J. T. Pandhi, C. Cornwell, K. Fujimoto, P. Barnes, J. Cox, H. Xiong, P. H. Davis, H. Subbaraman, J. E. Koehne and D. Estrada, "Fully inkjet-printed multilayered graphene-based flexible electrodes for repeatable electrochemical response," *RSC Advanced,* vol. 10, no. 63, pp. 38205-38219, 2020.

[129] A. Chakraborthy, S. Nuthalapati, A. Nag, N. Afsarimanesh, M. E. E. Alahi and M. E. Altinsoy, "A critical review of the use of graphene-based gas sensors," *Chemosensors,* vol. 10, no. 355, pp. 1-29, 2022.

List of Figures

List of Tables

List of Abbreviations

AFM	Atomic force microscopy
BSE	Back scattered electron
CVD	Chemical vapor deposition
DMF	N,N-dimethylformamide
DMM	Digital multimeter
DOS	Density of states
ED-XRF	Energy dispersive X-ray fluorescence
EHT	Electron high tension
ES-VRH	Efros-Shklovskii variable range hopping
FTIR	Fourier-transform infrared spectroscopy
GIC	Graphite intercalated compound
GO	Graphene oxide
IDE	Interdigitated electrodes
L-AA	L-ascorbic acid
MD	Molecular dynamics
M-VRH	Mott variable range hopping
NC	Nanocrystals
NMP	N-methyl-2-pyrrolidone
NMR	Nuclear magnetic resonance
NP	Nanoparticles
QD	Quantum dot
rGO	Reduced graphene oxide
SE	Secondary electrons
SEM	Scanning electron microscopy
SESI	Secondary Electrons Secondary Ions
TGA	Thermogravimetric analysis
XPS	X-Ray photoelectron spectroscopy
XRD	X-ray diffraction
XRF	X-ray Fluorescence

Acknowledgments

First of all, I would like to thank Professor Hackens, Professor Hermans and Professor Li Bassi for the opportunity to undertake this thesis project. Their guidance and expertise have helped me immensely throughout this work.

I am deeply grateful to Professor Massa Fernandes, my mentor during these months, without whom this project would not have been possible. Not only he was always ready to assist me step by step providing his expertise but also, he enriched me professionally and personally by transmitting me his passion and commitment towards the scientific research.

I would like to acknowledge the help of all Winfab staff members and collegues at NAPS. Special thanks to Alessandra and Oriane, who made me feel at home in a foreign country while encouraging me throughout this research project.

Thanks to all my friends with whom I shared these university years between study sessions and coffee breaks.

Finally, I the most important thanks to my family and my boyfriend for having supported me financially and emotionally, even when I was not the easiest person, and for having motivated me in the pursue of my studies.